Title	Studies on Sustainable and Practical Materials Based on Polysaccharides
Author(s)	原田, 信幸
Citation	大阪大学, 2022, 博士論文
Version Type	VoR
URL	https://doi.org/10.18910/87733
rights	
Note	

Doctoral Dissertation

Studies on Sustainable and Practical Materials Based on Polysaccharides

多糖類を基盤とする持続可能で実用的な材料に関する研究

NOBUYUKI HARADA

October 2021
Nippon Shokubai Research Alliance Laboratories
Osaka University

Content

General Introduction

We are living in the "polymer age". Polymers can be mass-produced and are easy to mold, light and durable, resistant to rust and corrosion, hygienic, and airtight. Accordingly, they contribute to many aspects of our lives. Indeed, it is almost impossible to imagine daily life, communication, mobility, health care, science, and even sports and culture without them.

Hermann Staudinger, awarded the Nobel Prize for Chemistry in 1953, proposed in 1920 that biopolymers (such as rubber) and man-made polymeric materials are composed of very high-molecular-weight polymers formed by a covalent bond between a very large number of monomer molecules. In 1922, he termed these materials macromolecules [1].

Early polymer research and development were based on the chemical modification of natural polymers. A variety of natural raw materials such as rubber and cellulose were chemically modified and converted into useful polymer materials with new properties. Latex from rubber trees was collected and converted to industrial rubber for making tires, and approximately 40% of raw materials are still supplied by rubber tree plantations today.

Nitrocellulose, a highly flammable compound first obtained by the nitration of cellulose in the late 19th century, is the main ingredient of modern gunpowder and is still employed in certain lacquers and paints. Plasticized nitrocellulose was the first thermoplastic material to be developed and it enabled the manufacture of photographic films [2].

Polymer chemistry, which began with the chemical modification of natural polymers, has enriched peoples' lives even more in the 20th Century with the development of various commercial synthetic polymers. This breakthrough was brought about by petrochemistry. The use of fossil materials such as petroleum and gas as raw materials for polymer manufacture has greatly simplified and improved the cost effectiveness of polymer production.

Natural and artificial polymers have thus become indispensable in our daily lives while supplementing each other. For example, the structurally and functionally diverse products of polymer chemistry are widely applied in food packaging, textiles, automobile parts, construction, electronics, bottles, toys, superabsorbent materials, membranes for water desalination, drug-release carriers, and biopolymers for tissue engineering.

The total production of synthetic polymers in the first decade of the 21st Century was roughly equal to that for the entire 20th Century [3]. However, global issues such as population growth, fossil resource constraints, increasing global energy demands, marine plastic waste issues, and global warming are stimulating a growing demand for renewable polymer products. This has led to the development of sophisticated methods for producing and applying sustainable polymers manufactured using renewable biomass as the feedstock.

Biomasses are defined as "Resources that are organic matter derived from animals and plants (excluding fossil resources)" in the Biomass Japan Comprehensive Strategy, which is being promoted mainly by the Ministry of Agriculture, Forestry, and Fisheries. Familiar examples of relevant biomasses are starch generated from carbon dioxide and water by photosynthesis in plants; lignocellulose (cellulose, hemicellulose, and lignin) that constitutes the secondary cell walls of plants; natural rubber (cis-polyisoprene) in the sap of rubber trees; naturally derived polypeptides such as collagen and gelatin; and polyhydroxy alkanoates (PHAs) produced by bacteria. As shown in Figure 1, excluding long-known modified natural polymers such as carboxymethylcellulose (CMC) and cellulose acetate (CA), the global production of renewable polymers was approximately 2.11 million metric tons in 2020, accounting for only ~1% of the world's total polymer production. However, the global production of renewable polymers is increasing [4].

Biopolymers derived from biomass are roughly classified into three types depending on their route of production. The first is biopolymers synthesized from biomass by microorganisms. A typical polymer obtained by this route is PHA. Polymers obtained from microorganisms and plants are usually used without modification.

The second is chemically synthesized biopolymers in which biomass-derived monomers are chemically polymerized. When the monomers obtained from biomass are identical to those derived from petroleum, they are called drop-in (replacement) monomers. The resulting biopolymers are indistinguishable from petroleum-based products, thus they can be mixed with petroleum-derived products and recycled. A typical example is bio-polyethylene (bio-PE) made from bioethanol-derived bio-ethylene.

The third is biopolymers for which natural polymers themselves are used as biomass. A typical example is the direct modification of natural polymers, such as the cellulose in CMC and CA, and natural polymer blends containing other polymers, such as natural-fiber-reinforced polymer composites (NFRCs) [5] and starch blends [6, 7]. Here, starch and cellulose, as-is or post-modification, have been used.

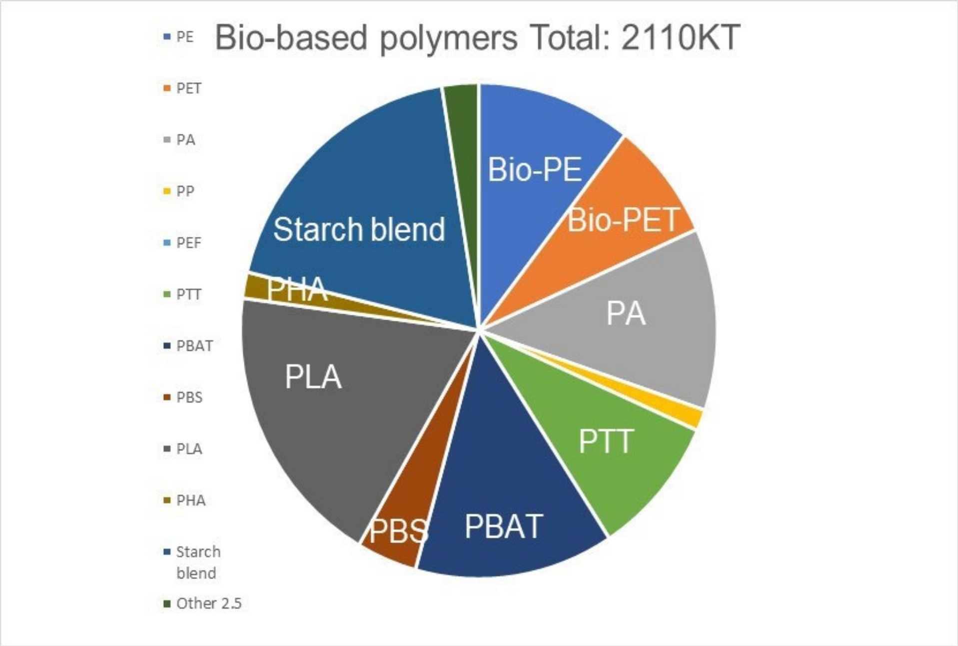

Figure 1. Global production capacities of bio-polymers 2020 (by material type)

PHAs were first discovered by French researcher Maurice Lemoigne in 1926 as a bio-polyester produced by terriers [8]. PHAs are common substances produced by bacteria and stored as energy. PHAs, including poly(lactic acid) (PLA), are fully biodegradable and their structures allow current composting enzymes and bacteria to break them down to form carbon dioxide, water, and humus. Poly(3-hydroxybutyrate) (PHB), also discovered by Lemoigne, is a well-known representative PHA. PHB has a melting point and tensile strength close to those of polypropylene, but a melting point (177°C) close to its pyrolysis temperature (185°C). Therefore, it is difficult to use it as an environmentally friendly thermoplastic owing to its narrow process window. However, PHB has been improved to exhibit physical characteristics suitable for a wider range of applications. Several companies have introduced a second monomer component into PHB and commercialized the product.

The first biomass-based polymer, poly(3-hydroxyburytate-co-3-hydroxyvalerate) (PHBV), was developed by combining another carbon source (propionic acid) with glucose. It was commercialized in the 1980s as Biopol by ICI (Great Britain). Furthermore, Tianjin GreenBio Material (China) commercialized poly(3-hydroxybutyrate-co-4-hydroxybutyrate) (P3HB4HB) [9], and Kaneka Corporation (Japan) developed poly(3-hydroxybutyrate-co-3-hydroxyhexanoate) (PHBH) using 3-hydroxyhexanoate as a second carbon source and commercialized the product under the tradename Green Planet.

Bacterial cellulose (BC), which, like PHAs, is synthesized by bacteria, is almost-pure cellulose that does not contain other foreign substances such as lignin. It is used as the raw material for *nata-de-coco* and in Sony's high-fidelity speakers. However, it is expensive ($30 /kg on a dry basis) [10]. Microorganism-synthesized biopolymers are generally expensive owing to the complexity of their production, which includes complex procedures for their extraction from living organisms. Accordingly, numerous cost-improvement studies are ongoing [11].

PE is the most common and widely produced synthetic polymer globally. It has typically been made from fossil raw materials in the same way as polystyrene and polyvinylchloride. Braskem (Brazil) was the first company in the world to produce bio-PE on a commercial scale. It is made by polymerization of bio-ethylene derived from bio-ethanol, which is a drop-in monomer, using existing polymerization reactors. The price of a barrel of ethanol derived from sugar cane is now competitive with that of a barrel of crude oil, and the price of bio-PE is now only 30% higher than that of petroleum-based PE [12].

PLA is an attractive renewable biodegradable polymer owing to its mechanical strength, high melting temperature, and relatively low cost. It is synthesized by chemical polymerization of lactic acid (LA) obtained from plant resources such as corn, sugar beet, and sugar cane, and it is the most widely used chemically synthesized biopolymer. Cargill Dow LLC commercialized PLA in 2002 under the trade name Nature Works and produces it at a capacity of 140,000 metric tons per year with starch as the starting material [13]. The selling price of PLA, which is polymerized *in vitro*, is $2.2 /kg, much higher than those of petroleum-based PP and PE, and fluctuations in the prices of starch and sugar feedstocks, feedstock pretreatment costs before fermentation, and LA separation and purification process costs after fermentation affect the price of PLA [14].

There are other examples of polymers that use drop-in monomers, including partial ones, as well as polymers obtained from bio-based monomers. For example, Dupont's poly(trimethylene terephthalate) (PTT) containing 1,3-propanediol (1,3-PDO) derived from cornstarch is a partial-biomass plastic polyester. Furthermore, poly(butylene adipate-co-terephthalate) (PBAT) has been obtained by condensation of butanediol (BDO), adipic acid (AA), and terephthalic acid (TPA). The product has excellent properties and is also one of the most produced biodegradable polymers. Bio-based BDO will be obtained through industrial biological fermentation to replace petrochemical BDO in PBAT directly. Sebacic acid from castor oil, as a substitute for AA, has been used as a monomer to prepare polyamide (PA) 610. PA11 produced using 11-aminoundecanoic acid derived from castor oil as a raw material is a fully biomass-based polymer. Bio-polyethylene terephthalate (bio-PET) bottles introduced by Coca Cola and used today are partly bio-based, being made of bio-based ethylene glycol (EG) and petroleum-based TPA. Poly(ethylenefuranoate) (PEF), which is structurally comparable to PET, can be produced from bio-based EG and 2,5-furandicarboxylic acid (FDCA). Furthermore, it has been reported that AA, which is usually made from petroleum-derived cyclohexane, can be obtained from cellulose-derived glucose in two steps [15], while furfural obtained from cellulose biomass can be converted into TPA [16]. Bio-based isobutanol can also be converted into TPA. These partially petroleum-derived polymers have the potential to be replaced by 100% drop-in monomers and to be 100% biopolymeric in the future. Finally, Nippon Shokubai Co., Ltd. very recently announced that biomass-based superabsorbent polymer (SAP) can be produced from acrylic acid derived from biomass-based propylene as the raw material [17].

The overall yields of bio-based monomer production are generally significantly lower than those of the corresponding petroleum-based monomers. Moreover, the production of ethylene from sugar-based ethanol requires decarboxylation and dehydration steps, and the utilization of resources is inefficient. Nevertheless, research into bio-monomers having higher atom efficiencies is expected to yield promising results.

For bio-based polymers to compete with petroleum-based materials, they require not only green-production credentials but also good sources of affordable biomass [18]. The direct utilization of readily available natural polymers as feedstocks for renewable material production is a more sustainable and desirable route to materials that can compete with petroleum-based materials. Among the natural polymers, polysaccharides are the most abundant organic compounds produced by living organisms on our planet. Cellulose and starch are representative polysaccharides and as such have gained much attention in the field of renewable resources. Inexpensive starch (about 10 cents per pound [19]) offers a myriad of possibilities for producing environmentally friendly materials with potential for mass commercial use. To reduce the cost of biomass-based polymer production and to enhance its eco-friendliness and performance, thermoplastic starch (TPS) with a variety of plasticizers has been added to polymers such as PE [20], PHBV, PLA [6, 7], and cellulose nanofiber [21]. NFRCs have been used in numerous fields from household items to industry and military applications, such as those in the automobile, railway, aerospace, marine, electronics, packaging, and construction industries. Furthermore, the use of natural fibers makes the parts lighter than those produced using glass fibers and improves the fuel economy of cars, thus reducing the consumption of fossil resources. Car manufacturers and suppliers use cellulose-fiber composites in a variety of automobile parts, such as seat-backs, window panels, door panels, packaging trays, and dashboards. The Mercedes-Benz E-Class, announced in 2016, saw an increase in the total weight of components manufactured using renewable raw materials of 59%. In the same year, Toyota unveiled a concept car, the Setsuna, with a body consisting of 86 wood panels. Furthermore, those parts can be easily replaced when repairs are needed. No nails or screws are used to join the wood panels, and traditional Japanese joinery techniques called *okuriari* and *kusabi* are used to assemble the car. Thus, the Setsuna could be considered the ultimate example of the application of biomass-based polymers in terms of utilizing raw materials. Figure 2 shows some automobile components made of NFRCs.

https://www.daimler.com/documents/sustainability/product/

https://global.toyota/jp/detail/11538726

Figure 2. Automobile components made of NFRCs

CMC was first prepared in 1918 and produced commercially in the early 1920s in Germany. CMC is an anionic, water-soluble derivative of cellulose and has been used in a wide range of applications in the biomedical, pharmaceutical, textile, construction, food, plastics, cosmetics, paper, and oil industries [22]. According to a CMC chemical profile reported by the Independent Commodity Intelligence Services in 2005, the global production of CMC stood at 360,000 metric tons/year [23] and its price ranged from €4.6 to €2 /kg depending on application.

CA is a modified natural polymer prepared by acetylating cellulose. It was first prepared in 1865 by Schützenberger, and it was widely produced commercially as films, sheets, and rod-material molding powders in the first half of the 20th century. It is tough and can be obtained as a transparent thermoplastic in a full range of colors. Having a natural feel, it is still used for tool handles and spectacle frames. CA can be easily dissolved in various organic solvents and is easier to modify than cellulose owing to the acetate groups, which effectively disrupt the strong hydrogen bonding between cellulose molecules. It is relatively cheap ($2.5 /kg) [24] and widely available, with an annual production of nearly one million metric tons [23, 24]. Thus, few plastics can boast similar pedigrees to those of CA and CMC. Biomass-based polymers that have been used for such a long period of time are rare and can be said to be champions of biomass-based polymers. Highly active research on lower-cost methods of obtaining modified cellulose, for example, utilizing discarded industrial waste [22, 25] as a cellulose resource, is ongoing.

The greenest processes for a manufacture of sustainable products are considered to be those that use waste as a renewable source [26]. These examples suggest that alternative resources such as wastes are important means to obtain sustainable and practical material. Table 1 summarizes the characteristics of the biomass-based polymers obtained from the three routes described above.

Table 1. Three routes from biomass to bio-polymers, characteristics, and challenges

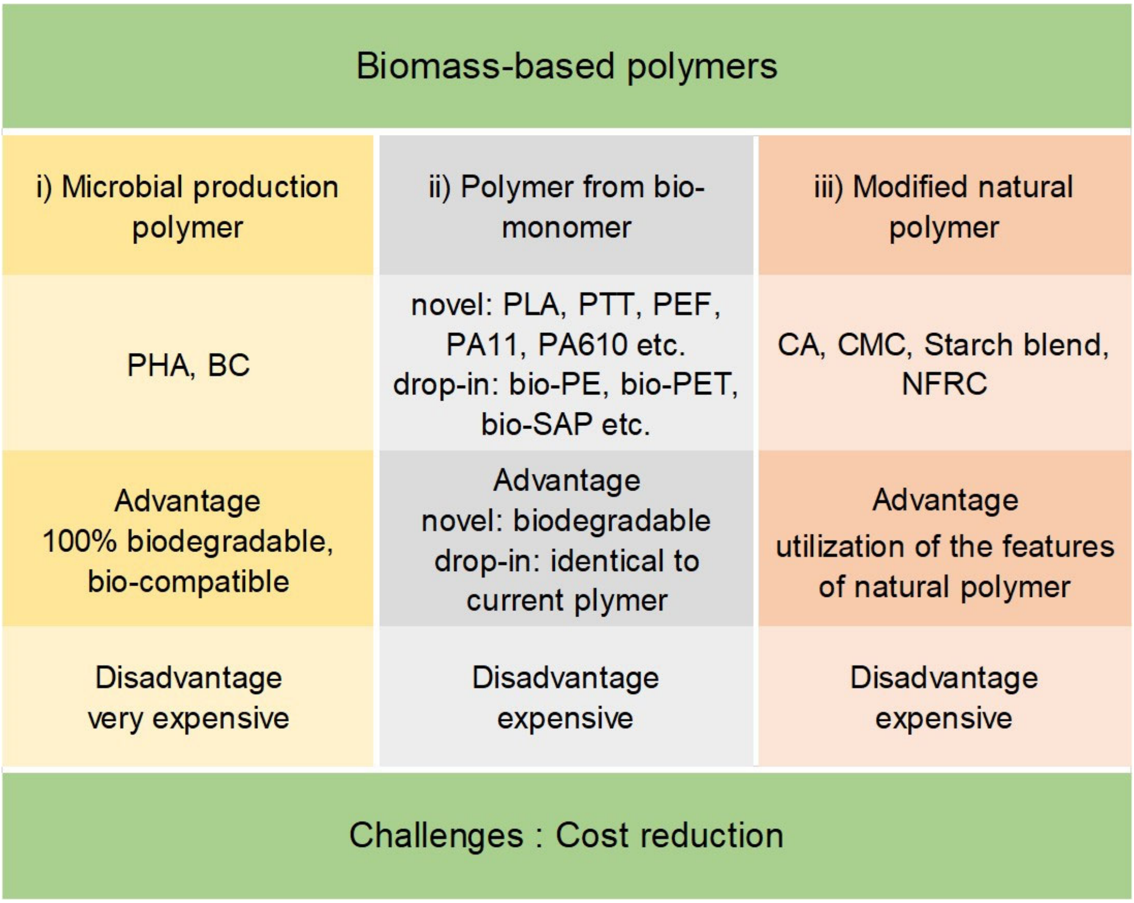

Biomass-based polymers		
i) Microbial production polymer	ii) Polymer from bio-monomer	iii) Modified natural polymer
PHA, BC	novel: PLA, PTT, PEF, PA11, PA610 etc. drop-in: bio-PE, bio-PET, bio-SAP etc.	CA, CMC, Starch blend, NFRC
Advantage 100% biodegradable, bio-compatible	Advantage novel: biodegradable drop-in: identical to current plymer	Advantage utilization of the features of natural polymer
Disadvantage very expensive	Disadvantage expensive	Disadvantage expensive
Challenges : Cost reduction		

Although the production scale and popularity of bio-based polymers is increasing, their price remains a significant barrier to their widespread use. According to the current status of the three types of biomass-based polymers mentioned above, it is essential that they be made from abundant and inexpensive raw materials at low cost by green processes utilizing inexhaustible waste resources if we are to fully realize sustainable and practical materials.

The valorization of harmful waste materials has three main advantages: The first is that wastes can be used as raw materials directly without the cultivation of dedicated biomass; the second is that the disposal costs for the waste itself are avoided; and the third is that it prevents the release of substances harmful to ecosystems.

Cigarette filters (CFs) are among the most-collected types of refuse recovered by beach cleanup campaigns around the world every year (Ocean Conservancy Reports 2010–2020). One CF contains enough toxic substances to contaminate 1000 L water to concentrations above their predicted no effect concentrations [27]. Thus, CFs pose a serious threat to aquatic animals, human beings and our environment. Approximately 84% of the CA produced in 2008 was used for the production of filtered cigarettes [28]. Furthermore, many smokers do not recognize cigarette butts as being harmful refuse. CA from recovered CFs has the potential to be used as a free raw material for other useful functional products, thus preventing environmental damage. Accordingly, the work presented in this thesis concerns the use of CA recoverable from hazardous waste and inexpensive starch as starting materials for the manufacture of sustainable and practical materials.

This thesis is composed of 6 chapters.

Outline of this thesis

In this thesis, the author presents their work on preparing **sustainable and practical materials using starch and CA**.

Chapter 1. A simple and energy-saving preparation of starch phosphate carbamate particles by a green, wasteless process

This chapter describes the conversion of starch, an inexpensive raw material, into useful compounds without waste emission. A novel method for preparing hydrogel-forming starch phosphate carbamate (SPC) particles and their potential applications are presented. SPC particles were prepared from gel particles consisting of a mixture of starch, urea, and aqueous phosphate solution by heating. The performance of SPC obtained by the method presented in this chapter was compared with that of SPC obtained by the conventional method. The SPC was obtained with high reaction efficiency and exhibited an excellent balance between water absorption capacity and shear modulus. The effect of hydrogels on plant growth was investigated by the seeding test based on the Fertilizer Control Law, and the green SPC particles having no washing process showed better results than poly(acrylate)-based SAP particles. These results demonstrate the potential for the social implementation of this product.

Chapter 2. Macroporous cellulose beads prepared via a non-solvent induced phase separation method from a CA solution

This chapter describes a fabrication method for macroporous cellulose beads (MCBs) with a three-dimensionally interconnected porous structure from a cellulose acetate solution in a single step through a non-solvent-induced phase separation (NIPS) method. The obtained beads absorb water as quickly as the fluff pulp used in diapers, and the water absorbency and stiffness of the beads can be controlled by simply changing the CA concentration in their preparation. The fluidity of the beads in water is superior to that of current fluff pulp and thus the beads have the potential to be applied to toilet-flushable diapers, which have not yet been realized. Similar results were obtained with CA recovered from CFs, demonstrating that this technique can be applied to valorization strategies.

Chapter 3. A simple fabrication method and environmental applications of activated-carbon-containing porous cellulose beads

The NIPS method used in Chapter 2 for preparing the MCBs was extended to the preparation of activated carbon (AC)-containing porous cellulose beads (ACPBs) in this chapter. The adsorption behavior of the obtained ACPBs was evaluated using toluidine blue (TB) dye as a model adsorbate. The ACPBs retain their original shape and adsorption capacity over three times of TB adsorption/desorption cycles. Furthermore, the ACPBs efficiently remove malodorous gases from gas mixtures, again indicating their potential for use in diapers. Activated carbon is known to be useful for controlling odors, but black deodorants are not esthetically suitable for diapers, thus the possibility of white activated carbon was also investigated.

Chapter 4. Preparation and characterization of water-swellable hydrogel-forming porous cellulose beads

A cellulose-based water-swellable hydrogel was obtained by applying the method described in Chapter 1 to the microporous cellulose beads in Chapter 2. The obtained water-swellable hydrogel-forming porous cellulose beads (HFPCBs) maintained the interconnected porous structure during processing. The HFPCBs showed a maximum centrifuge retention capacity of approximately 50 g/g in deionized water. Despite their highly porous structure, HFPCBs had a compressive strength of several tens of kilopascal in the swollen state. To demonstrate their potential application, the swollen HFPCBs were successfully used for the germination of plant seeds.

Chapter 5. Study on the penetration of singlet oxygen into films having an oxygen permeability coefficient close to that of skin

The coronavirus disease 2019 (COVID-19) pandemic has become one of the biggest issues of the present world. It is known that singlet oxygen ($^1O_2$) generated by a photoexcited photosensitizer (PS) inactivates the influenza virus due to the loss of infectivity by "bald" virions caused by the detachment of spike proteins [29]. Accordingly, the use of films that generate $^1O_2$ is considered to be a promising strategy for the prevention of pandemics. Because CA has oxygen permeability, it is also useful as a substrate for producing $^1O_2$ from oxygen. Before developing an antiviral film using a CA film containing a PS that was already known to release $^1O_2$ upon being irradiated with visible light, in this chapter, the effects of the emitted $^1O_2$ on human skin were investigated by detecting the invasion of $^1O_2$ into a film with an oxygen permeability similar to that of skin. The results demonstrated that the potential for $^1O_2$ to penetrate the skin is very low and that the film is safe for humans.

Chapter 6. Fabrication and evaluation of durable, optically clear, and self-disinfecting films

This chapter presents the fabrication of an optically clear film by incorporating phenoxy-substituted phthalocyanine zinc (PPcZn) into a CA film. The film generates $^1O_2$ under visible-light irradiation, and it exhibited activity against viruses attached to its surface. Even after six months indoor exposure, it maintained excellent durability in terms of $^1O_2$ generation ability, transparency, and mechanical strength. The self-disinfecting film was easily folded into various shapes, and it is expected to be used for consumer-goods packaging that requires antiviral properties.

Chapter 1

A simple and energy-saving fabrication of starch phosphate carbamate particles by a green, wasteless process

1.1 Introduction

Superabsorbent polymers (SAPs) having three-dimensionally crosslinked hydrophilic polymer networks, are capable of reversibly swelling or dehydrating and retaining a large amount of water in a swollen state. They are used in various fields such as personal care, agriculture, civil engineering, and medicine [30, 31]. Most SAPs currently available are made from petroleum-derived acrylic acid [30, 32]. In recent years, there is an increasing attention to replacement of petroleum-derived resources with renewable resources due to concerns about global warming and depletion of fossil fuels [30]. Interest in biodegradability is also growing since non-degradable plastics are causing serious environmental and health problems worldwide [32]. To shift from a petroleum-based SAP to a sustainable one using eco-friendly materials and to meet the requirement of the biodegradability and compostable ability of the material are social requirement. Polysaccharides are promising raw materials for future SAP because they are not only renewable and biodegradable but also non-toxic and biocompatible.

Starch is an inexpensive polysaccharide and the second most abundant next to cellulose. It has lower crystallinity than cellulose, and is relatively easy to be chemically modified. Use of starch as a raw material for SAPs has been reported, which includes hydrolyzed starch–polyacrylonitrile graft copolymer [33], hydrolyzed product of starch–polyacrylonitrile physical mixture [34], crosslinked carboxymethyl starch [35, 36], crosslinked oxidized starch [37], crosslinked starch phosphate [38, 39], crosslinked starch carbamate [40], and starch phosphate carbamate (SPC) [41, 42]. Especially, SPC is a unique modified starch with partially crosslinked structure and has a potential to be a feasible alternative to polyacrylates due to its good physicochemical behavior and ease of preparation with safe ingredients. SPC shows not only good water absorbency [43-45], but also ion absorbing power [46], and flame retardancy [47]. SPC has been prepared by thermally reacting starch with urea and phosphoric acid or phosphate using solid- or paste- state technology in vacuo [43]. In the reaction, substitutions of hydroxyl groups of starch with carbamoyl groups and phosphate groups take place simultaneously. The properties of SPC are significantly affected by the degree of substitution with phosphate groups (DSp) and that with carbamate groups (DSc) [44, 45, 48]. It has been also reported that crosslinking reaction proceeds between two carbamoyl groups and/or between hydroxyl group and carbamoyl group accompanying liberation of ammonia [40]. This study aims to develop a simpler and more economical preparation method of SPC with improved physical properties. In one of the reported preparation methods of SPC, the reaction mixture is heated as a paste (P-SPC). In the new method described in this report, the paste is allowed to gel, pulverized into particles, and heated under ambient pressure (G-SPC). The chemical structure, time dependence of the reaction, and the physical properties of G-SPC will be discussed. Additionally, from the perspective of the green process, we also obtained G-SPC particle without washing process after the reaction and will be compared with commercially available petroleum-derived SAP for the effect of adding hydrogels on plant growth.

1.2 Experiment

1.2.1 Materials

Cornstarch was purchased from Kanto Chemical Co., Inc, (Tokyo, Japan). Urea, sodium dihydrogen phosphate dihydrate (SDP), sodium chloride, 0.01 M NaOH, and methanol were purchased from Fujifilm Wako Pure Chemical Co. (Osaka, Japan). Commercially available polyacrylate-based SAP （Acryhope GH-2） was obtained from Nippon Shokubai Co., Ltd. All chemicals and reagents were of analytical grade and used without further purification.

1.2.2 Measurement

Fourier-transform infrared (FTIR) spectroscopic measurements with attenuated total reflectance were performed using an FT/IR-6200 type A system (JASCO Co., Easton, MD, USA). Nitrogen content was determined using an elemental analyzer (JM10; J-Science Lab Co., Ltd., Kyoto, Japan). Phosphorus content in samples was determined by inductively coupled plasma optical emission spectroscopy (ICP-OES) using an ICP-OES analyzer (OPTIMA 8300; PerkinElmer, Waltham, MA, USA). For the measurement, an aqueous solution of the sample was prepared with nitric acid using a pressure acid-decomposition apparatus (ETHOS 1600; Milestone, Sorisole, Italy). Stereomicroscopic and scanning electron microscopic (SEM) images were obtained by a stereo microscope (MS4572; Carton Optical Industries, Inc., Tokyo, Japan), and a Miniscope TM3000 (Hitachi, Tokyo, Japan) at 15 kV, respectively. XRD analysis was performed on an X-ray diffractometer (Smartlab; Rigaku, Tokyo, Japan) using Cu-Kα radiation at a 2θ range from 10° to 40°, with the voltage and current set to 45 kV and 200 mA, respectively. The surface area of the product was measured by Brunauer-, Emmett-Teller (BET) instrument (BELSORP-MR6; Microtrac BEL Corp., Osaka, Japan). Rheological properties were evaluated using an MCR301 rheometer (Anton Paar GmbH, Graz, Austria) with parallel-plate geometry (50 mm diameter). The measurement was performed under the following conditions: temperature 25°C, load 0.3 psi, strain 0.1%, frequency 10 rad/s. Prior to the measurement, SPC (0.20 g) was weighed, moistened with 5.0 mL of deionized water, and allowed to stand for 15 min.

1.2.3 SPC preparation

For the preparation of G-SPC, an aqueous solution of SDP was added to a mixture of cornstarch and urea with gentle stirring at ambient temperature to yield a homogeneous paste. The paste was allowed to stand until gelation and pulverized into small particles with a spatula. The obtained particles were spread on a Teflon sheet, and heated at 145 °C under ambient pressure (Figure 1-1).

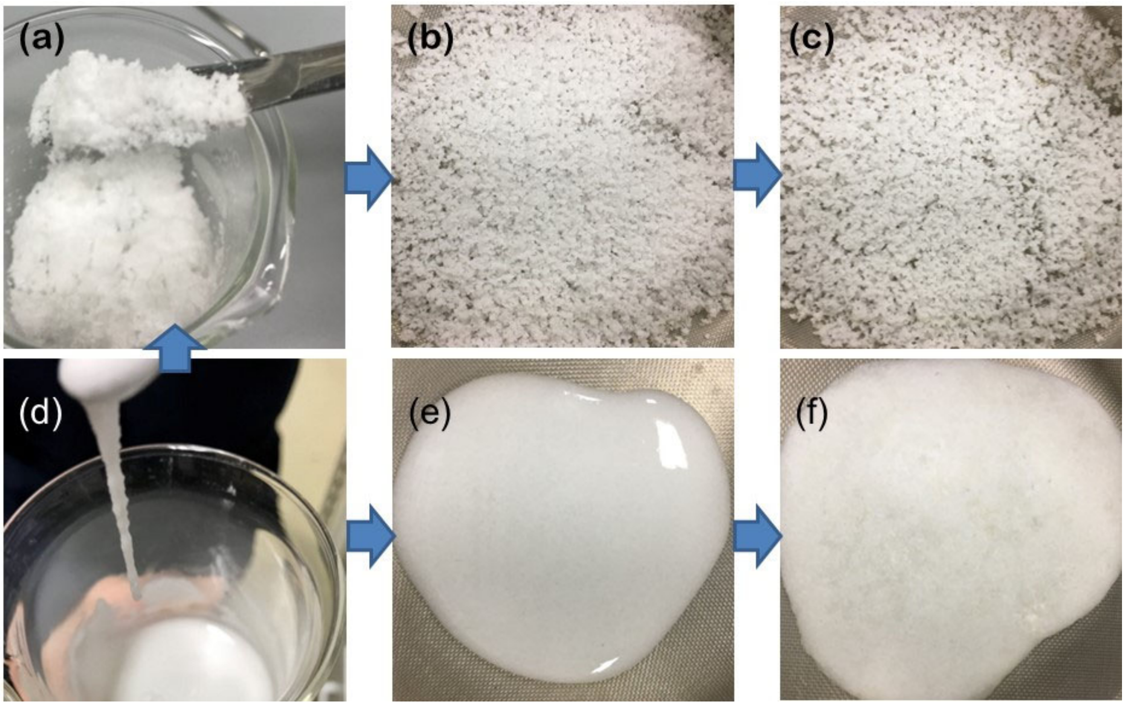

Figure 1-1. Preparation of G-SPC ((a)-(c)) and P-SPC ((d)-(f)); pulverized gel (a), paste (d), before baking ((b) and (e)), after baking ((c) and (f))

After heating, G-SPC did not require mechanical pulverization step because it was reacted already in the form of particles. For comparison, P-SPC was prepared by directly heating the homogeneous paste, followed by mechanical pulverization. All SPC samples except for the green-process sample used for the plant growth test were washed with a methanol-water mixture (volumetric ratio, 3:1) and subsequently pure methanol, and dried *in vacuo*. The reactions were performed with varying reaction time at the same molar ratio of the reactants (Table 1-1).

Table 1-1. Effect of reaction time on degree of substitution

Sample	Time (min)	P (%)	N (%)	DSp	DSc
G-SPC1	10	4.82	0.76	0.32	0.11
G-SPC2	15	4.96	1.24	0.34	0.19
G-SPC3	20	4.65	1.62	0.32	0.25
P-SPC1	25	4.89	0.43	0.32	0.06
P-SPC2	40	4.83	0.86	0.32	0.13

[a] Molar feed ratio of AGU : urea : SDP =1.0 : 4.0 : 0.4 (AGU: anhydroglucose unit)

1.2.4 Measurement of water absorbency

Centrifuge retention capacity in deionized water (CRCw) was measured according to the EDANA method (ERT 441.2-02). Specifically, 0.050 g of SPC was placed in a non-woven bag and then immersed in an excess of deionized water for 30 min to allow free swelling, followed by centrifugation at 250. CRCw is calculated by the following equation:

$$\text{CRCw (g/g)} = (W_1 - W_0)/W_0 \qquad (1\text{-}1)$$

where W_0 and W_1 are the dry and wet weights of SPC, respectively. Centrifuge retention capacity in saline (CRCs) was measured using 0.90 wt% sodium chloride aqueous solution instead of a deionized water. For CRCs, 0.20 g of SPC was used.

1.2.5 Germination and initial growth test

G-SPC4 particles was prepared by heating for 12 minutes with the same composition as G-SPC1 without washing process. CRCw value of G-SPC4 and Acryhope GH-2 were 34 g/g and 200 g/g, respectively. The effects on germination and initial growth were confirmed by seedling tests according to the Fertilizer Control Law. Two types of irrigation conditions were set to examine the effect of the material due to the difference in soil water content. During the cultivation period, the plots given 60% irrigation were designated as constant irrigation plots, and the plots 30% reduced irrigation from the 14th to 21st days were designated as water-saving plots. 400 mL (540 g) of decomposed granite soil passed through a 2 mm sieve into a Neubawell pot (650 ml). Pots were filled with 0.54 g of G-SPC4 or GH-2 (equivalent to 0.1% of 540 g of soil) and mixed with the soil. On top of that, 25 seeds of Komatsuna (variety; Hamami No. 2, Sakata Seed Corporation) were sown and covered with 70 g of sand soil. Irrigation was carried out once a day until the 13th day after sowing and twice a day from the 14th day to the 21st day, and tap water was given to the standard amount while measuring the weight using an electric spray. The germinated Komatsuna was thinned out by leaving 9 strains of moderately growing individuals on the 7th day. Each test was conducted 3 pots under the same conditions.

1.3 Results and discussion

1.3.1 Characterization of G-SPC and P-SPC

By reacting starch with SDP and urea, a substitution reaction of hydroxyl groups of starch with phosphate groups as well as with carbamoyl groups took place and a crosslinking reaction simultaneously proceeded between two carbamoyl groups and/or between hydroxyl group and carbamoyl group (Scheme 1-1) [40, 43].

Figure 1-2 shows FTIR spectra of G-SPCs with different reaction time in Table 1-1 in comparison with those of cornstarch and alkali treated G-SPC3. The alkali treatment was carried out by immersion of G-SPC3 in an excess amount of 0.01M NaOH for 1h, followed by the same washing and drying procedure for the preparation of the SPC samples. The broad band at 3390 cm^{-1} originated from the vibration of the hydroxyl groups decreased in G-SPCs, indicating that the substitution occurred at hydroxyl groups.

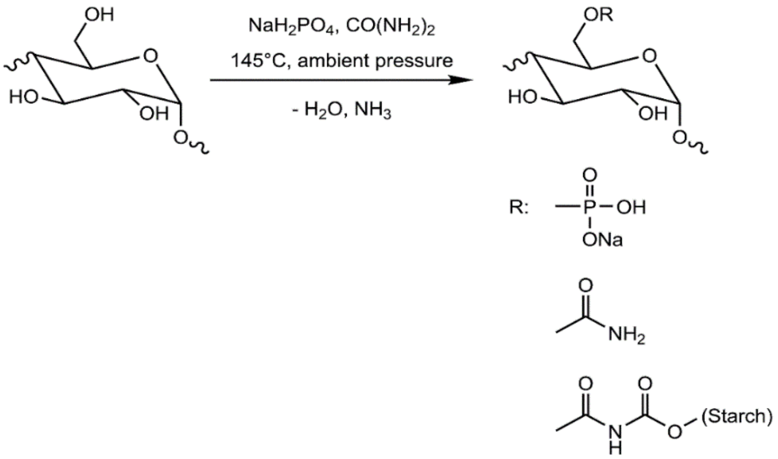

Scheme 1-1. Reaction of starch with SDP and urea

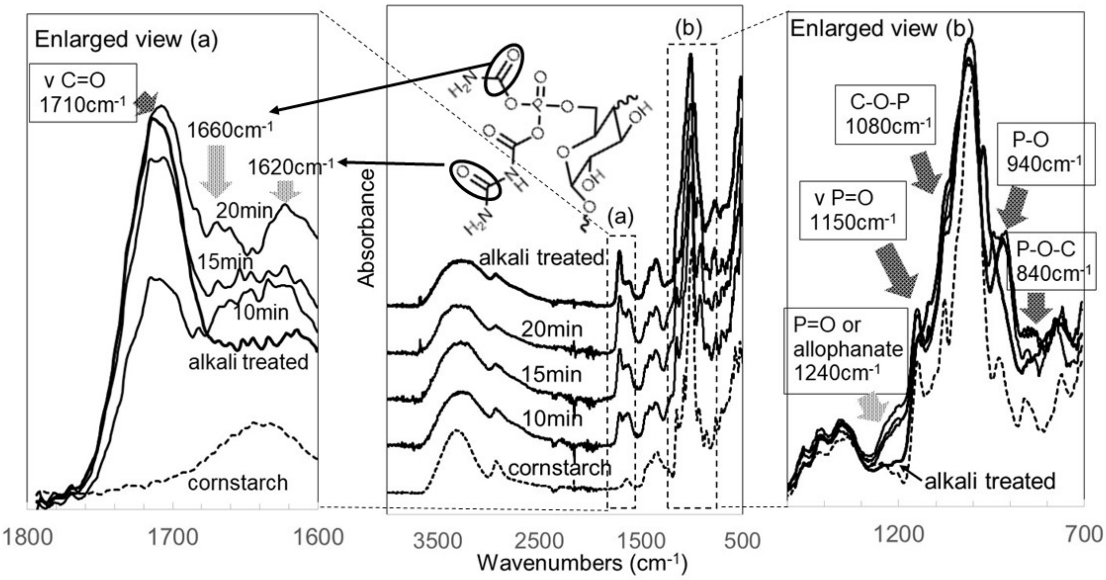

Figure 1-2. IR spectroscopy of cornstarch and G-SPCs with different reaction times

A characteristic strong band at 1710 cm^{-1} attributed to C=O of starch carbamate [43] appeared in G-SPCs and the intensity of the band increased with the reaction time. In the preparation of G-SPC, the weight of the reaction mixture decreased by 20 wt%, 23 wt%, and 25 wt% at the reaction times of 10 min, 15 min, and 20 min, respectively presumably due to evaporation of water and decomposition of urea. It is supposed that carbamoyl groups were formed by the reaction of isocyanic acid generated during the significant decomposition of urea with hydroxyl groups of starch. The absorption strength of bands at 1660 cm^{-1}, 1620cm^{-1}, and 1240 cm^{-1} was greatly reduced by the alkali treatment. The band at 1660 cm^{-1} is attributed to C=O of carbamoyl phosphate starch because carbamoyl group attached to a phosphorus atom has a lower absorption frequency than that attached to a carbon atom due to lower electronegativity of a phosphorus atom [41]. The band at 1620cm^{-1} is due to the second C=O of allophanate that was formed by addition of isocyanic acid with carbamate phosphate starch [49]. The shift of absorption frequency from 1660 cm^{-1} to 1620 cm^{-1} may be explained by resonance effect from the adjacent nitrogen atoms. Ammonium carbamate, which has an absorption at around 1540 cm^{-1}, is an extreme example of the effect [50]. The rather broad band centered at 1240 cm^{-1} is assigned to P=O of carbamate phosphate starch and/or allophanate groups. The absorption of P=O of carbamate phosphate starch shifted to higher frequency by the adjacent carbamoyl group [49, 51]. All the bands attributed to carbamoyl groups bonded to phosphate starch almost disappeared upon the alkali treatment, while the intensity of the band at 1710 cm^{-1} attributed to C=O of starch carbamate kept at the same level. The result indicates that carbamoyl groups attached to phosphate groups were hydrolyzed but the carbamoyl groups directly bonded to starch were not hydrolyzed under the alkaline condition. Phosphorylation was confirmed by the new bands at 1150 cm^{-1}, 1080 cm^{-1}, 940 cm^{-1}, 840 cm^{-1} corresponding to P=O, C-O-P, P-O, P-O-C of phosphates, respectively [39, 43, 51-53]. While the intensity of the band at 1660 cm^{-1} derived from C=O of carbamoyl group bonded to phosphate groups and the band at 1620 cm^{-1} attributed to C=O of allophanate increased with time, the intensity of the bands derived from the phosphate group remained almost constant. The result indicates that most of the phosphorylation reaction took place in starch gelatinized by urea before urea starts to decompose.

To avoid overestimation of the content of carbamoyl groups and phosphate groups and make all phosphate groups of the SPC in the form of sodium salt before measuring the content of nitrogen and phosphorus, the product was immersed in excess 0.01 M NaOH for 1 h, subsequently followed by the same washing and drying as described in the preparation of the SPC samples. The DS with disodium phosphate monoester groups (DSp) and that with carbamoyl groups (DSc) are calculated by equations (1-2) and (1-3), respectively, according to the report by Touzinsky on cellulose derivatives containing two or more different substituent groups [54];

$$\mathrm{DSp} = \frac{\dfrac{P \times 162}{31 \times 1}}{100 - \dfrac{P \times 124}{31 \times 1} - \dfrac{N \times 43}{14 \times 1}} \qquad (1-2)$$

$$\mathrm{DSc} = \frac{\dfrac{N \times 162}{14 \times 1}}{100 - \dfrac{P \times 124}{31 \times 1} - \dfrac{N \times 43}{14 \times 1}} \qquad (1-3)$$

where, *P*, *N*, 162, 31, 14, 124, 43, and 1 represent wt% values for SPC phosphorus content, wt% values for SPC nitrogen content, the molar mass of an anhydroglucose unit, the atomic weight of P, the atomic weight of N, the molar mass of the disodium phosphate group minus 1, the molar mass of the carbamoyl group minus 1, and the number of phosphorus and nitrogen atoms in the respective substituent, respectively. The measured total content of phosphorus and nitrogen and the calculated DSp and DSc are shown in Table 1-1.

Values of DSc increased along with increasing reaction time, whereas DSp values remained almost the same, indicating that phosphorylation reached the maximum at an early stage. This trend was in good agreement with that of the IR data. The products obtained in the current reaction provided the same degree of substitution as those obtained in the solid-state reaction with similar compositions with an order of magnitude shorter reaction time [43, 55].

The specific surface areas of 600-300 μm fractions of G-SPC2 and P-SPC1 particles were 1.54 m^2/g and 0.94 m^2/g, respectively. Specific surface area of G-SPC was 60 % higher than that of P-SPC at the same particle size. An average particle size of corn starch was around 15 μm, and its specific surface area was only 0.54 m^2/g even though the particle size is finer than SPCs. Figure 3 shows SEM images of G-SPC2 particles and P-SPC1 particles. G-SPC2 particles were relatively round and had numerous pores presumably formed by evaporation of ammonia gas generated by urea decomposition during the reaction. On the other hand, the reaction mixture of P-SPC1, which was in the paste form, became a hard plate-like material after the reaction and cooling. The particles of P-SPC1 obtained by mechanical crushing of the material had surfaces with few holes. It is considered that ammonia evaporation of P-SPC was suppressed by the rigid surface of the plate-like material formed in the early stage of the reaction. SPCs obtained by solid-state technology have been reported to contain native starch particles in the diameter between 5 μm and 20 μm [46]. Neither G-SPC nor P-SPC contained native starch particles, while they had granular size that would require agglomeration of starch particles. Absence of fine particles is desirable because SAP fines of less than 100 microns in diameter are not useful in practical applications [56, 57].

Figure 1-3 (c) shows stereomicroscopic image of a swollen G-SPC2 particle colored by aqueous iodine solution. The swollen particle consisted of bluish-purple domains and a yellow domain. The former domain is attributed to an amylose-iodine complex. No complex with iodine was formed in the latter domain presumably because the helix structures originally present in starch were lost as a result of reaction with urea and SDP. In the XRD spectrum of G-SPC2, distinct peaks at diffraction angles of 15°, 23°, and dual peaks at 17° and 18° observed in native cornstarch disappeared (Figure 1-4). The result indicates that most of the crystalline structure was converted to an amorphous structure in the course of the reaction, which is in agreement with the observation by stereomicroscopy [39].

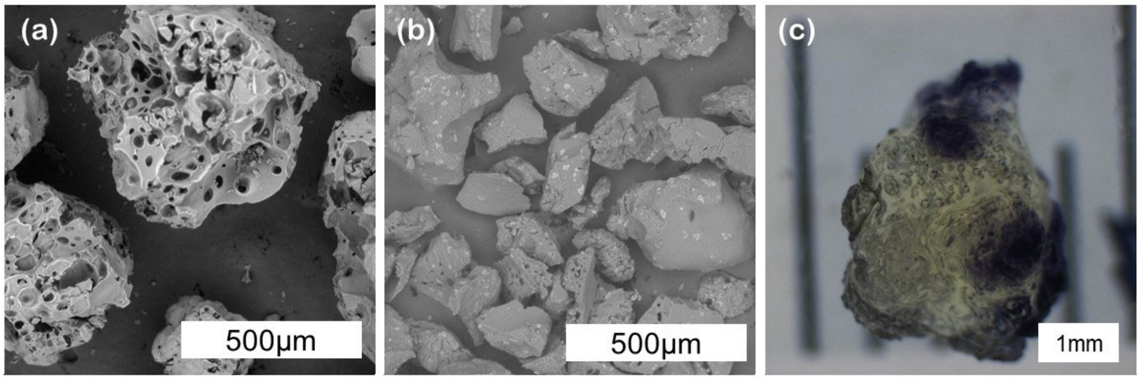

Figure 1-3. SEM images of G-SPC2 (a) and P-SPC1 (b) and stereomicroscopic image of swollen G-SPC2 (c)

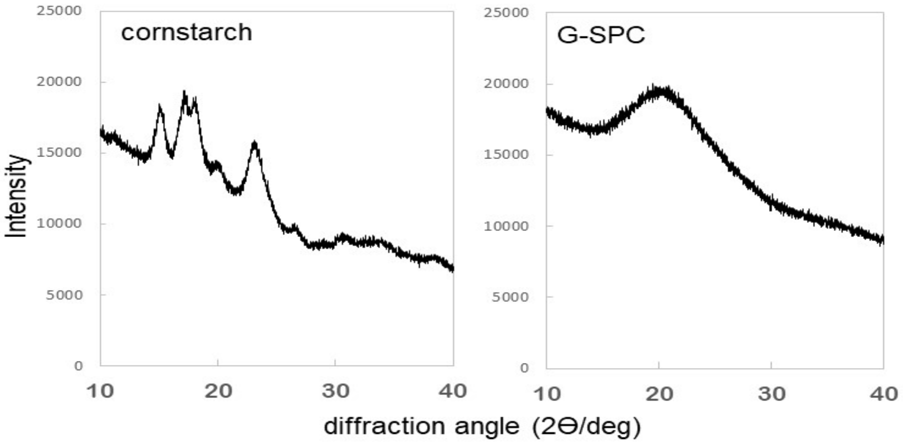

Figure 1-4. XRD traces of cornstarch and G-SPC2

1.3.2 Effect of reaction time on water absorbency of G-SPC and P-SPC

Figure 1-5 shows the reaction time dependence of water absorbency. For both G-SPC and P-SPC, CRCw increased with reaction time, reached the maximum and decreased. CRCs of G-SPC also exhibited a similar trend. In the thermal reaction of starch with urea, it has been reported that once a sufficient amount of starch carbamate was formed, the crosslinking reactions became predominant. The solubility of starch carbamate was governed by the magnitude of crosslinking [40]. The CRCw trace of G-SPC was comparable with that of P-SPC. However, the process of G-SPC was more efficient as the reaction proceeded significantly faster.

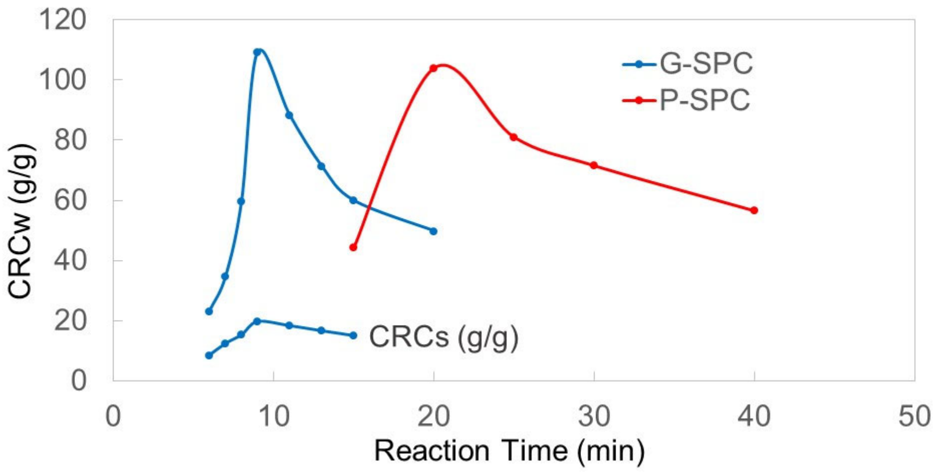

Figure 1-5. Reaction time dependence of water absorbency (CRCw)

1.3.3 Rheological properties of G-SPC and P-SPC

Figure 1-6 shows the relationship between water absorbency and shear modulus (*G*’). Noticeably, *G*’ of G-SPC was 30 % higher than that of P-SPC at the same water absorbency level. Particularly, for CRCw above 100g/g, *G*' of G-SPC was more than three times larger than that of P-SPC. We suppose that G-SPC was heated more uniformly than

P-SPC due to its particulate form as indicated by higher DSc (Table 1-1) and presumably less variation in substitutions between final particles, leading to high *G*'.

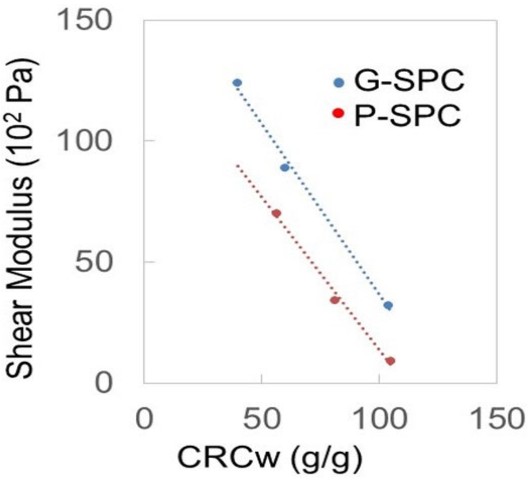

Figure 1-6. Relationship between water absorbency and shear modulus

1.3.4 The effect of SAPs on plant growth

Figure 1-7 shows the result of the germination and growth of the Komatuna under the two irrigation conditions after 21 days. The use of SAPs in plant growth has several benefits, such as conservation of water, soil amendment, reducing the consumption of soil nutrients, lowering surface runoff, avoiding soil erosion, minimizing the negative impacts of dehydration and moisture stress in crops, controlling several phytopathogens [58]. For both GH-2 and G-SPC4, the growth of Komatuna was promoted compared to the case without SAP, and the difference seemed to be larger especially under the condition of lower irrigation. More notably, the addition of G-SPC4 significantly promoted the growth of Komatsuna. The land used to grow the renewable feedstock for the production of biomass-based polymer has been estimated at approximately 0.70 million hectares in 2020 and it has accounted for less than 0.02 % of the global agriculture area of 4.7 billion hectares [4]. Although there seems to be no competition between the renewable feedstock for food and the production of biomass-based polymer, starch-based G-SPC4 obtained by a green process comprising no washing and no waste process may have a potential to turn a semiarid place into a farmland.

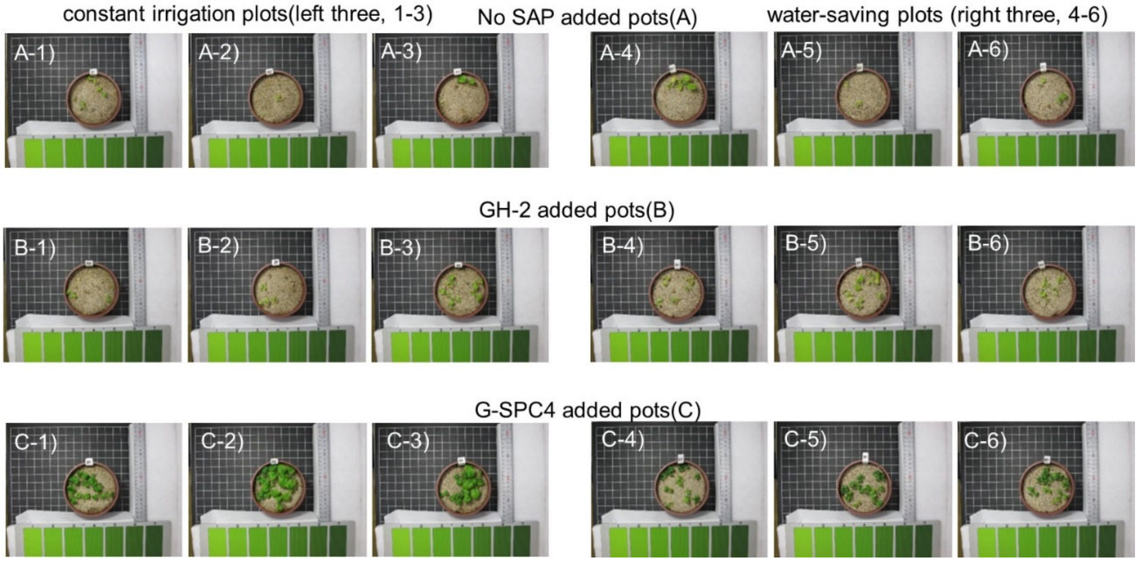

Figure 1-7. The growing state of Komatsuna after 21 days; (A) without SAP, (B) with GH-2, (C) with G-SPC4; (1-3) constant irrigation, (4-6) water-saving

1.4 Conclusion

In this chapter, a novel preparation method of SPCs was described and characterized in that the reaction mixture of starch, urea, and an aqueous phosphate solution was heated in the form of gel particles under ambient pressure. The method was compared with the method in which the reaction mixture is heated in the form of paste from the standpoint of process efficiency and product features. In comparison with P-SPC, G-SPC required shorter reaction time, i.e., lower production energy, and exhibited higher elastic modulus and higher surface area arising from porous morphology. SPC is an attractive material as it is sustainable, biodegradable, and made from inexpensive and safe raw materials. The effect of adding hydrogels on plant growth was confirmed by the seeding test based on the Fertilizer Control Law and SPC particles, which obtained as reactant without washing (no wastes), showed better result than polyacrylate-based SAP particles. Ammonia generated in making SPC can also be recovered as ammonium sulfate useful as fertilizer by trapping it with a dilute aqueous sulfuric acid. Although the adoption of dedicate crops for the biomass-based products has some limitations, this product may provide a way to increase biomass raw materials in places that were previously unavailable. These results are attractive toward social implementation of this product and may be useful to support good circulation of Biomass-based polymers by applying G-SPC to plant growth.

Chapter 2

Macroporous cellulose beads prepared via a non-solvent induced phase separation method from a CA solution

2.1 Introduction

In recent years, application developments of renewable materials have been required in various fields from the viewpoint of resource problems, waste treatment technologies, environmental conservation, and sustainable society. Cellulose widely distributed on the earth is the largest production polymer prepared by creatures on the earth and one of the most typical renewable polymer resources. Since cellulose is clean and circulates, it is also the ultimate polymeric material that is not depleted on the earth. Cellulose is a hydrophilic, chemically and physically stable compound, and various functional groups can be chemically introduced on its surface by modification.

Polymer monoliths are unitary porous materials having a bi-continuous structure in which material skeletons and void spaces are three-dimensionally connected. For preparing polymer monoliths, some methods utilizing phase separation of a polymer solution have been developed as follows: polymerization induced phase separation in which the phase separation takes place together with a polymerization reaction [59-61]; NIPS (non-solvent induced phase separation) in which the phase separation proceeds by addition of a poor solvent to the polymer solution with a good solvent [62-64]; TIPS (thermally induced phase separation) involving the phase separation by utilizing the different solubility of the polymer with a temperature change [65-68]. Among them, the TIPS method is highly useful for the monolith fabrication because the procedures consisting of heating and cooling steps are simple.

Porous cellulose monoliths are attractive functional materials by combination of unique characteristic properties of cellulose and monoliths; porous cellulose can be applied to adsorbents, enzyme immobilization matrices [69], catalyst carriers [65, 70], chromatography fillers [71], ion exchange resins [68, 72], and water treatment membranes [73] by utilizing the high specific surface area of the matrix and chemical modification of cellulose [67]. So far, several methods for preparation of cellulose monoliths have been reported: dropping a cellulose acetate (CA) solution into an aqueous medium [69]; dropping a CA solution into an organic solvent [74]; use of a cellulose ionic liquid for the phase separation [75]; coagulation of an alkali/urea solution of cellulose [76]; bulk method by TIPS [66].

Disk or column shape monoliths are often prepared for their applications. Because mechanical properties of porous materials are often weaker than those of bulk ones, careful handling of monoliths in such shapes is required, which sometimes restricts their potential applications. An easily handled shape for porous materials is spherical as popularly seen in most ion exchange resins.

Cigarette filters (CFs) are the most frequently littered pieces of environmental wastes which are released both directly and indirectly into the environment and have risks for our planet. Most CFs are formed from CA and the regenerated CA recovered from the used CFs can also be useful as a biomass raw material and their recycling contributes to the better ecosystem.

In this study, we provide a novel fabrication method for macroporous cellulose beads (MCBs) in a single step procedure using CA as a starting material. DMSO is non-toxic and recyclable solvent [77]. To achieve greener or more sustainable process, DMSO was selected to the solvent for CA. The cellulose beads were directly obtained from DMSO solution of CA by combination of NIPS and alkaline hydrolysis. Additionally, similar MCB was successfully obtained using CA recovered from used CFs and evaluated.

2.2 Experiment

2.2.1 Materials

CA with molecular weight of 50,000 and an acetyl content of 39.2 to 40.2 wt% was purchased from Sigma-Aldrich. DMSO, 0.1 M NaOH, 0.1 M HCl, $CaCl_2$, and ethanol were obtained from Wako Pure Chemical Industries, Ltd. Sodium hypochlorite pentahydrate was purchased from Tokyo Chemical Co., Ltd. Fluff pulp was picked out from adult diaper (brand name: Refre, LiveDo Corporation) and used for comparing with MCBs. All reagents were used without further purification. The CF waste collection was done at Himeji plant of Nippon Shokubai Co., Ltd. The waste in the triple packaging plastic bags was sent to our laboratory and CA was recovered from CF waste at our laboratory.

2.2.2 Measurement

FTIR spectroscopic measurements with attenuated total reflectance were performed with an iS50R FTIR (Thermo Scientific· Nicolet·). Stereo microscopic images were obtained with a stereo microscope model Z6 APOP (Leica). SEM images were recorded with a FE-SEM SU8020 (Hitachi) at 1.5 KV or 2.0 KV. Compression ratio and compression stiffness were measured with a compression-testing machine KES-G5 (Kato Tech Co., Ltd.). For this measurement, a lump of swollen cellulosic beads was used. Specific surface area of the MCB was determined by using the BET instrument described in chapter 1. XRD analysis was performed on the same equipment described in chapter 1 at 2θ range from 5 to 50°.

2.2.3 Fabrication of MCBs

The cellulosic beads were readily obtained by combination of NIPS and the successive alkaline hydrolysis in one-pot (Figure 2-1). A typical fabrication protocol of the microporous cellulose beads (MCBs) is as follows. A DMSO solution of CA (10.2 wt%, 1 mL) was dropped into 30 mL of 0.1 M NaOH solution with gentle stirring to form the beads. The mixture was kept stirring for 18 h to complete deacetylation by alkaline. The obtained porous beads were washed with deionized water until the pH of the solution became neutral. Final washing with ethanol and successive drying afforded cellulosic porous beads (MCB-1). Similarly, acetate porous beads (APB-1, 2, and 3) were prepared except use of deionized water, 0.1 M HCl, and $CaCl_2$ aqueous solution as poor solvent, respectively, instead of 0.1 M sodium hydroxide for preparation of the beads. MCB-2 and 3 were fabricated under conditions similar to MCB-1 except the CA concentration of 7.8 wt% and 5.4 wt%, respectively.

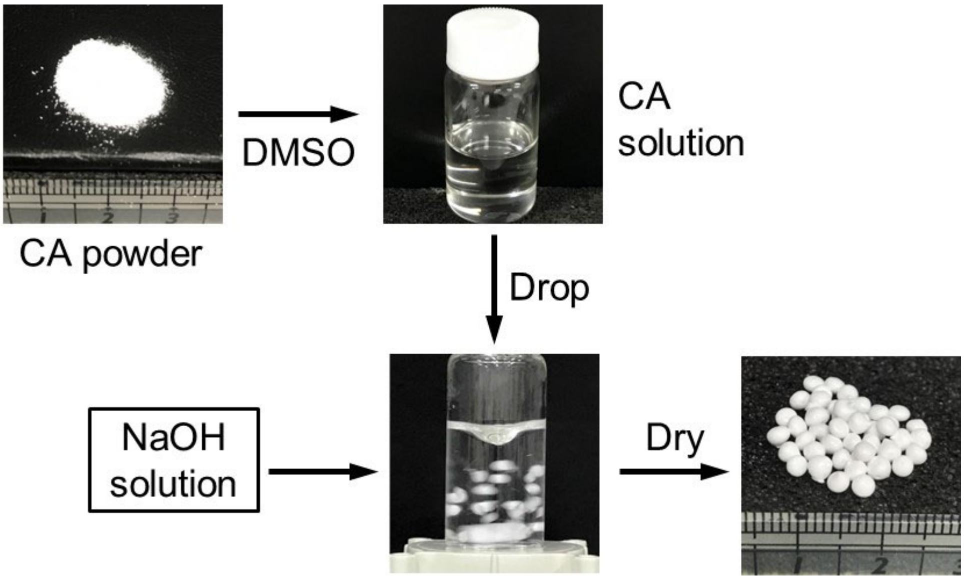

Figure 2-1. Fabrication process of microporous cellulose beads

2.2.4 Measurement of water absorbency of MCB

Two methods were applied for measuring water absorbency of MCB.

1) Absorption capacity of the beads

Beads were immersed in 100 mL of deionized water in 200 mL beaker for 1 min. Then, the wet beads were taken out from the beaker and the excess amount of water was wiped off by Kimwipes (KIMWIPE TM S-200, Nippon Paper Crecia Co., Ltd..) and the weight of the wet beads were measured. Absorbent capacity was calculated according to the following formula;

$$\text{Absorption capacity (g/g)} = (W_1 - W_0)/W_0 \qquad (2\text{-}1)$$

where W_0 and W_1 are the dry and wet weights of MCB respectively.

2) Water absorption capacity (WAC)

As a fluff pulp absorbs water by utilizing capillary effect in a diaper, water absorption capacity (WAC) was measured as a lump and compared. About 1g of sample was immersed in 100 mL of deionized water in a 200 mL of beaker for 1 min. Then, the wet sample was poured onto a sieve having a mesh size of 720 µm, the sieve was leaned for 10 seconds to drain water, and the weight of the wet sample was measured. The measurement was performed 5 times with the same sample, and the average value was calculated following formula;

$$\text{WAC (g/g)} = (W_3 - W_2)/W_2 \qquad (2\text{-}2)$$

where W_2 and W_3 are the dry and wet weights of sample respectively.

2.2.5 Preparation of MCBs from used CFs

As shown in Figure 2-2 (A), the used CFs were ultrasonic cleaning in 0.05 wt% sodium hypochlorite aqueous solution for 30 min, after external paper removal, CFs were ultrasonic cleaning in deionized water for 30 min two times, so to take out CA fiber. Successively, to remove potential organic compounds the filters were ultrasonic cleaning in ethanol for 30 min twice. Finally, the obtained samples of CA were dried at 50 °C for

60 min in the oven and dried recycled CA fibers (Figure 2-2 (B)) were obtained. Macroporous cellulose beads (MCB-4, Figure 2-2 (C)) using recovered CFs were obtained from the recycled CA fibers in the same manner as described in subsection 2.2.3 using the CA fiber instead of the CA powder and setting the concentration of the CA fiber to 5.4 wt%.

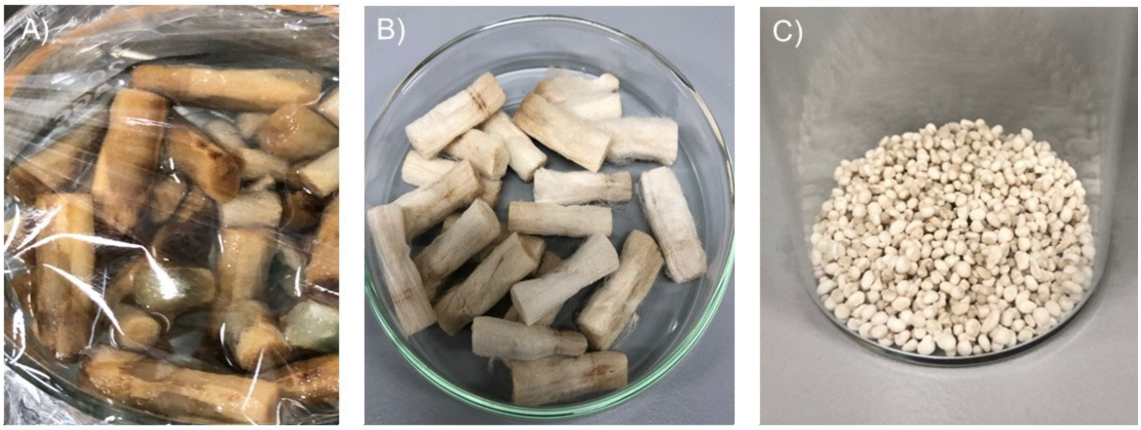

Figure 2-2. Pictures of the steps taken from used CFs (A) to MCBs (C) through recycled CA fibers (B)

2.3 Results and discussion

2.3.1 Characterization of MCBs

Figure 2-3 shows SEM images of MCB-1. MCB-1 had smooth fine pores on the surface (Figure 2-3(a)), and the interior consisted of large pores (Figure 2-3(b)) with a diameter of around 10 μm and macroporous walls having submicron size continuous pores between them (Figure 2-3(c) and (d)). By using an alkaline aqueous solution as a phase separating agent, rapid phase separation on the particle surface would be suppressed, resulting in the smooth surface of the particle. Such macroporous walls with submicron size continuous pores are presumed to be formed by spinodal decomposition mechanism [78].

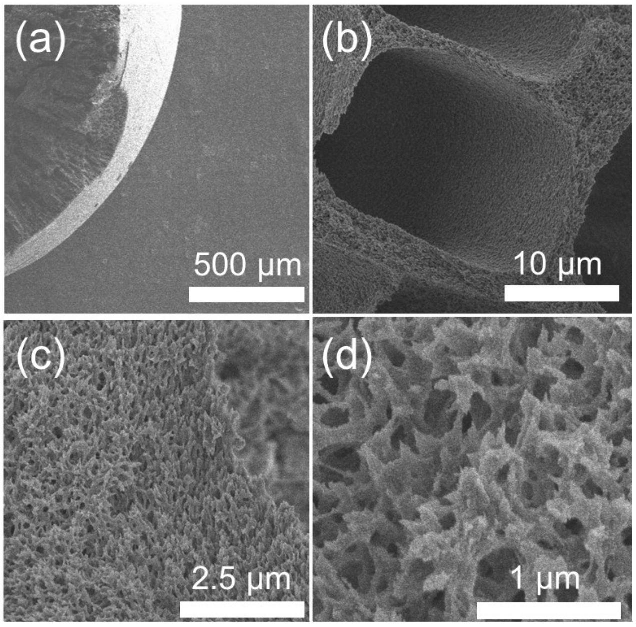

Figure 2-3. SEM images of MCB-1 with different magnification

In the FTIR spectrum of MCB-1 (Figure 2-4(c)), the absorption peak at 1735 cm^{-1} due to the stretching vibration of C=O of the acetyl group completely disappeared and the broad absorption peaks at around 3400 cm^{-1} and 2900 cm^{-1} derived from the hydroxyl group became larger than those of CA. The spectrum of MCB-1 was in good accordance with that of reagent cellulose. These data clearly suggest that the acetyl group of CA was selectively hydrolyzed under the present conditions. Interestingly, the pouring of the CA solution into the aqueous alkaline induced the formation of the macroporous bead of CA and the conversion from CA to cellulose in one-pot to form the MCBs.

This single step preparation of the MCBs is highly useful for industrial applications since no tedious multi-step procedures are involved for the preparation.

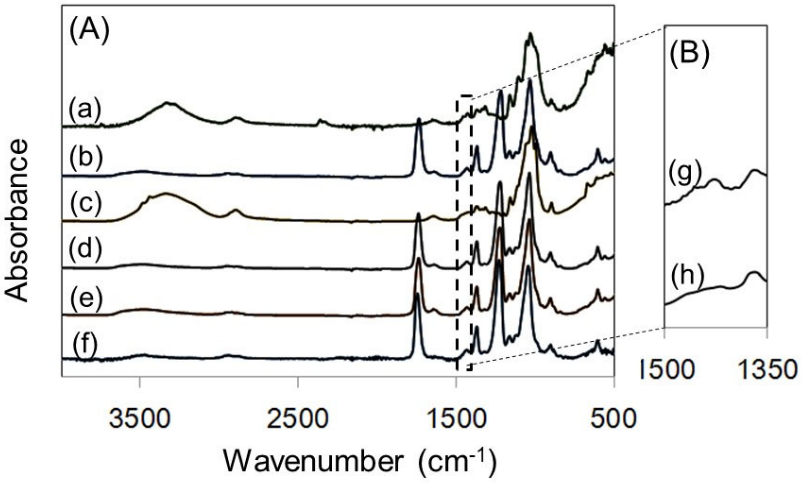

Figure 2-4. FTIR spectra (A) of cellulose (a), CA (b), MCB-1 (c), AMB-1 (d), AMB-2 (e), and AMB-3 (f); expanded spectra (B) of cellulose (g) and MCB-1 (h)

From the BET analysis, MCB-1 possessed relatively large specific surface area of 32.0 m^2/g. This value is smaller than that of the cellulose monolith obtained by TIPS method from CA [66], which may be a disadvantage for applications of the present microporous particles.

The polymer structure, specific surface area, and surface morphology were significantly influenced by type of poor solvent, into which the CA solution was dropped. In this study, deionized water, 0.1 M HCl, and $CaCl_2$ aqueous solution were also used as poor solvent. FTIR analysis showed that no deacetylation occurred for the three samples (AMB-1, 2 and 3, respectively). Although the HCl was reported to be effective for the deacetylation of CA, the present reaction conditions did not induce the deacetylation [79]. These data clearly indicate that use of the NaOH aqueous solution is essential for the single-step preparation of the macroporous cellulose beads.

The specific surface area of AMB-1, 2 and 3 were 17.6, 17.8, and 21.4 m^2/g, respectively. These data were much lower than that of MCB-1. The surface area of the macroporous beads may become larger during the deacetylation. In order to investigate these differences, the macroscopic and microscopic morphologies of MCB-1 and AMB-1 were compared by using stereo microscope and SEM. As shown in the stereomicroscopic images (Figure 2-5(a) and (b)), the cross-section image of MCB-1 was similar to that of AMB-1. The internal structures of both samples observed by SEM were also close to each other (Figure 2-5(c) and (d)).

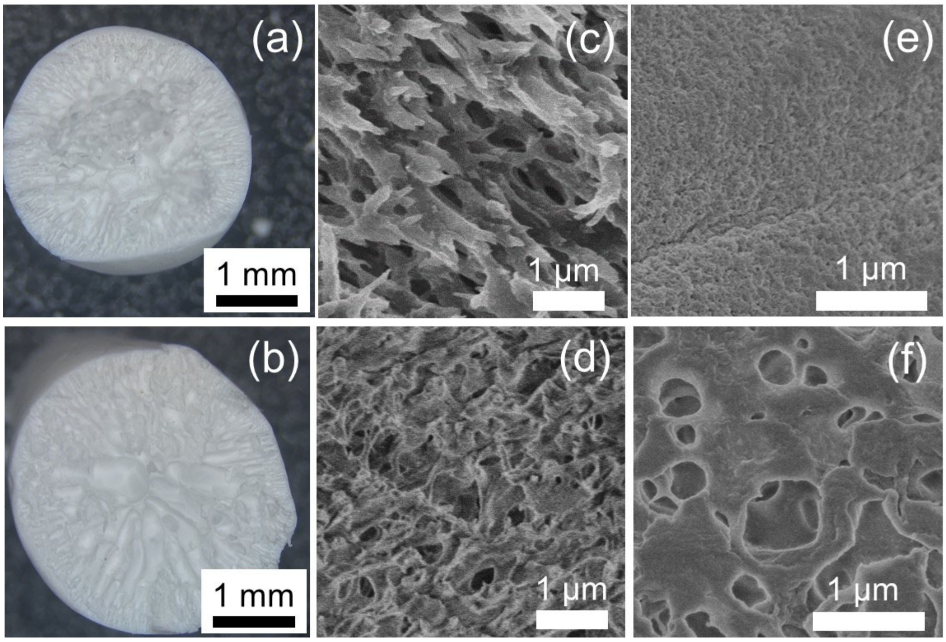

Figure 2-5. Stereo microscope images of MCB-1 (a) and AMB-1 (b); inside SEM-images of MCB-1 (c) and AMB-1 (d); surface SEM-images of MCB-1 (e) and AMB-1 (f)

On the other hand, the morphology of the surface structure was greatly different (Figure 2-5(e) and (f)). Very dense pores on the surface were found for MCB-1, whereas the surface of AMB-1 consisted of a skin layer with large pores. It was reported that the aggregation of the concentrated layer is slow so as to form larger droplets when water is poor solvent [80], which reasonably explains the surface morphology of AMB-1. By the addition to the NaOH solution, the deacetylation occurred while forming monoliths, which might accelerate the aggregation on the surface. As a result, the surface morphology of MCB-1 was significantly different from that of AMB-1. In using pure water as poor solvent, the solvent substitution occurs very fast on the particle surface as compared with that in the alkali aqueous solution, leading to the formation of large pores. In other words, when the CA solution contacts pure water, the coalescence of the diluted phases occurs in priority to the coalescence of the polymer, resulting in the formation of large pores.

Figure 2-6 shows X-ray diffraction (XRD) spectra of cellulose powder (reagent) and the as-obtained MCB-1. In the diffraction pattern of MCB-1, the crystalline peak of cellulose was split into two weaker and broader peaks at 2θ = 20.1 (110) and 21.5 (200). In the magnified FTIR spectrum of MCB-1 (Figure 2-4(B)), a peak at 1430 cm^{-1} due to CH2 bending vibration of crystalline cellulose [81] was not definitely observed.

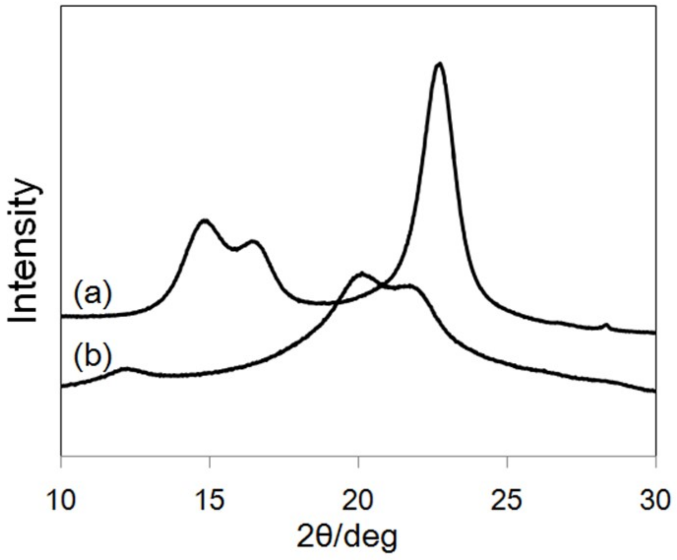

Figure 2-6. XRD traces of cellulose (a) and MCB-1 (b)

These data strongly suggest the formation of amorphous cellulose II structure for the present macroporous cellulose beads.

Table 2-1 summarizes the water absorbency, specific surface area determined by BET (S_{BET}), compression ratio, and compression stiffness of the macroporous cellulose beads prepared with different CA concentrations.

Table 2-1. Water absorbency, specific surface area, compression ratio, and compression stiffness of cellulosic porous beads

Code	CA Conc. (wt%)	Water absorbency (g/g)	S_{BET} (m^2/g)	Compression rate (%)	Compression stiffness
MCB-1	10.8	5.2	32.0	45	0.87
MCB-2	7.8	8.3	25.4	52	0.76
MCB-3	5.4	15.5	25.5	80	0.30

As the concentration decreased, the water absorbency and compression rate greatly increased, whereas the compression stiffness decreased. The increase of the water absorbency and the decrease of the compression stiffness are probably due to the decrease of the solute amount at the time of the solvent exchange and the increase of the porosity at the time of the monolith formation. Little significant change was observed for the surface area even in the change of the CA concentration. When volume of a material is V, density is ρ, and surface area is S, the specific surface area S_S per unit mass is represented as $S_S = S/V\rho$. The size (volume) of the macroporous beads obtained in this study became smaller with decreasing concentration.

On the other hand, it is known that the monolith density decreases with decreasing concentration in the NIPS method, Thus, there was little significant change in the specific surface area even as the volume decreased with decrease of the density. Figure 2-7 shows photos of a wet sample of MCB-2 during and after the compression test, which clearly shows the good flexibility under the wet conditions. Interestingly, the compressed sample instantaneously reabsorbed water after the release of pressure. The deacetylation may increase the affinity toward water on the basis of interaction between hydroxyl groups of cellulose and water molecules.

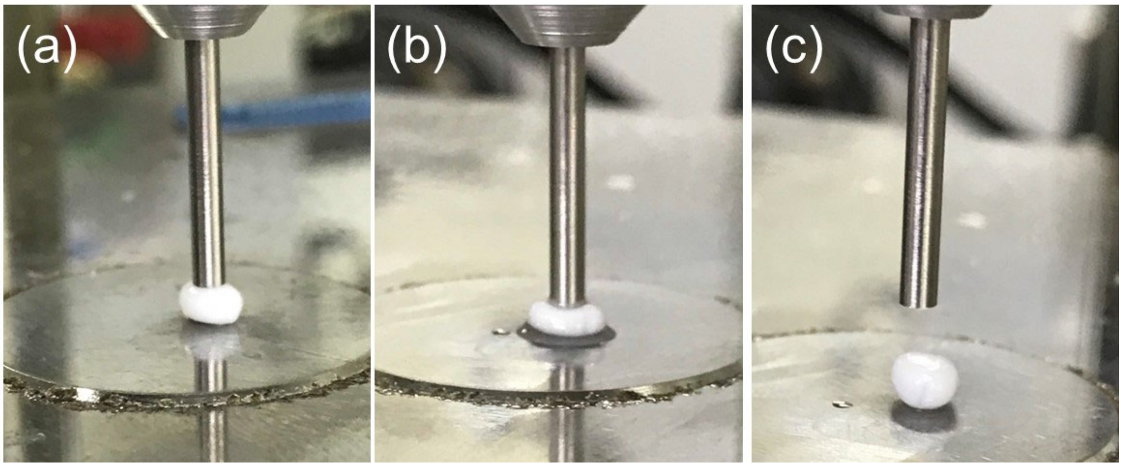

Figure 2-7. Mechanical properties of wet cellulose porous beads (MCB-2) before (a), during (b, water desorption), and after compression (c, water resorption)

2.3.2 Water absorption capacity (WAC) of MCB compared with pulp used for disposable diapers

In order to investigate potential applications for MCBs, WAC value of MCB was measured and compared with that of fluff pulp. Table 2-2 summarizes the results.

Table 2-2. WAC values of fluff pulp, MCB-3, and MCB-4

Sample	Water absorption capacity (g/g)
Fluff pulp	22.7 ± 0.7
MCB-3	22.8 ± 0.4
MCB-4 (obtained from used CFs)	23.0 ± 0.7

Interestingly, the cellulose beads obtained from CA, including those recovered from CF, showed good WAC value comparable to that of pulp used in commercially available disposable diapers, and there is a possibility that these macroporous beads can be used in disposable diapers. Figure 2-8 shows the photographs before (upper photo) and after (lower photo) water absorption of those samples.

Regarding Japanese disposable diapers including those for adults, the Ministry of Land, Infrastructure, Transport and Tourism (MLIT) has started a study in 2018 on whether to flush used disposable diapers into the sewer and throw them away. Initially, it seemed that crushing and breaking of disposable diapers was also considered, but crushing and breaking have been determined to be not applied. In the data of "Information arrangements on recycling of used disposable diapers" by the Ministry of the Environment, fluff pulp occupies 52 wt% of disposable diapers [82] and it may be clogged in a U-shaped pipe of the toilet unless crushed. Therefore, new shaped pulp such as MCBs flowing in water with comparable absorption performance may be a useful alternative to fluff pulp in probable flushable-in-toilet diapers.

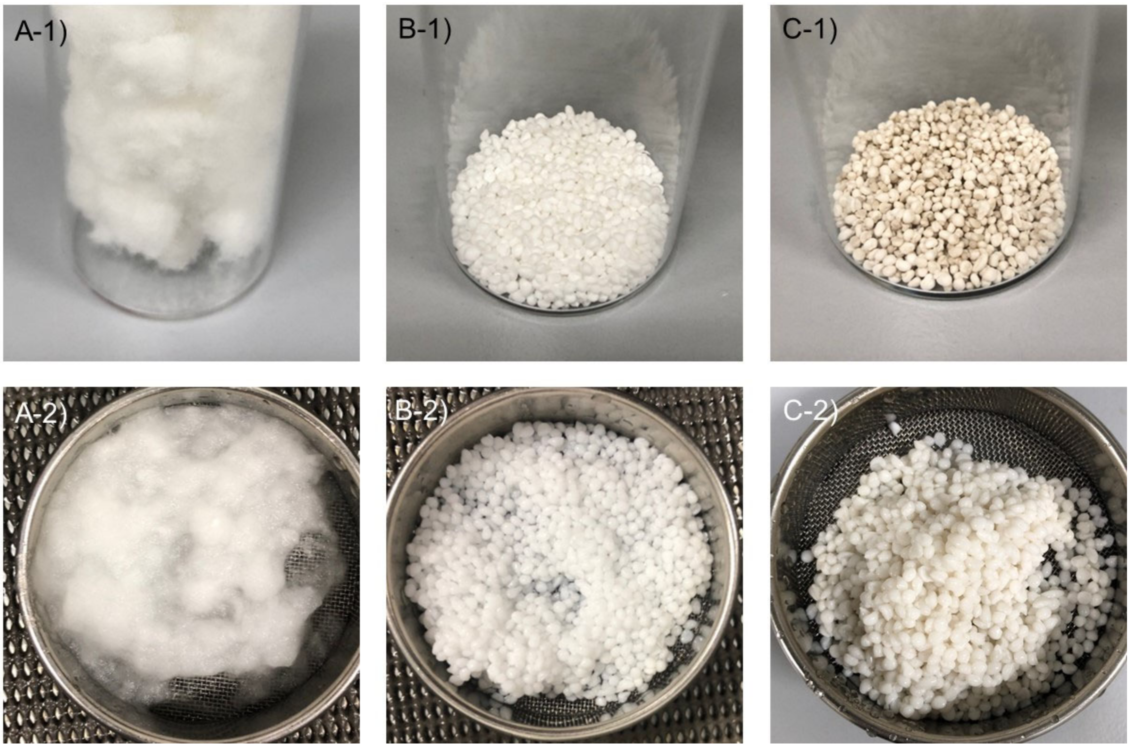

Figure 2-8. Absorption images of fluff pulp (A), MCB-3 (B), and MCB-4 (C)

2.4 Conclusion

In chapter 2, MCBs having a three dimensionally interconnected porous structure have been successfully manufactured from CA via NIPS in a single step. The macroporous bead formation and deacetylation took place in one pot by pouring the DMSO solution of CA into the aqueous NaOH, which is as simple green process for functional porous cellulose beads. The water absorbency of the present macroporous beads could be controlled by changing the CA concentration. In this study, NIPS was used for preparation of microporous beads. Compared with TIPS, NIPS can provide monoliths from a wide range of polymer concentrations. Therefore, using aqueous alkali as poor solvent for NIPS with the CA solution would provide various shapes of macroporous cellulose materials such as films, sheets, fibers, and blocks, which expand applications of macroporous cellulose materials including cellulose monoliths in wide scientific and industrial fields. For example, quick water absorption is applicable for sanitary applications such as paper diapers. Furthermore, the same functional cellulose beads were obtained from used CFs and valorization of harmful waste materials was demonstrated.

Chapter 3

A simple fabrication method and environmental applications of activated-carbon-containing porous cellulose beads

3.1 Introduction

Dyes are used in various industries as colorants for paper, pulps, textiles, food, and cosmetic rubbers. Most dyes are highly stable and difficult to remove from industrial waste [83, 84]. The presence of dyes in wastewater has adverse effects on aquatic biota [85]. Therefore, the removal of toxic dyes from industrial wastewater before discharge to the environment is an important issue. Various methods have been proposed for wastewater treatment. Among these, adsorption is considered the simplest and most effective method [85, 86].

One type of environmental pollution is contamination with malodorous gases, which has adverse effects on not only ecological environments but also human health and is thus an important problem to solve. Toxic malodorous gases are generated in various places such as animal fattening farms [87], wastewater treatment facilities, and daily living environments (toilets, kitchens, etc.). Sulfur and nitrogen compounds are common malodorous gases. The sulfur-containing compound methyl mercaptan is produced in aerobic or anaerobic environments like petroleum-refining processes, wood pulping production, sewage treatment, and energy-related activities [88]. Large amounts of ammonia are generated from sewage treatment and abattoir sites. The olfactory detection thresholds of methyl mercaptan and ammonia are very low and these chemicals have been designated as offensive odor substances under the "Offensive Odor Control Law" in Japan. Therefore, materials capable of efficiently adsorbing both methyl mercaptan and ammonia are highly desirable. A reusable and eco-friendly adsorbent for wastewater treatment and removal of malodorous gases is thus an important research goal in terms of both environmental remediation and legal compliance.

Activated carbon (AC) has been widely used as a bifunctional adsorbent material for not only water purification but also odor removal because of its large surface area and highly microporous structure [89-92]. However, AC is generally a powder, which makes it difficult to separate and recover [93-95] from aqueous solutions [96]. To solve this shortcoming, environmentally friendly adsorbents containing AC with appropriate size and mechanical strength have been developed by several researchers. For example, granules consisting of AC retained in alginic acid particles [92], films prepared from a solution of cellulose or cellulose acetate (CA) containing AC [93, 95], coagulated beads by adding AC to a cellulose solution [94], and AC-containing monoliths [67, 96, 97] have been reported. Generally, porous materials are mechanically weaker than bulk materials; however, it is possible to improve the mechanical properties of porous materials and even to exceed the properties of bulk materials by considering both the solid-state structure and porous space morphology [98]. For example, spherical particle shapes can mitigate mechanical problems to some extent, as is commonly seen for ionic resin beads. Fabrication of adsorbent beads allows the adsorbent to be readily applied in simple filtration operations. As described in chapter 2, we prepared porous cellulose beads with a three-dimensionally interconnected porous structure by a non-solvent-induced phase separation (NIPS) of CA solution in a single step at room temperature [99].

The purpose of this chapter is to produce AC-containing porous cellulose beads (ACPBs) with excellent mechanical strength using the NIPS method and then evaluate their practical application in water treatment and as a deodorant. ACPBs can be conveniently separated from aqueous solution and easily recovered after the use. The phenothiazine dye toluidine blue (TB) was selected as a model adsorbate in this study because of its widespread use in the textile industry, biotechnology, and medicine. The presence of this dye in water is damaging to aquatic life and human health because it has mutagenic effects and toxic interactions with DNA and RNA [100]. Here, we assess the impact strength and effectiveness of ACPBs in removing TB from aqueous solutions with a wide range of dye concentrations. The adsorption behavior of ACPBs toward TB in water is compared with that of reference beads without AC and the potential for removal of malodorous gases in gas mixtures is also confirmed. In addition, the possibility of white activated carbon is also investigated.

3.2 Experiment

3.2.1 Materials

AC (product name: Taiko CW350SZ) was kindly offered by Futamura Kagaku (Nagoya, Japan). The specific surface area and total pore volume of AC were 1500 m^2 /g and 0.54 mL/g, respectively. TB was purchased from Fujifilm Wako Pure Chemical Corporation (Osaka, Japan). CA, DMSO, ethanol, methanol, 0.1 M HCl, and 0.1 M NaOH were the same ones used in the previous chapter. All chemicals were of analytical grade and used without further purification. Ammonia (100 ppm in nitrogen) and methyl mercaptan (80 ppm in nitrogen) were purchased from Iwatani Fine Chemicals (Osaka, Japan).

3.2.2 Measurement

FTIR measurements were performed on the same equipment described in the section 2.2.2. Stereomicroscopic images, SEM images, and BET surface area were obtained using the same equipment described in the section 1.2.2. Ultraviolet–Visible (UV–Vis) spectra were obtained by a spectral transmittance meter (UV-1650PC, Shimadzu Corporation, Kyoto, Japan).

3.2.3 Fabrication of ACPBs

As shown in Figure 3-1, ACPBs were prepared according to the method described in the section 2.2.3 with slight modifications. A 10.2 wt% solution of CA in DMSO containing the same amount of AC as that of CA was added dropwise into 0.1 M NaOH solution (30 mL) with gentle stirring to form beads. The mixture was stirred for 18 h at 25 °C to complete the deacetylation of CA by the alkaline solution. The obtained beads were washed with deionized water until the pH of the solution became neutral. Final washing with ethanol and successive drying afforded ACPBs.

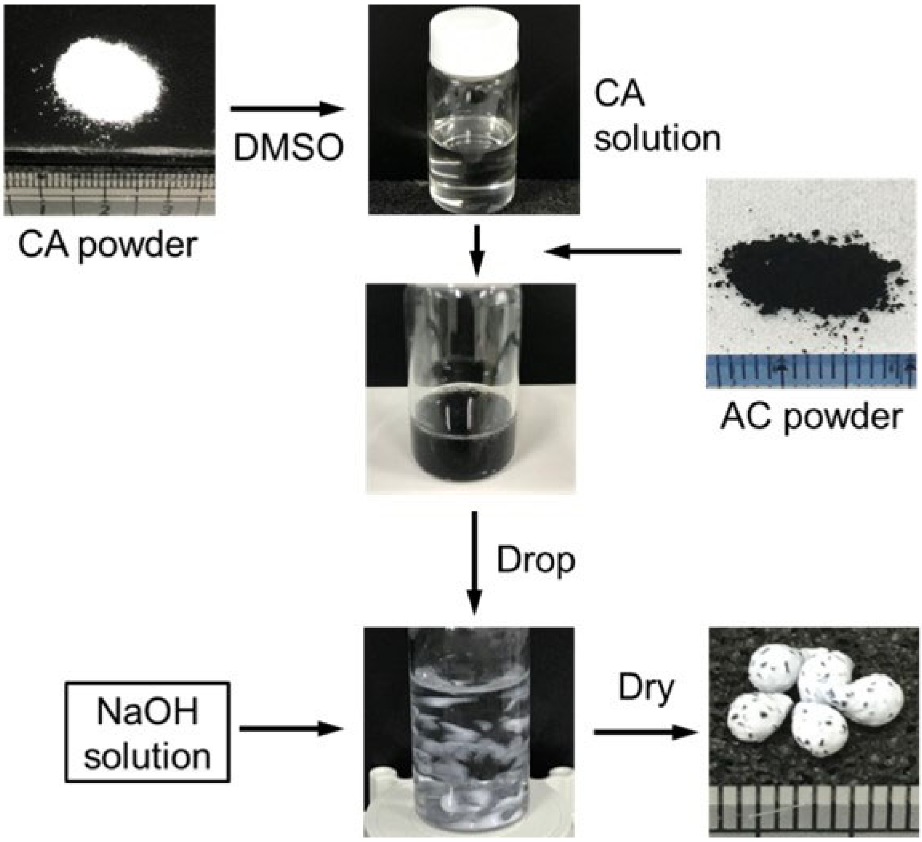

Figure 3-1. Fabrication process of activated carbon (AC)-containing porous cellulose beads. CA, cellulose acetate; DMSO, dimethyl sulfoxide

As reference materials, porous cellulose beads (PCBs) were prepared without AC and porous cellulose acetate beads (PABs) were prepared by adding a DMSO solution of CA dropwise into water in the absence of AC. The impact strength of the beads was tested by quantifying their weight loss after being dropped 30 times from a height of 55 cm onto a steel plate according to a previously reported method [97].

3.2.4 Adsorption of TB

ACPBs (32 mg), PCBs (40 mg), and PABs (40 mg) were added to separate solutions of aqueous TB (40 mL) with different initial concentrations (C_0) of 5.0, 10.1, 12.5, 20.1, 50.7, and 101.0 mg/L in 50-mL plastic containers. The mixtures were gently stirred at 100 rpm and 30 °C under light shielding. The suspensions were stirred during sample collection. At various contact times (t), 100 μL of sample solution was collected using a micropipette and diluted 20 times, filtered through a 0.2-μm filter, and then the concentration of the residual TB at 630 nm was measured using the UV-Vis spectrometer. The adsorption capacity at t was calculated using Equation (3-1) as follows:

$$q_\mathrm{t} = (C_0 - C_\mathrm{t})\frac{V}{m} \tag{3-1}$$

where q_t and C_t represent the adsorption capacity (mg/g) and TB concentration at contact time t, respectively. V and m (g) are the volume of the TB solution and the weight of porous beads, respectively. The effect of C_0 on the adsorption behavior of the beads was studied in the range of 5–101 mg/L. The adsorption capacity of the beads at equilibrium was measured. The equilibrium adsorption capacity q_e (mg/L) was calculated according to Equation (3-2):

$$q_\mathrm{e} = (C_0 - C_\mathrm{e})\frac{V}{m} \tag{3-2}$$

where C_e (mg/L) is the TB concentration at equilibrium.

3.2.5 The recycling and re-usability studies

Ease of separation and the ability to reuse an adsorbent without damage are important standards for practical applications [96]. Adsorption experiments were performed to test the re-usability of the ACPBs by contacting 40 mL of TB solutions (initial concentration of 12.5 mg/L) with 32 mg of ACPBs. ACPBs obtained by stirring for 24 h in a 12.5 mg/L TB solution, were separated by filtration and subjected to desorption experiments. First, 0.5 M HCl in 60% (v/v) methanol solution followed by pure methanol were used as desorption agents. The used ACPBs, which adsorbed TB, were stirred for 2 h in the first desorption agent, separated by filtration, washed with deionized water until neutral, and stirred for 24 h in the second desorption agent, separated by filtration, and dried in vacuo. Re-usability was investigated by repeating the adsorption-desorption process 3 times.

3.2.6 Adsorption of malodorous gases

The adsorption of ammonia gas by ACPBs and PCBs was examined as follows. Ammonia gas (5.0 L) was sealed in an aluminum gas bag (AA-5, GL Sciences Inc., Tokyo, Japan). A 5 cm-long notch, suitable for inserting beads, was made at the end of the gas bag. ACPBs (2.0 g) were inserted into the bag, and then the notch was closed. Keeping the bag at 25 °C, the gas concentration was measured using a gas sensing tube for ammonia (No. 31 La, Gastech Corporation, Kanagawa, Japan) at various adsorption times under atmospheric pressure. A blank experiment was conducted by performing the same operation without the adsorbent. The adsorption behavior of methyl mercaptan was examined in the same manner except that methyl mercaptan gas and a gas sensing tube for methyl mercaptan was used (No. 71, Gastech Corporation, Kanagawa, Japan).

3.3 Results and discussion

3.3.1 Characterization of ACPBs

The FTIR spectra of representative PABs, PCBs, and ACPBs are shown in Figure 3-2. The bands between 2500 and 4000 cm^{-1} were attributed to stretching of hydroxyl (OH) and the asymmetric and symmetric methylene (CH_2) valence vibrations of cellulose. Relative to that of the PABs, PCBs, and ACPBs exhibited weaker absorption intensity at 2927 and 3400 cm^{-1}, indicating the increased content of OH groups of cellulose because of the deacetylation of acetate groups of CA. Also, the bands at 1730 cm^{-1}, 1365 cm^{-1}, and 1213 cm^{-1} in the FTIR spectrum of PABs (assigned to carbonyl groups, ester groups, and methyl groups of CA [101], respectively) completely disappeared in the FTIR spectra of PCBs and ACPBs. Hence, the PCBs and ACPBs were 100 % deacetylated and hydrolysis of the acetyl groups was successfully achieved by the single-step reaction. The weight ratio between AC and CA in the final beads was calculated from the ratio of the precursors at the preparation stage and the degree of deacetylation was 0.62:0.38. The coverage of AC on the surface of the beads was determined with image analysis software

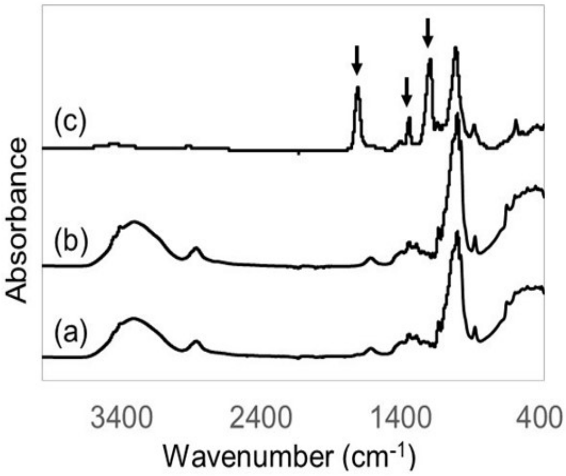

Figure 3-2. Fourier-transform infrared spectra of (a) activated carbon-containing porous cellulose beads, (b) porous cellulose beads, and (c) porous cellulose acetate beads

WinROOF (Mitani Corp., Fukui, Japan). The average and standard deviation of AC coverage on the surface of the beads were 12.4% and 1.7%, respectively.

The macroscopic and microscopic morphologies of PABs, PCBs, and ACPBs were compared by SEM imaging. As shown in the cross-sectional images in Figure 3-3, the internal structures of the three samples were similar. As illustrated in Figure 3(c) and (f), AC was dispersed and fixed in the cellulose skeleton of ACPBs.

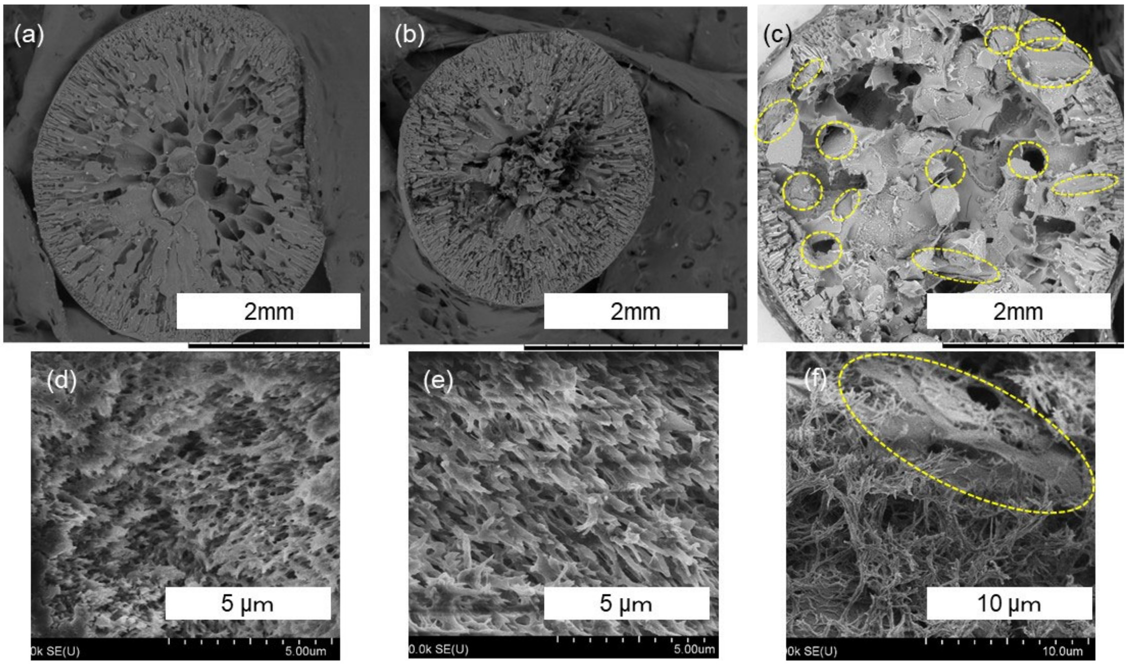

Figure 3-3. Cross-sectional scanning electron microscopy images of (a, d) porous cellulose acetate beads, (b, e) porous cellulose beads, and (c, f) activated carbon-containing porous cellulose beads. Yellow circles in (c) and (f) indicate activated carbon particles

The AC particles with an average diameter of 400 μm were arranged inside the micrometer-sized pores of the cellulose skeleton. These AC particles were considerably larger than the macroporous structure of cellulose. ACPBs, PCBs, and PABs had BET specific surface areas of 700, 25, and 18 m^2/g, respectively. As shown in subsection 2.2.3, deacetylation by an alkaline treatment slightly increases specific surface area [99], and here the addition of AC markedly increased the specific surface area of the beads. Because of the introduction of AC possessing micropores and mesopores into the macroporous cellulose skeleton of the ACPBs, a hierarchical porous structure results that offers a high BET specific surface area. Regardless of the presence of AC, all the porous beads had high impact strength; no weight loss was observed for any of the samples after the impact strength measurements.

3.3.2 Adsorption of TB on ACPBs

The adsorption of TB by the porous beads prepared in this study was examined. The blue TB solution at an initial TB concentration of 12.5 mg/L became colorless in the presence of ACPBs but it remained blue upon addition of PABs or PCBs, suggesting a high adsorption ability of the ACPBs toward TB (Figure 3-4).

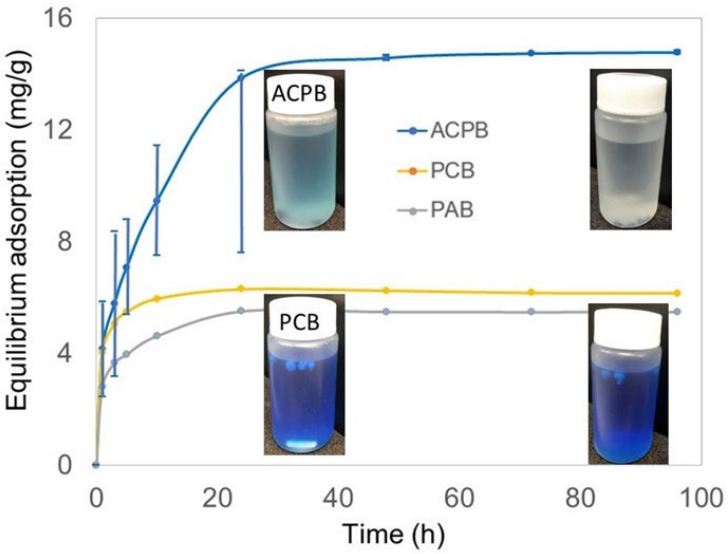

Figure 3-4. Toluidine blue adsorption on different types of beads (activated carbon-containing porous cellulose beads [ACPBs], porous cellulose beads [PCBs], and porous cellulose acetate beads [PABs]) at different contact times (initial toluidine blue concentration C_0 = 12.5 mg/L)

Adsorption occurred rapidly initially and then reached equilibrium in 48 h. After TB adsorption all the beads could be easily removed from the aqueous solution. The bead shape was unchanged although there was slight swelling. The respective amounts of adsorbed TB on the beads after 1 and 3 h were 4.2 and 5.8 mg/g for ACPBs, 4.0 and 5.1 mg/g for PCBs, and 2.8 and 3.7 mg/g for PABs. These data suggest that TB in the aqueous solution first adsorbed on the hydrophilic porous cellulose and then adsorbed on AC through gradual internal diffusion. The difference between the adsorption behavior of PCBs and PABs is assumed to be related not only to the porous structure and large specific surface area, but also the hydrophilicity of the cellulose structure and ion exchange [102]. Overall, our results illustrate that the fabrication method used here provides an easy way to fabricate porous AC-containing cellulose beads with high dye adsorption capacity and impact strength in a single step.

3.3.3 Adsorption kinetics of ACPBs

To investigate the influence of C_0 on the adsorption rate of ACPBs, C_0 was adjusted to be in the range of 5 to 101 mg/L. The effects of C_0 and t on the adsorption of TB onto ACPBs were examined at pH 6 and 30 °C (Figure 3-5). The adsorption amount increased with both C_0 and t. Because of the large number of active sites in ACPBs, rapid adsorption occurred initially (within the first 24 h). Thereafter, the diffusion of TB inside the pores of ACPBs occurred gradually, and adsorption equilibrium was reached. The rate constants of TB adsorption onto ACPBs were evaluated by three different kinetic models.

According to the Weber–Morris model, a diffusion process may be related to different diffusion rate parameters within various pore sizes and pore blockages may occur over time, resulting in decreased adsorption or diffusion.

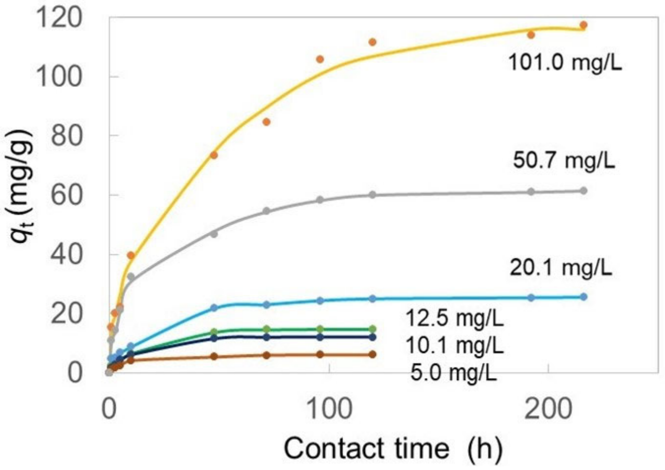

Figure 3-5. Effects of contact time and initial toluidine blue concentration on toluidine blue adsorption onto activated carbon-containing porous cellulose beads

The Weber–Morris model [Equation (3-3)] [103] was applied to the data to confirm the rate-limiting step of this adsorption process,

$$q_{\mathrm{t}} = k_{\mathrm{i}} t^{1/2} + C \tag{3-3}$$

where, k_i and C are the intraparticle diffusion coefficient (mg/g $h^{1/2}$) and the intercept, respectively. In Equation (3-3), if intraparticle diffusion is the rate-limiting step, a plot of q_t vs. $t^{1/2}$ should pass linearly through the origin. However, applying Equation (3-3) to our experimental data gave low correlation coefficients (R^2<0.895) and the intercepts of the plots reflected an obvious boundary layer effect (Figure 3-6). None of the plots passed through the origin, indicating that intraparticle diffusion between the pores was not the only rate-limiting step [103]. This analysis reveals that decreasing the boundary area of the porous cellulose portion by lowering the particle size should effectively increase the adsorption rate of ACPBs.

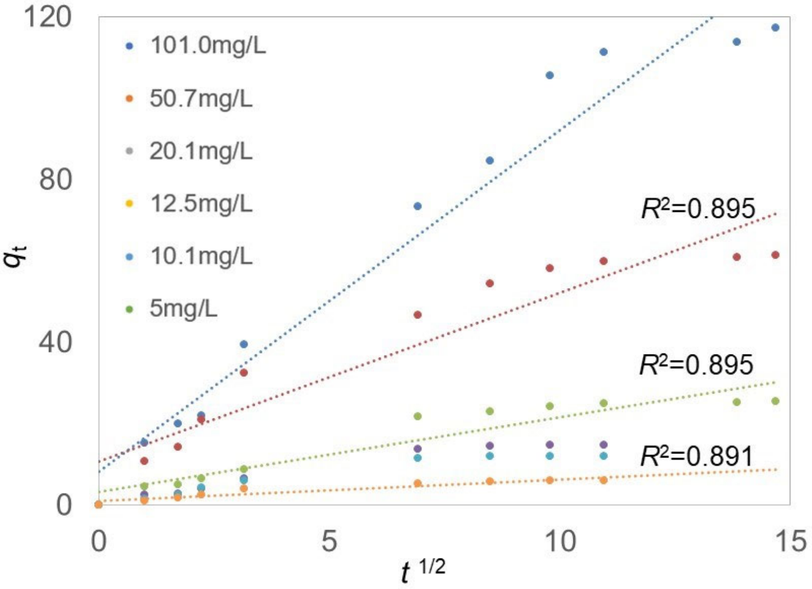

Figure 3-6. Plots for the Weber–Morris model

Next, pseudo-first-order and pseudo-second-order kinetic models [Equation (3-4) and (3-5), respectively] were applied to the experimental data for TB adsorption by ACPBs at different dye concentrations.

$$\ln(q_e - q_t) = \ln(q_e) - k_1 t, \tag{3-4}$$

$$t/q_t = 1/(k_2 q_e^2) + t/q_e, \tag{3-5}$$

where k_1 is the pseudo-first-order rate constant (h^{-1}) and k_2 is the pseudo-second-order rate constant (g/mg h). Equation (3-4) showed proper fitting (R^2<0.969), whereas the correlation coefficients for the pseudo-second-order equation [Equation (3-5)] were relatively high (R^2 > 0.991) in all cases. The kinetic parameters determined for TB adsorption by ACPBs at different C_0 are summarized in Table 3-1.

Table 3-1. Parameters calculated from kinetic data for toluidine blue adsorption onto activated carbon-containing porous cellulose beads at different initial toluidine blue concentrations using to the pseudo-second-order rate equation.

C_o (mg/L)[a]	q_e exp. (mg/g)[b]	q_e cal. (mg/g)[c]	R^2	k_2 (g/mg h)[d]
5.0	6.1	6.3	0.9988	0.0238
10.1	12.1	13.2	0.9979	0.0079
12.5	14.8	16.5	0.9946	0.0050
20.1	25.5	27.1	0.9975	0.0029
50.7	61.5	64.1	0.9982	0.0015
101.0	119.1	128.2	0.9913	0.0003

[a] Initial TB concentration. [b] Experimental equilibrium adsorption capacity. [c] Calculated equilibrium adsorption capacity. [d] Pseudo-second-order rate constant.

Table 3-1 also reveals the high linearity of the plot (R^2 >0.991) and good agreement between the calculated and experimental values of adsorption capacity (denoted as q_e cal. and q_e exp., respectively) determined by Equation (3-5). These results show that the adsorption of TB on ACPBs followed pseudo-second-order kinetics. We found that q_e increased with C_0, and the strong driving force for adsorption induced by the concentration gradient at high dye concentration increased the amount adsorbed by ACPBs. However, a high TB concentration caused k_2 to markedly decrease. Because TB is known to aggregate at concentrations of several tens of micromoles or higher [104], we presume that the migration of TB from the liquid phase to the surface of the adsorbent was slowed by the increased affinity between the dye molecules at high dye concentration such as 10 mg/L, which corresponds to 32 μM.

3.3.4 Analysis of adsorption isotherms

An adsorption isotherm shows how the adsorbed molecules distributed between the liquid and solid phases in equilibrium. To examine this relationship, the Langmuir and Freundlich models were applied to the present adsorption results. According to the Langmuir model, the adsorption energy is constant and independent of surface coverage; maximum adsorption occurs when the adsorbent surface is covered with a monolayer of adsorbate. According to the Freundlich model, adsorption occurs on a heterogeneous surface with a range of different affinities. The linear forms of the Langmuir and Freundlich models are expressed by Equations (3-6) and (3-7), respectively.

$$C_e/q_e = 1/(q_m K_L) + (1/q_m)C_e, \tag{3-6}$$

$$\ln q_e = \ln K_F + \left({}^{1}\!/_{n}\right)\ln C_e, \tag{3-7}$$

where K_L is the Langmuir constant, C_e is the equilibrium TB concentration (mg/L), q_m is the maximum adsorption capacity (mg/g), and K_F and n are Freundlich constants. The term $1/n$ is a measure of adsorption intensity, which indicates the affinity between the adsorbent and adsorbate. If $1/n<1$, the adsorption is favored [105]. When $n > 1$, an attractive force that promotes adsorption is present between the adsorbent surface and adsorbate. When the amount of adsorption and coating on the adsorbent surface are small, $n = 1$. For very weak attractions between the adsorbent and adsorbate, $n \ll 1$. The factor K_F is an indicator of adsorption capacity that also includes the affinity of the adsorbent for the adsorbate.

The results of fitting the Langmuir and Freundlich models to isotherm data are shown (see Figure 3-7) and listed in Table 3-2. The correlation coefficients reveal that both the Freundlich and Langmuir models were appropriately fitted to the isotherm data. The determined value of n, which indicates the adsorption properties, was 2.89, suggesting that adsorption of TB onto ACPBs was favorable. The Langmuir equation predicted that q_m of ACPBs was 123.5 mg/g. This value is comparable with those obtained for TB and methylene blue on other adsorbents such as water-insoluble starch sulfate (26.6 mg/g) [106], pulp fiber (25.0 mg/g) [101], gypsum (26.0 mg/g) [107], nanocellulose fiber aerogel (4.2 mg/g) [108], tea leaf (81.3 mg/g) [109], banana trunk-activated carbon (64.7 mg/g) [90], activated carbon obtained from fruit (271.0 mg/g) [92], bamboo-activated carbon (454.2 mg/g) [110], activated carbon/cellulose films (103.7 mg/g) [95], and cellulose/activated carbon composite monolith (159 mg/g) [96]. Because ACPBs have both a high adsorption capacity and impact strength, they could be used as an efficient and recyclable adsorbent for wastewater treatment.

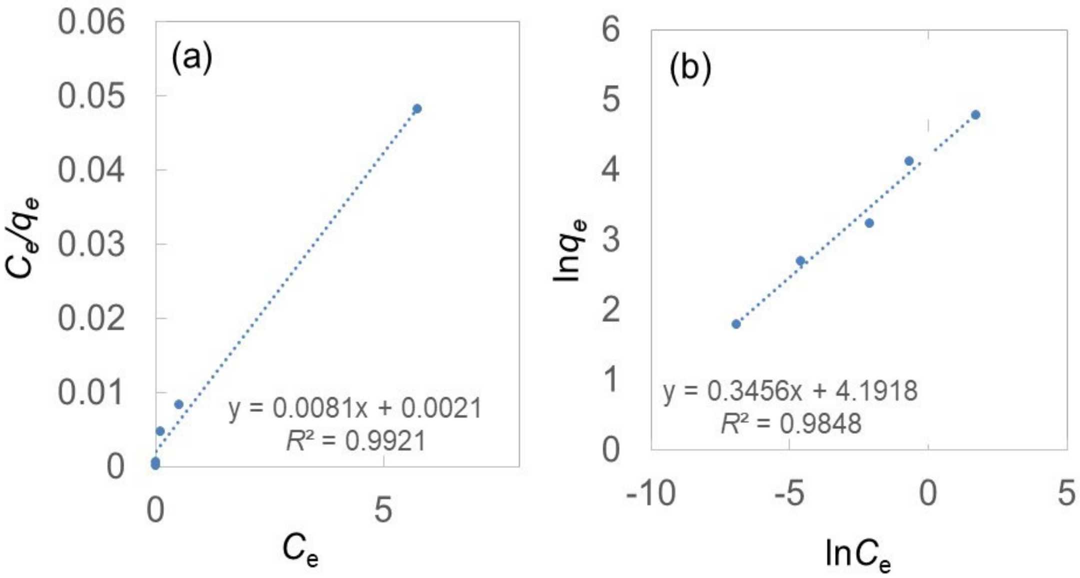

Figure 3-7. Adsorption isotherms of TB onto ACPB, (a) Langmuir, and (b) Freundlich models

Table 3-2. Isotherm parameters for toluidine blue adsorption onto activated carbon-containing porous cellulose beads (pH 6, 30 °C, dosage 32 mg).

Langmuir constants			Freundlich constants		
K_L (L/mg)	q_m (mg/g)[a]	R^2	K_F (mg/g) (L/mg)$^{1/n}$	n	R^2
3.85	123.5	0.992	66.1	2.89	0.985

[a]Maximum adsorption capacity.

3.3.5 Re-usability of ACPBs

The values of the adsorption capacity for each cycle are given in Figure 3-8 as a bar diagram, which shows that the adsorption capacity of the ACPBs was maintained at greater than 85% of the initial adsorption capacity over three cycles. Also, the original shape of ACPBs was retained in appearance.

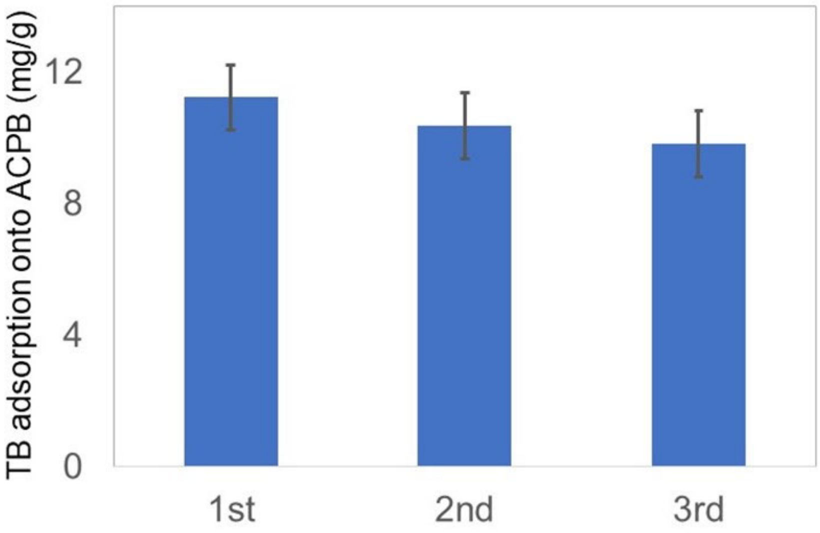

Figure 3-8. Adsorption capacity of ACPBs in three cycles

To confirm more if the original shape of ACPBs was retained, the surface structures of before and after beads recycled were compared by SEM images. In Figure 3-9, the particles slightly protruding from the surface indicate AC. From the images, it seems to have some scratches in Figure 3-9(b), but it maintained a structure that was almost comparable to the original. It can be said that the surface structure of ACPB is hardly destroyed even after three adsorption steps followed by two desorption steps. These data indicate that ACPBs can be recycled without particle destruction and can maintain excellent adsorption capacity after reuse. A more environmentally friendly regeneration method of ACPBs is underway in our laboratory.

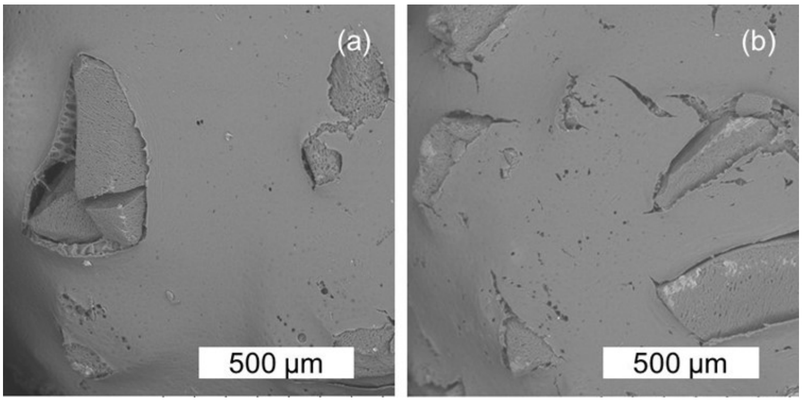

Figure 3-9. SEM images of the surface structure of the bead (a) before and (b) after 3 times use

3.3.6 Adsorption of malodorous gases on ACPBs

Figure 3-10 shows time courses of the ammonia and methyl mercaptan concentration during their adsorption by ACPBs and PCBs. In the blank test, a small decrease of the methyl mercaptan concentration over time was observed, whereas the ammonia concentration decreased slightly, suggesting that ammonia was adsorbed onto the gas bag containing the sample but methyl mercaptan was not. More notably decreases of the concentrations of both ammonia and methyl mercaptan occurred in the presence of ACPBs compared with the case for the PCBs. These data strongly indicate that ACPBs have potential for applications as adsorbent media for malodorous gases such as ammonia and methyl mercaptan. Although cellulose has been reported to adsorb ammonia [111], the combination of a cellulose matrix with fixed AC may provide superior adsorption and easy to handling.

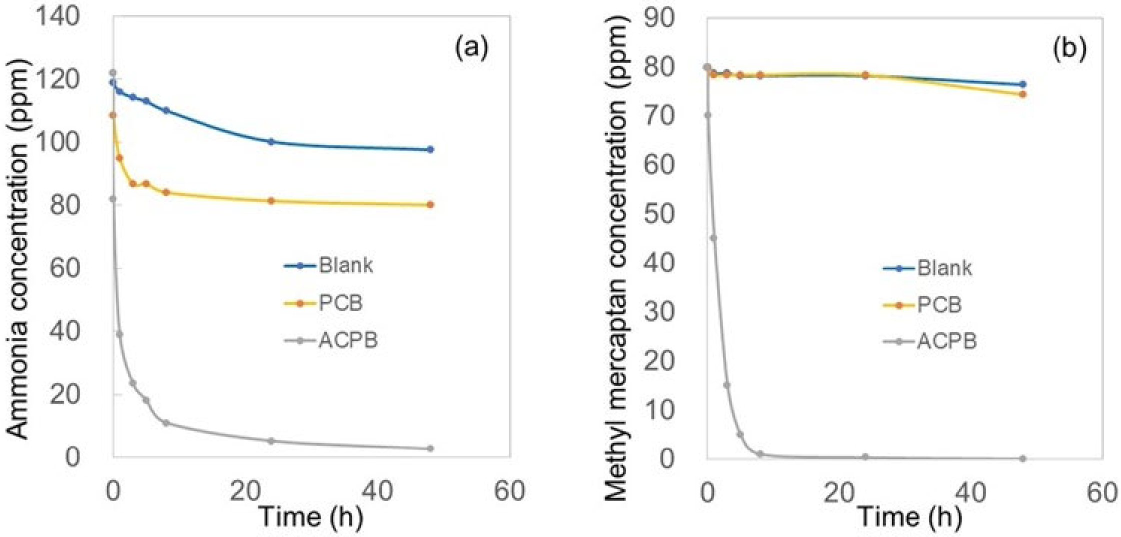

Figure 3-10. Removal of (a) ammonia and (b) methyl mercaptan by activated carbon-containing porous cellulose beads (ACPBs) and porous cellulose beads (PCBs)

3.3.7 Preparation of white ACPB

Here, a preparation possibility of ACPBs with a white appearance was investigated by encapsulating AC inside of the porous cellulose particles. By arranging AC dispersed DMSO solution as inside stream and CA dissolved DMSO solution as outside stream, two streams were simultaneously added dropwise to a 0.1N NaOH aqueous solution using Encapsulator B-390 (Nihon BUCHI K.K.). As shown in Fig. 3-11 (a), frog egg-shaped particles were obtained. After drying the particles, white particles as shown in Figure 3-11 (b) and (c) were obtained. This particle contained activated carbon inside as shown in Fig. 3-11 (d). This was promising result to realize white activated carbon.

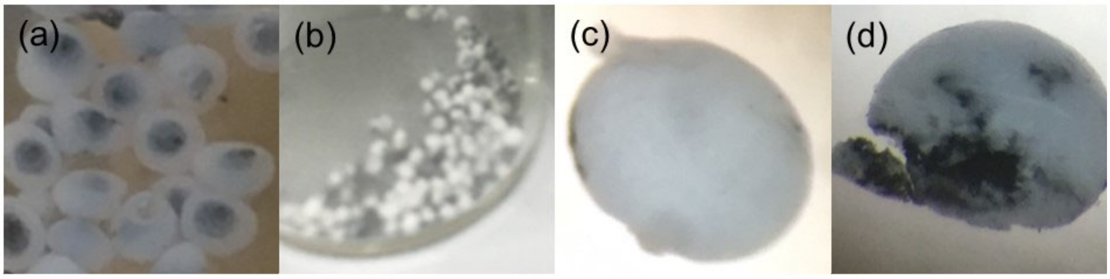

Figure 3-11. White ACPB particle, (a) before drying, (b) dried particles, (c) outside view, (d) inside view

3.4 Conclusion

ACPBs with a three-dimensionally interconnected porous structure were fabricated from CA via NIPS in a single step. ACPB synthesis and deacetylation were conducted in one pot by pouring a dispersion of AC in DMSO solution of CA into an aqueous solution of NaOH. This process is simple, eco-friendly, and clean compared with conventional adsorbent fabrication processes. Characterization revealed that the prepared ACPBs consisted of AC combined with a porous cellulose matrix and they possessed high impact strength. The adsorption data for TB on ACPBs fitted the Langmuir equation well and the Freundlich model revealed that the adsorption of TB onto ACPBs was favorable. The Morris–Weber equation illustrated that the rate-limiting step of TB adsorption was affected not only by intra-particle diffusion between the pores but also the boundary layer effect. The adsorption kinetics of TB onto ACPBs followed a pseudo-second-order equation. ACPB adsorbed 119.1 mg/g of TB at an initial TB concentration of 101.0 mg/L and the Langmuir equation predicted that the maximum adsorption capacity of ACPBs for TB was 123.5 mg/g. This value is comparable with those of several other adsorbents, which makes ACPBs an interesting material for water treatment. Furthermore, ACPBs were stable in reuse and kept an excellent adsorption capacity over 3 times adsorption-desorption recycles. To reduce a toxic waste load for the environment, further investigation of the environmentally friendly method of regenerating the ACPBs is underway in our laboratory. ACPBs also effectively deodorized a gas mixture containing the malodorous substances ammonia and methyl mercaptan. By encapsulating AC inside of the porous cellulose particles, white ACPBs were obtained and they have a potential to use as white deodorants suitable for disposable diapers.

Chapter 4

Preparation and characterization of water-swellable hydrogel-forming porous cellulose beads

4.1 Introduction

Porous hydrogels are known for their excellent water storage and release properties, tissue-like properties, solute transportation capabilities, and rapid stimuli response arising from their microporous structures [112]. Porous hydrogels can also provide hydrated space through which the cells proliferate and assemble into supracellular tissue architectures [113] and supply oxygen which is essential for nutrient uptake from the liquid in the interstitial space to plant roots [114]. In recent years, considerable efforts have been made to develop cellulose-based porous hydrogels including cellulose II nanogels, and a wide range of hydrogels made from nanocelluloses (cellulose I) [115, 116]. These porous hydrogels have high biocompatibility, reduced latent toxicity, and lower environmental impact [117] than hydrogels based on synthetic polymers. The potential areas of applications of cellulose-based porous hydrogels include tissue engineering [117-119], water treatment [120], drug delivery [121-123], and personal care [124]. Among these applications, scaffolding materials for tissue engineering require three-dimensional structure and pores on which cells grow and regenerate the needed tissues [125].

Porous cellulose hydrogels have been prepared by several methods such as freeze-drying [116-118, 121], high internal phase emulsion [119], porogen leaching [120], extraction with supercritical CO_2 [115, 122], and phase separation [123, 124]. Whereas a variety of fabrication techniques of porous cellulose including shape and morphology control have been extensively developed and a shape- and morphology-tunable cellulose monolith has been prepared using a facile temperature-induced phase separation method [66, 126]. However, few studies have been made to introduce ionic groups into a preformed porous cellulose structure to form a porous cellulose hydrogel. In chapter 2, macroporous cellulose beads (MCBs) were prepared through a NIPS method using a cellulose acetate (CA) solution [99]. The macroporous structures of MCBs have been formed by spinodal decomposition mechanism during the formation of MCBs. This material can absorb water in free state but not form a hydrogel and it releases water immediately under pressure like fluff pulp.

This chapter presents a simple and efficient method for preparing hydrogel-forming porous cellulose beads (HFPCBs), by the reaction of urea and sodium dihydrogen phosphate dihydrate (SDP) on prefabricated MCBs. The preparation method allows introduction of functional groups to preformed porous cellulose using safe raw materials while maintaining the original structure. The chemical structure, specific surface area, swelling kinetics, and mechanical strength of the hydrogel beads were measured as a basis for future applications.

4.2 Experiment

4.2.1 Materials

CA, urea, SDP, NaCl, DMSO, ethanol, 0.1 M HCl, and 0.1 M NaOH were the same ones used in the previous chapters. All chemicals were of analytical grade and used without further purification.

4.2.2 Measurement

FTIR spectroscopy was performed on the equipment described in chapter 1. The peak heights were normalized with respect to the peak height at 1030 cm^{-1} corresponding to C−O−C stretching of primary alcohol in cellulose. Stereomicroscopy images and SEM images were captured on the equipment described in chapter 1. Elemental analysis was conducted to determine the nitrogen content of the hydrogel using an elemental analyzer described in chapter 1. The phosphorus content was also determined by the same way described in chapter 1. XRD and BET surface area were performed on the same way described in chapter 1. The differential scanning calorimetry (DSC) measurement was made with DSC 3500 Sirius® Differential Scanning Calorimeter (NETZSCH-Gerätebau GmbH, Germany) under nitrogen gas blanket at a flow rate of 20 mL/min. The temperature was programmed at 25 to 300 ºC with heating rate of 10 ºC/min. For samples swollen in a 0.9 wt.% NaCl aqueous solution, the elastic modulus was determined by RSA-G2 Solids Analyzer (TA Instruments, DE, USA) and the mechanical strength (compressive strength) was determined by the equipment described in chapter 1.

4.2.3 Fabrication of HFPCBs

In a typical synthesis, MCBs were first prepared using a DMSO solution of CA (5.4 wt.%) according to the method described in subsection 2.2.3. Then, 5 g of an aqueous solution of 15 wt.% urea and 4 wt.% SDP was added to 0.5 g of MCBs. The mixture was allowed to stand for 15 min and heated at 145 °C for 20 min. The thermally treated product was washed twice with an ethanol-water mixture (volume ratio, 3:1) and subsequently with ethanol before being dried in vacuo. Different HFPCBs were prepared by varying the feed ratio of SDP against MCBs and the reaction time, as summarized in Table 4-1.

Table 4-1. Sample codes and preparation conditions of HFPCBs

Sample	Feed ratio of SDP (wt.%)[a]	SDP/urea ratio	Reaction time (min)
HFPCB1	30	0.20	20
HFPCB2	40	0.27	20
HFPCB3	40	0.27	30
HFPCB4	70	0.47	20
HFPCB5	70	0.47	24

[a] The feed ratio of urea against MCBs was fixed at 150 wt.%.

4.2.4 Centrifuge retention capacity (CRC)

The CRC of the hydrogel beads in saline solution (CRCs) and in deionized water (CRC_W) were measured by the same manner described in subsection 1.2.4.

4.2.5 Swelling kinetics

A technique based on capillary suction was used to measure the swelling kinetics of the hydrogel beads [127]. A plastic cylinder (inner diameter 2.54 cm) fitted with a stainless steel wire mesh (100 mesh, opening 150 μm) at the base of the cylinder was used as the measurement cell. A glass filter (diameter 12cm, thickness 0.5 cm) was placed in a stainless steel container (20 cm × 20 cm × 2 cm). After pouring 140 ml of deionized water on the top of the glass filter, a piece of filter paper (diameter 12cm) was placed on the glass filter. Then 0.01 g of HFPCBs was weighed and introduced into the measurement cell. The measurements commenced by placing the measurement cell on the filter paper. The time-dependent swelling rate Q_t (g/g) was calculated according to Equation (4-1), as follows:

$$Q_t \text{ (g/g)} = W_t/W_0 \qquad (4\text{-}1)$$

where W_t and W_0 are the amount of liquid absorbed by the HFPCBs at time *t* and the initial weight of HFPCBs, respectively. The amount of liquid absorbed by the HFPCBs at time *t* was determined by the difference between the weight of the cell containing the swollen HFPCBs and that without HFPCBs.

4.3 Results and discussion

4.3.1 Reaction mechanisms and possible condensation of phosphates and carbamate groups

It has been known that flame-retardant cellulose can be obtained by introducing the fire-resistant elements phosphorus and nitrogen by treating cellulose with phosphate and urea [128-130].

As shown in Figure 4-1, the reaction is supposed to be (A) esterification to produce phosphate and (B) formation of carbamate group by reaction with isocyanic acid by urea decomposition.

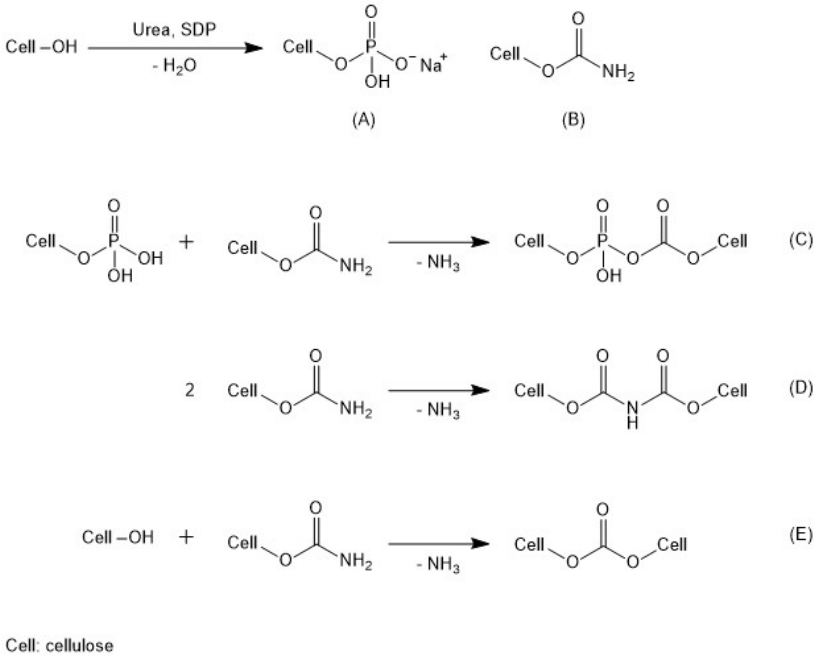

Figure 4-1. Reaction of cellulose with SDP and urea

In addition, high temperatures and long reaction times may lead to formation of cross-linked structures by condensation such as (C), (D), (E) [130-132].

4.3.2 Chemical structure analysis of MCBs and HFPCBs by ATR-FTIR

The FTIR spectra of representative HFPCBs, MCBs, and CA are shown in Figure 4-2. The band at 1736 cm^{-1} in the spectrum of CA attributed to acyl group disappeared in the spectra of MCBs and HFPCBs as a result of deacetylation of CA. The bands between 2500 and 4000 cm^{-1} were attributed to OH stretching and the asymmetric and symmetric CH_2 valence vibrations of cellulose. Relative to the MCBs, the HFPCBs and CA exhibited reduced absorption intensity between 3500 cm^{-1} and 3200 cm^{-1}, suggesting functionalization of the OH groups of cellulose. A similar trend has been reported in the synthesis of cellulose carbamate [133]. It has been reported that phosphorylation at OH groups of cellulose in a phosphoric acid/urea system preferentially occurs at C-6 position regardless of the reaction conditions [131].

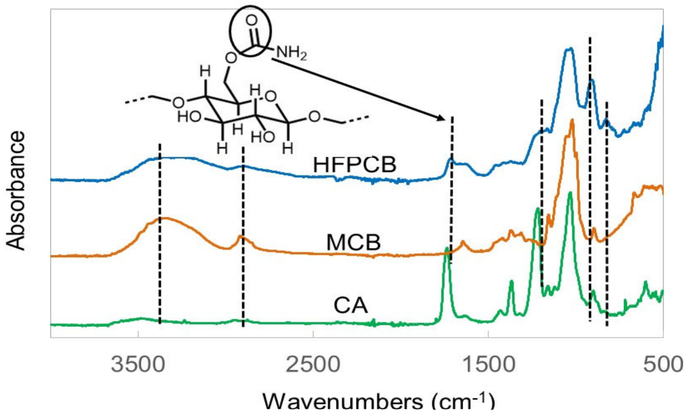

Figure 4-2. ATR-FTIR spectra of CA, MCB, and HFPCB

Thus, the shift of the absorption band originally observed at 3400 cm^{-1} to lower wavenumbers suggests that the introduction of functional groups reduced intramolecular and intermolecular hydrogen bonding at the C-6 position. The band at 1717 cm^{-1} in the spectrum of HFPCBs was attributed to C=O stretching mode of carbamate groups introduced upon reaction between cellulose and urea [133, 134]. The new bands at 1212, 904, and 813 cm^{-1} observed in the spectrum of HFPCBs were assigned to P=O bonds, P−O stretching mode, and P−O−C bonds, respectively [52]. These results indicate that phosphorylated cellulose carbamate was formed on HFPCBs.

4.3.3 Determination of the degree of substitution

The residual reactants and by-products such as ammonium salts, were removed by immersing the crude reaction product in excess 0.01 M NaOH for 1 h. The product was then washed with a mixture of deionized water and methanol and subsequently dried in vacuo. The degree of substitution (DS) values for disodium phosphate monoester (DSp) and carbamate (DSc) groups were estimated according to the method described in subsection 1.3.1. The maximum degree of substitution (DS) of the glucose unit in cellulose is three (C-2, C-3, and C-6) [135]. Table 4-2 shows that the DSp value increased as the amount of SDP was increased. The DSc value decreased with increasing SDP/urea ratio. As previously reported for the starch–urea–phosphoric acid reaction [55], the lower rate of carbamoyl formation and DSc values were due to the increased rate of phosphate ester formation that suppressed the reaction between the OH groups of cellulose and the isocyanic acid generated upon thermal decomposition of urea.

Table 4-2. Contents of P and N and degrees of substitution (DSp and DSc)

Sample	P (%)	N (%)	DSp[a]	DSc[b]
HFPCB1	4.53	1.62	0.31	0.24
HFPCB2	5.51	1.36	0.39	0.21
HFPCB3	5.47	1.46	0.39	0.23
HFPCB4	7.88	0.90	0.63	0.16
HFPCB5	8.39	0.91	0.69	0.17

[a] DSp, degree of substitution for disodium phosphate monoester groups.

[b] DSc, degree of substitution for carbamate groups.

4.3.4 Morphology analysis

The cross-sectional images observed by SEM revealed that MCBs and HFPCBs had a similar three-dimensionally interconnected porous structure with macropores and micropores (Figure 4-3a–d).

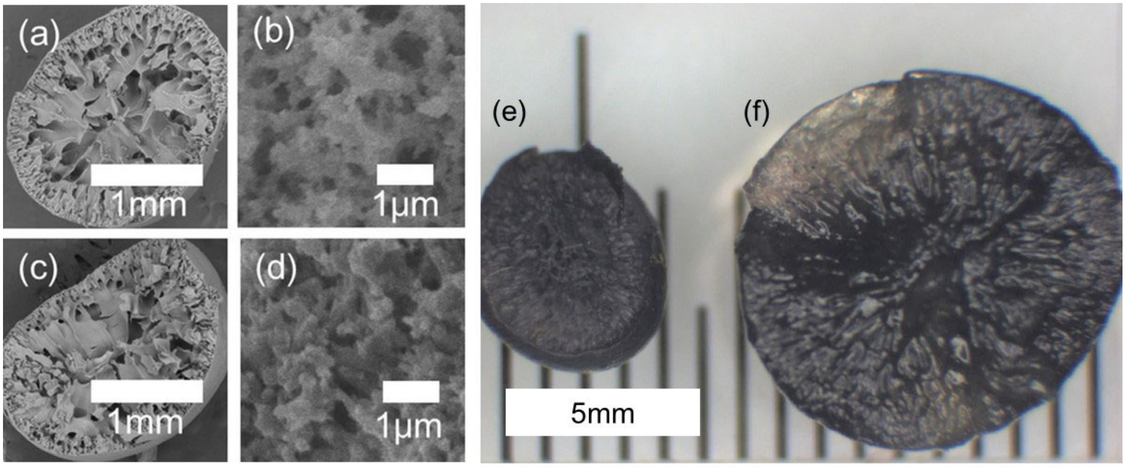

Figure 4-3. (a–d) SEM images and (e, f) stereomicroscopy images of precursor MCBs (a, b, e) and HFPCB3 (c, d, f). The stereomicroscopy images were obtained following sample immersion in an aqueous iodine solution

In addition, MCBs and HFPCBs displayed comparable BET surface areas, for example, 36.5 m^2/g of HFPCB2 and 35.5 m^2/g of corresponding precursor MCBs. These results indicate the negligible effect of the urea/SDP treatment on the microporous structure of the beads.

Upon addition of an aqueous iodine solution, the MCBs expanded in size (Figure 4-3e), while maintaining their porous structure, whereas the HFPCBs not only expanded significantly more than the MCBs but also turned into a hydrogel (Figure 4-3f). The transparent part shows the hydrogel and the dark blue part shows the continuous pores that hold free water. These results indicate the introduction of ionic groups to the nonionic precursor (MCBs) as a result of the thermal reaction between urea and SDP.

4.3.5 XRD analysis

Figure 4-4 shows the XRD spectra of wood pulp cellulose, and representative MCBs and HFPCBs. Both MCBs and HFPCBs exhibited the typical cellulose II pattern [136].

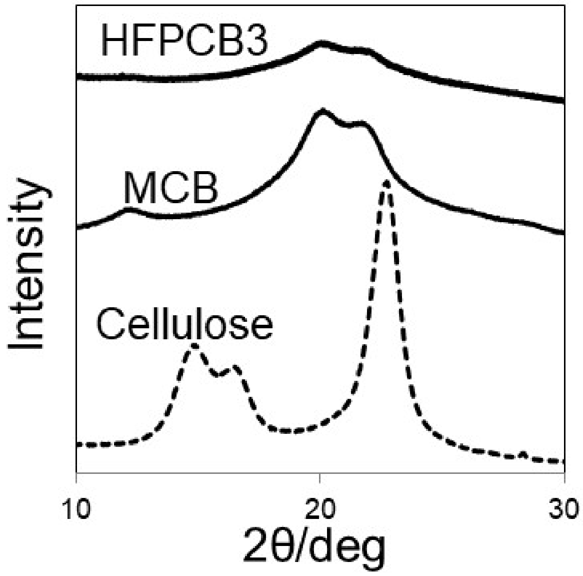

Figure 4-4. XRD patterns of cellulose, MCB, and HFPCB3

Profile fitting was performed between 2θ 10° and 30°, that is, around the main peak of the XRD spectrum, and the crystallinity of the samples was calculated using the ratio between the peak area of the crystal component and the total peak area (i.e., the peak area of the crystal component and the halo pattern area of the amorphous component). Wood pulp, MCBs, and HFPCBs displayed crystallinity values (%) of 66%, 38%, and 20%, respectively. Comparison of these values indicate that a part of the cellulose II structure of the MCBs was converted into a more amorphous structure upon reaction of OH groups with SDP and urea. It has been reported that the crystallinity of cellulose decreases with decreasing intra- and intermolecular hydrogen bonding between hydroxyl groups [137]. We assume the decreased crystallinity of HFPCBs is attributed to the introduction of functional groups.

4.3.6 CRC of HFPCBs

Table 4-3 shows the CRC of the different sample. The ratio of urea to MCBs was fixed at 1.5 for all experiments because the CRC of HFPCBs became lower when the ratio was lower than 1.5. After the reaction, most of the unreacted urea was recovered suggesting urea also acts as a solvent in this reaction. The HFPCB samples generally showed larger CRCs than the precursor sample MCBs. HFPCB2, obtained at a SDP/urea ratio of 0.27 featured the largest CRC value with a corresponding CRC_w value of approximately 50 g/g. CRC_w decreased when the SDP/urea ratio was above or below the optimum ratio.

Table 4-3. CRC_w and CRC of HFPCBs

Sample	Centrifuge retention capacity	
	CRC_w (g/g)	CRC (g/g)
MCB	6.1	6.1
HFPCB1	19.0	8.0
HFPCB2	48.1	12.4
HFPCB3	24.1	8.1
HFPCB4	31.7	9.2
HFPCB5	17.3	7.2

When the SDP/urea ratio decreased, the number of phosphate groups introduced into the structure also decreased, which is not favorable for absorption capacity, fewer ionic groups imply a smaller osmotic pressure. In contrast, when the SDP/urea ratio increased, the HFPCBs became almost water-soluble owing to a decrease in crosslinking density. During the thermal reaction between urea and starch, cross-linking has occurred between two carbamate groups and/or between the hydroxyl and carbamate groups [130-132]. In the case of thermal reaction of starch–urea–phosphoric acid, it was reported that an increase in phosphate prevented carbamate groups from reacting with adjacent carbamate groups or hydroxyl groups, thereby retarding the cross-linking process [42]. A similar mechanism may explain the poor water absorbency of the HFPCBs when the SDP/urea ratio is high. The experimental results and proposed mechanism suggest that high water absorbency is achieved at an optimal composition.

4.3.7 DSC curves of HFPCBs

In order to analyze the change of crosslinking density, the thermal behavior of MCB and HFPCB was investigated using DSC. It has been reported that amorphous cellulose decomposes at around at 190°C [138] and there is a direct correlation between the degree of cross-linking density and the decomposition temperature of the cellulose membranes

[139]. Figure 4-5 shows the DSC curves obtained from MCB, HFPCB2, and HFPCB3. The endothermic peaks at around 100 °C are considered to be caused by water loss of the materials. The sharp endothermic peaks between 190 °C and 220 °C can be attributed to the pyrolysis of the products. The observed decomposition temperatures of MCB, HFPCB2, and HFPCB3 were 187.4 °C, 190.6 °C, and 216.5 °C, respectively. DSC of cellulose treated with diammonium hydrogen phosphate has been reported to show endotherms ascribed to random chain scission and pyrolysis at lower temperature than untreated cellulose [140], and thermal stability of cellulose and cellulose derivatives is influenced by their crystallinity [141]. HFPCB2 showed pyrolysis at slightly higher temperature than MCB. The result could be explained by competition between decrease in the decomposition temperature due to decrease in crystallinity and increase in the decomposition temperature due to increase in crosslinking density. HFPCB3 which was prepared with a longer reaction time, showed higher decomposition temperature than MCB and HFPCB2, probably because of relatively higher cross-linking density.

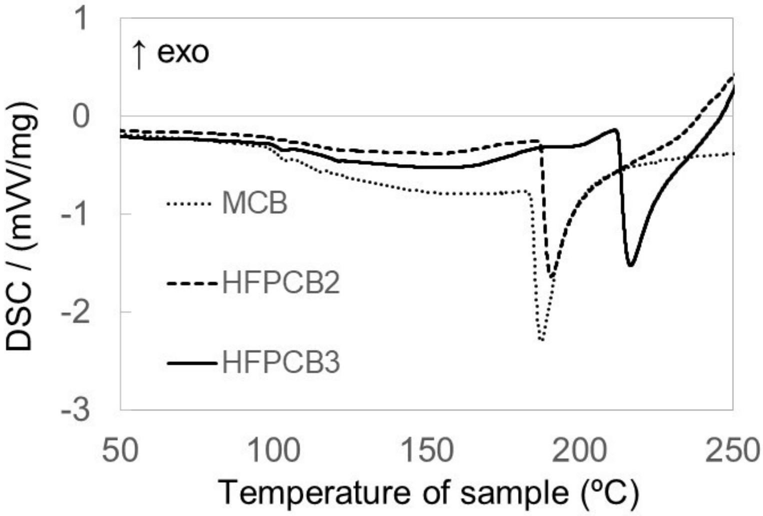

Figure 4-5. DSC curves of MCB, HFPCB2, and HFPCB3

4.3.8 Effect of reaction time on CRC_w

HFPCB2 and HFPCB3 displayed a similar DSp value. However, a small difference in DSc and a significant difference in water absorbency between these two samples were observed. As previously discussed, carbamate groups are formed as the cross-linking reaction proceeds. Thus, the relationship between reaction time and water absorbency was examined at a fixed weight ratio of reagents (MCB:urea:SDP = 1.0:1.5:0.6) at 145 °C, and the results are shown in Figure 4-6.

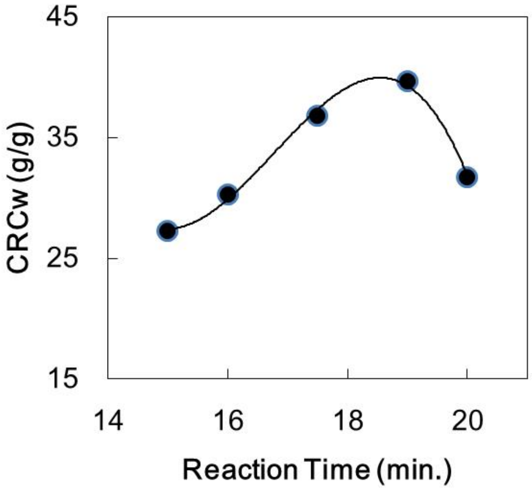

Figure 4-6. Relationship between reaction time and water absorbency (CRCw)

CRC_w increased with increasing reaction time, reaching a maximum of 39.7 at a reaction time of 19min, before decreasing with prolonged reaction time. The trend suggests that the substitution of OH groups with phosphate groups and carbamate groups, which contribute to water absorbency, and the cross-linking reaction caused by carbamate groups proceeded simultaneously. When substitution with phosphate groups reached saturation, the effect of cross-linking reaction became predominant. The result indicates that both the composition of the reaction mixture and the reaction time need to be carefully selected to achieve high CRCs.

4.3.9 Swelling kinetics

The swelling kinetics of the HFPCBs was determined by measuring the swelling capacity as a function of time at 25 °C for samples with different equilibrium swelling capacities Q_∞, which were prepared by heating the same composition of reagents (MCB:urea:SDP = 1.0:1.5:0.4) at various reaction times of 22 min, 27 min, and 32 min (Figure 4-7a). The rate of swelling was fast in the initial stages of swelling and gradually decreased to an equilibrium value. From the first-order kinetics model, the rate of swelling at a given time is proportional to the remaining available swelling capacity. Therefore, when the equilibrium swelling capacity is Q_∞, the swelling capacity at time t is Q_t, and the remaining available swelling capacity at t is $Q_\infty - Q_\mathrm{t}$; the first-order kinetics model can be expressed as follows:

$$\frac{\mathrm{d}Q_\mathrm{t}}{\mathrm{d}t} = k_1(Q_\infty - Q_\mathrm{t}) \qquad (4-2)$$

where k_1 is first-order rate constant. Integration of Equation (4-2) between limits of $Q_t = 0$, $t = 0$ and $Q_\mathrm{t} = Q_\mathrm{t}$, $t = t$ gives the following equation:

$$\ln\frac{Q_\infty}{Q_\infty - Q_\mathrm{t}} = k_1 t \qquad (4-3)$$

The second-order kinetics model is expressed as follows:

$$\frac{\mathrm{d}Q_\mathrm{t}}{\mathrm{d}t} = k_2(Q_\infty - Q_\mathrm{t})^2 \qquad (4-4)$$

where k_2 is the second-order rate constant. Integration of Equation (4-4) between limits of $Q_\mathrm{t} = 0$, $t = 0$ and $Q_\mathrm{t} = Q_\mathrm{t}$, $t = t$ leads to the following equation:

$$\frac{t}{Q_t} = \frac{1}{Q_\infty^2 k_2} + \frac{t}{Q_\infty} \quad (4-5)$$

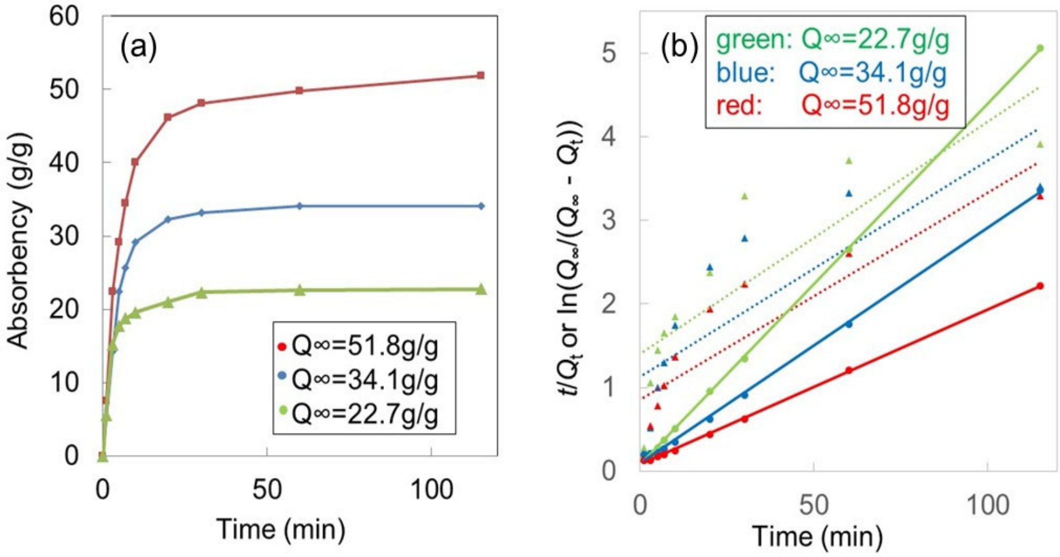

Figure 4-7. (a) Swelling kinetics of HFPCBs and (b) plots of t/Q_t (circles, solid lines) or $\ln(Q_\infty/(Q_\infty - Q_t))$ (triangles, dotted lines) against time

The data in Figure 4-7a were fitted to Equations (4-3) and (4-5) to obtain the fitted data shown in Figure 4-7b. The data did not fit the first-order kinetics model (dotted lines) regardless of the equilibrium swelling capacities. In contrast, the experimental data were well fitted by the second-order kinetics model (solid lines). Swelling kinetics that are determined by the rate of diffusion of the solvent in the network are known to follow the first-order kinetics model [142]. For the second-order kinetics, the rate of swelling is governed by the relaxation process of the polymer chains [143]. Specifically, the rate of swelling or the relaxation process is proportional not only to the swelling capacity that is available at time *t* but also to the internal boundary area enclosing the sites capable of swelling that have not yet swollen at that time. As the internal boundary area is proportional to the swelling capacity that is available at time *t*, the rate of swelling follows a second-order kinetics model. The influence of the internal boundary area is expected to become more significant for materials with high surface areas such as HFPCBs having maintained porous structure. A similar result was reported for hydrogels with porous and mesh-like morphologies [144].

As observed from Table 4-4, k_2 increased as Q_∞ decreased. A similar trend was reported in other hydrogels such as those comprising acrylamides and itaconic acid [144, 145]. The elastic modulus was higher for the sample with low Q_∞ and high k_2. The result indicates that the reduction of Q_∞ was caused by increased cross-linking density in SPC because elastic modulus is known to increase with cross-linking density [146]. The increase of k_2 is likely due to the faster relaxation of the shorter elastic chains between the cross-links at low Q_∞.

Table 4-4. Second-order swelling kinetics-fitted parameters and elastic modulus

Q_∞ exp. (g/g)	R^2	Q_∞ calc. (g/g)	k_2 [g/(g/min)]	Modulus (MPa)
22.7	0.9997	23.2	0.0233	2.73
34.1	0.9987	35.3	0.0089	-
51.8	0.9994	53.8	0.0044	0.14

4.3.10 Mechanical strength

The relationship between CRC and the compressive strength of the HFPCBs was examined by plotting the CRC against the natural logarithm of the compressive strength obtained at 70 % strain of each HFPCB (Figure 4-8a). The compressive strength of the HFPCBs was tens of kilopascal, which is acceptable for applications such as soft tissue repair.

Figure 4-8b–e shows photographs of HFPCB3 subjected to a compression test. The pictures strongly suggest the flexibility and stability of the swollen hydrogel bead under pressure. Furthermore, the sample retained water during the course of compression, and only a small amount of water was released as the load was pressed to its furthest distance onto the bead. The water was promptly reabsorbed as the load was lifted.

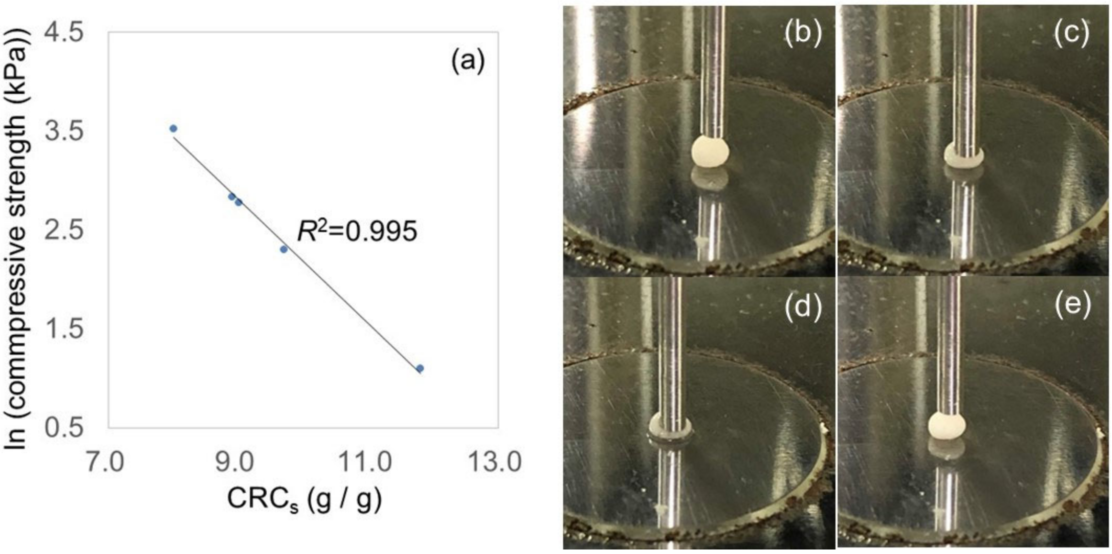

Figure 4-8. (a) Relationship between CRC and natural logarithm of compressive strength. (b–e) Photographs of a hydrogel bead during compression test

4.3.11 Germination of plant seeds

As a potential application of the HFPCBs, a germination test with plant seeds was performed. The HFPCBs were soaked in water for 30 min, and the excess water was removed before seeding with radish seeds. Figure 4-9 shows that germination and growth occurred on the hydrogel beads of HFPCBs within 1 week. For comparison, a similar experiment was performed using MCBs with the same amount of water; however, germination did not occur (data not shown).

Figure 4-9. Germination of Japanese radish on HFPCBs

Seed germination is known to occur in three phases: absorption phase (phase 1), activation phase (phase 2), and germination phase (phase 3) [147]. In phase 1 and phase 3, moisture supply is important [148]. While urea and phosphate are well-known fertilizers [148], neither of them affected germination in this experiment because the beads were washed by water and alcohol before use. Despite the fact that the amounts of water contained in MCBs and HFPCBs was the same, the difference in germination was observed. This result may be attributed to the reduced ability of MCB to retain water (compared with HFPCB) and the subsequent rapid loss of water through evaporation, thereby limiting water supply required for the seeds to germinate and grow. In addition to the water content, phosphate and carbamate in HFPCBs might have affected germination through the osmo-priming effect [147].

4.4 Conclusion

Highly water-swellable HFPCBs were prepared through a single-step thermal reaction of urea and SDP on MCBs by applying the method described in Chapter 1 to the microporous cellulose beads in Chapter 2. HFPCBs retained the interconnected porous structure of MCBs and featured a high specific area of 36.5 m^2/g. FTIR analysis revealed that the HFPCBs had a cellulose phosphate carbamate structure. The HFPCBs achieved a maximum CRC_w of approximately 50 g/g with judicious choice of the reaction time and the composition of the reagents. Despite the high swelling capacity, the compressive strength of the HFPCBs swollen in saline was in the range of several tens of kilopascal. The swelling kinetics of the HFPCBs followed a second-order kinetics model likely because of their high surface area. As a potential application, swollen HFPCBs were successfully used for the germination of plant seeds. The preparation method presented in this study allows introduction of functional groups to preformed porous cellulose to form a porous cellulose hydrogel while maintaining the original structure. The method has a potential to convert preformed porous cellulose materials with various shapes into highly absorbent materials. The HFPCBs are expected to be highly applicable in various fields such as pharmaceuticals, drug delivery, tissue engineering, agriculture, and water remediation.

Chapter 5

Study on the penetration of singlet oxygen into films having an oxygen permeability coefficient close to that of skin

5.1 Introduction

COVID-19 appeared in Wuhan, China in December 2019 was caused by the new coronavirus named as severe acute respiratory syndrome (SARS) coronavirus-2 (SARS-CoV-2), spread all over the world rapidly, and has become one of the biggest issues of the present world. The new coronavirus infection causes SARS and has brought a record number of deaths in the world. It has been reported that the main route for the spread of this disease is human-to-human diffusion mechanism and that the most effective mean to prevent the transmission of COVID-19 is wearing a mask in public coupled with social distance [149]. Besides, infection spreading by contact can occur either by direct contact with an infected person, or indirectly through an infected object or surface. Surfaces and objects can act as a reservoir of microorganism that may spread to whoever contacts with the surface, careful cleaning and disinfection of environmental surfaces are essential for the prevention of bacterial and viral infection [150, 151]. Singlet oxygen ($^1O_2$) is a reactive oxygen species and a strong oxidant. It is therefore highly cytotoxic; it inactivates viruses and kills bacteria [152]. When $^1O_2$ arrives from outside the cell, it reacts directly with the cytoplasmic membrane or generates reactive secondary products—such as peroxy radicals—that may in turn cause lethal damage to the target [153]. In contrast to antibiotics, the mechanism by which species derived from reactions with $^1O_2$ kill bacterial is completely unselective, and offers little room for evolutionary adaptation [154]. To reduce the demands imposed by the continuous disinfection of environmental surfaces, films or structures containing photosensitizers (PSs)—which can generate $^1O_2$ when irradiated with visible light under aerobic conditions—have attracted considerable attention because they have the potential for continuous self-disinfection in everyday environments [155-160]. A photoexcited PS can follow one of two reaction pathways called type I and type II. Active free radicals and radical ions are generated in the Type I reaction. In the type II reaction, energy is transferred from the PS to oxygen molecules, resulting in the generation of highly reactive $^1O_2$ [150, 154, 156]. Rose bengal (RB) is one of the most efficient and widely used singlet oxygen sensitizers [161]. Decraene et al. reported that cellulose acetate (CA) films containing 25 μM toluidine blue and RB had a reduced microbial load in both laboratory-based experiments [162] and clinical environments [163].

The $^1O_2$ produced by the action of UV radiation on potential photosensitizers in the cells of tissue is hazardous to human health because it induces inflammation, the formation of cataracts, premature skin aging, and skin cancer [164, 165]. It has been proposed that antioxidants should be used in combination with anatase-type titanium oxide (TiO_2)—which is a component of many sunscreen lotions—to reduce the potential adverse health effects of active oxygen species, including the $^1O_2$ generated by TiO_2 [166, 167]. The skin comprises three core layers. The outermost layer is the epidermis and is 10–120 μm thick [168]; keratinocytes constitute 90% of the cells in the epidermis [169]. Keratinocytes undergo continuous and rapid proliferation, and are thought to be continually regenerated. Depending on the stage of differentiations, keratinocytes leave the basal layer and move upwards. They then undergo terminal differentiation and form a continually shedding protective barrier at the surface of the skin [170]. This homeostasis is extremely important for maintaining the natural barrier function of the skin. Attack by $^1O_2$ damages keratinocytes, but the damage is much less severe than that induced by microorganisms. Moreover, cells recover from attack by $^1O_2$, which does not induce delayed destruction by apoptosis, and healthy mammalian cells are significantly more resistant to attack than bacteria [171]. $^1O_2$ usually causes little harm if the intracellular mechanisms that reduce the damaging effects work properly. Damaged cells are constantly being repaired by many cellular systems. If the frequency of damage events exceeds the repair capacity, the damaged cells are not repaired in time [172]. $^1O_2$ is much safer for the human skin than bacteria or viruses, but it cannot be said that there is no risk at all.

Our interest is whether the $^1O_2$ continuously generated from the self-disinfecting surface mentioned above may have an adverse effect on the human body. Normally, self-disinfecting surfaces, such as those covering furniture and walls, stop generating $^1O_2$ when touched by humans because light illumination is essential for the production of $^1O_2$. However, the self-disinfecting surfaces that cover screens—such as those used in smartphones and touch panels—do not stop generating $^1O_2$ when touched by humans because during use they are illuminated by back lights. The continuous generation of $^1O_2$ during contact with the skin is beneficial in terms of sterilization, but its effect on the skin is a concern. $^1O_2$ cannot penetrate mouse skin, regardless of the existence of a stratum corneum, because it is short-lived and highly reactive [173]. However, it is unclear whether $^1O_2$ invades and damages the epidermis. According to an experiment using 1,3-diphenylisobenzofuran (DPBF) for detection, the lifetime of $^1O_2$ is 2.8 s at 23°C and 1 atm, during which time it diffuses approximately 0.992 cm [174]. If the self-disinfecting surfaces mentioned above are positioned where humans will touch them, they will be more effective at preventing infection. However, the reported relative longevity of $^1O_2$ in air may have adverse effects on human health, and may negatively affect self-disinfecting surfaces. It is unknown whether the $^1O_2$ generated by self-disinfecting surfaces can invade the skin when humans touch them.

In this chapter, the penetration of $^1O_2$ into a polymer film with an oxygen permeability coefficient close to that of human skin was investigated. The objective was to explore the possibility that human skin can be invaded by the $^1O_2$ generated by self-disinfecting surfaces. A CA film containing 5.5 mM RB was used as the self-disinfecting surface. $^1O_2$ was generated by irradiating the film with visible light. The formation of $^1O_2$ by a self-disinfecting surface during irradiation with visible light was confirmed using a molecular film containing the $^1O_2$ detector DPBF, and the antibacterial effect of the surface on *Escherichia coli* was determined. The penetration of $^1O_2$ into polymer films was investigated using a CA film containing 19.8 mM DPBF and ethyl cellulose (EC) film containing 16.9 mM DPBF. The diffusion of $^1O_2$ into the polymer film will be discussed herein.

5.2 Experiment

5.2.1 Materials

EC (ethyl cellulose 100 with a viscosity of 100 mPa·s (centipoise)) was purchased from Kishida Chemical Co., Ltd. (Osaka, Japan). RB (2,4,5,7-tetraiodo-3′,4′,5′,6′-tetrachlorofluorescein disodium salt; Acid Red 94) was purchased from Tokyo Chemical Industry Co., Ltd. (Tokyo, Japan). DPBF, acetone, and tetrahydrofuran (THF) were purchased from FUJIFILM Wako Pure Chemical Corporation (Osaka, Japan). CA used was the same one in the previous chapters. All the chemicals and reagents were of analytical grade and were used without further purification.

5.2.2 Characterization

FTIR spectroscopy was performed by the same way described in subsection 4.2.2. The thickness and the gap between the $^1O_2$ detector and the self-disinfecting surface were measured using a Dial thickness gauge (Mitutoyo corporation, kanagawa, Japan) at three or more positions. Except for the antibacterial experiment, $^1O_2$ production was detected by irradiating each film with an F32W-T fluorescent light source (Nichido Ind. Co., Ltd., Osaka, Japan). The illuminance of the light was 2000 lx, and was measured using a general light class A illuminance meter (YOKOGAWA 510 Luxmeter model 51011; Yokogawa Test & Measurement Corporation, Tokyo, Japan). The absorption spectra of the films were obtained using a UV-Vis spectrophotometer (UV-1650PC; Shimadzu Corp., Kyoto, Japan).

5.2.3 Preparation of films containing RB and DPBF

Films containing RB and DPBF were prepared according to the procedures described in Figure 5-1.

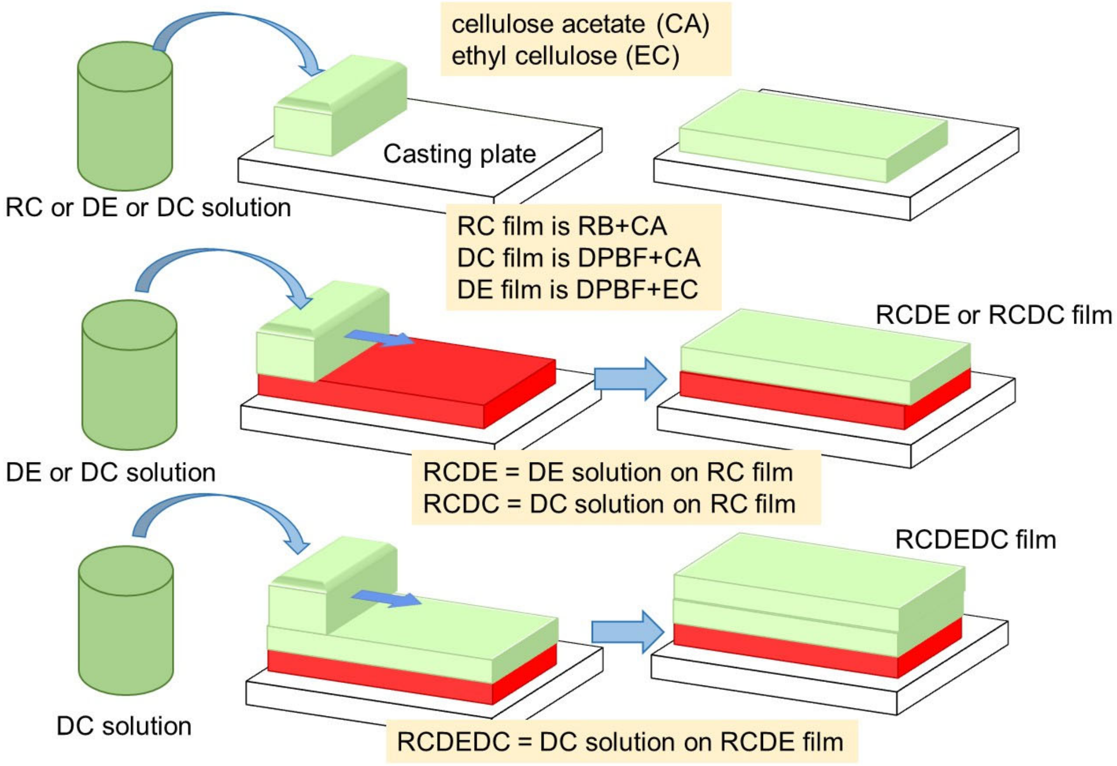

Figure 5-1. Fabrication of films containing photosensitizers (PSs)—i.e. rose bengal (RB) and 1,3-diphenylisobenzofuran (DPBF)

In a typical preparation, 10 mg of RB and 2.5 g of CA were dissolved in 25 mL of acetone. Two weir plates (each with a height of 530 μm, a length of 200 mm, and a width of 50 mm) were fixed in parallel 120 mm apart on a glass plate. The RB and CA solution (8 mL) was poured between the weir plates and the excess solution was removed with a glass rod to form a film, which was dried at 25 °C. The resulting film was thereafter referred to as an RC film. The RC film is represented in red in the figures because RB is red. The DE films, which comprised DPBF and EC, were produced using the same weight ratio of DPBF, polymer and solvent used for the RB film, and are represented in light green in the figures because DPBF is a yellowish fluorescent dye. All procedures were carried out in the dark. CA and EC films containing DPBF were prepared in the same way, and subsequently referred to as DC and DE films, respectively. The DE film was prepared using THF as the solvent instead of acetone. The thicknesses of each film were in the range 36 ± 5 μm. Similarly, two-layers film was prepared from the different solutions by depositing a second layer solution after the first layer had dried on a glass plate, and allowing the solvent to evaporate completely at 25 °C. A film in which a DPBF-containing solution was cast as a second layer on an RB-containing film, and a film that was further layered (a three-layers film) with a polymer solution, were also made in the same manner. The rule for naming the films was as follows: the first layer was indicated before the second layer, and the individual layers were defined with the acronym for the PS placed before the acronym for the polymer. For example, films made by casting a DE solution or a DC solution on an RC film were referred to as RCDE and RCDC films, respectively. The thicknesses of the double-layer films were in the range 72 ± 5 μm. Optically clear films were obtained in all cases. The dried films were stored in foil laminate bags until required. The PS molar concentrations were calculated as [PS] = n/m [175], where n/m is the ratio of the number of moles of PS to the mass of the film, and ρ is the density of the film. Using the molar mass of RB (973.67 g mol^{-1}), the molar mass of DPBF (270.33 g mol^{-1}), and the densities of CA (1.34 g cm^{-3}) and EC (1.14 g cm^{-3}), the concentrations of the PSs in RC, DC, and DE films were calculated as 5.5, 19.8, and 16.9 mM, respectively.

5.2.4 Confirmation of $^1O_2$ generation in the RC film

$^1O_2$ generation in the RC film was confirmed by the release of $^1O_2$ from the RC film into the air, and by an antibacterial study. The release of $^1O_2$ into the air was confirmed by increasing the concentration of DPBF and adding a very small amount of EC to the THF solution. THF was used as a solvent instead of ethanol to obtain a uniform distribution of DPBF molecules by referring the method described in the literature [174]. A THF solution of DPBF (32.8 mM) was prepared in the dark, and EC (0.01 wt%/volume) was dissolved in the solution. While shading, 60 μL of the solution was applied to a glass slide (76 × 26 mm), which was left in flowing air at 25 °C for 60 min to dry. The DPBF molecules were spread on the glass to form a 4-μm thick transparent layer. With the DPBF surface facing upwards, an RC film fixed on a cover glass was placed face-to-face with the DPBF layer; the two layers were kept 80 μm apart using a spacer. Visible light was irradiated from the upper side (the cover glass side) for 600 s, and the change in the absorbance of the DPBF at 416 nm was detected. $^1O_2$ irreversibly oxidizes the conjugated structure of DPBF, and the reduction in absorption by DPBF at 416 nm corresponds to $^1O_2$ generation [176, 177]. For comparison, the same experiment was performed without the RC film. Antibacterial activity studies on an RC film and a CA film (the control) were performed according to Japanese Industrial Standard JIS R 1752 2020 (the visible light-responsive photocatalyst, antibacterial, film adhesion method) using *E. coli* (NBRC 3972) as the test microorganism. Briefly, a sterilized humidity control filter paper was placed on the bottom of a sterilized storage petri dish, an appropriate amount of sterilized water was added to control the humidity, and a glass rod was placed on it. The test pieces were 50 ± 2 mm × 50 ± 2 mm × 36 ± 5 μm, and were sterilized for several minutes with ultraviolet radiation before use. The sterilized test piece was placed on the glass rod, 0.15 mL of the planktonic test bacterial solution was dropped onto the test piece, the bacterial solution was covered with a polyethylene film, and the moisturizing glass was placed on the petri dish. Excepting three control pieces, light irradiation tests were performed immediately after inoculation with the test bacterial solution to measure the viable cell count. A white fluorescent lamp (FHF32EX-N-H, Panasonic Corporation, Osaka, Japan) was used as the light source. The experiment was performed for 4 h both in the dark and in visible light (1000 lx), and was carried out three times to obtain an average value. After inoculation, the test pieces were immediately washed with 10 mL of Digest-Soy Lecithin Polysorbate 20 Medium (SCDLP), proper dilution, and the number of viable cells in each test was counted after incubation at 35 °C for 16h.

5.2.5 $^1O_2$ penetration into polymer films following contact

The ability of $^1O_2$ to penetrate a polymer film was determined using DE and DC. The film samples were 20 mm × 40 mm in size. As illustrated in Figure 5-2, the RC film was layered on either a DE or a DC film, and sandwiched between two glass plates to achieve contact without a gap. The arrangement was then irradiated from the upper side. The absorbance level of the DE and DC films were measured after 30, 60, 120, 300, 600 s. For comparison, the experiment was also carried out without RC film. All the experiments were performed at least three times to confirm reproducibility. The same experiment was

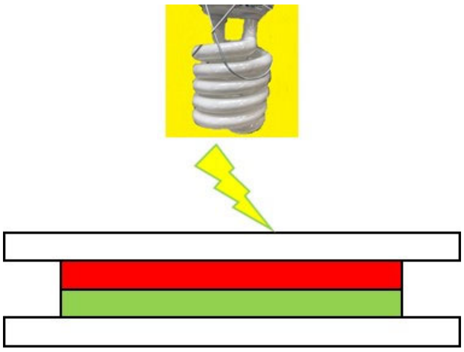

Figure 5-2. Cross-sectional illustration of $^1O_2$ detection during irradiation with visible light

conducted with the film placed on the opposite side—i.e., the DE or DC film was layered on the RC film before irradiation.

5.2.6 $^1O_2$ penetration into polymer films by casting

RCDE and RCDC films were used to determine whether the $^1O_2$ generated in the RC film would react with the DPBF in another film. The films were sandwiched between glass plates and irradiated, illustrated in Figure 5-2.

5.3 Results and discussion

5.3.1 Generation of $^1O_2$ in the RC film by irradiation with visible light

The rate of $^1O_2$ production is related to decrease in absorbance by DPBF as a function of irradiation time [178]. Using DPBF to detect $^1O_2$, the generation of $^1O_2$ in the RC film was investigated, and the results are shown in Figure 5-3. The RC film significantly reduced the absorbance of DPBF, indicating that it generated $^1O_2$ when irradiated with visible light. A similar result has been reported for the reaction between $^1O_2$ generated by excited meso-tetra(*o*-dichlorophenyl)porphine and DPBF [174].

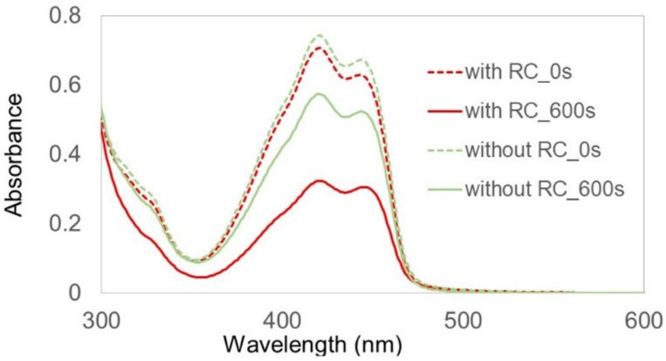

Figure 5-3. Observed UV-Vis absorption spectra before and after irradiation with and without the RC film

There was a slight decrease (23%) in absorption at 416 nm without the RC film compared with the decrease (62%) caused by $^1O_2$, which demonstrated that DPBF itself acted as a weak sensitizer [179, 180], and DPBF reacted with the $^1O_2$ generated by the reaction between the excited DPBF and oxygen.

The antibacterial activity of the RC film was confirmed. All the tests satisfied the requirements for validity specified in JIS R 1752. Log reduction [160] was used to quantify the living microbes. Using a logarithmic scale, the ratio of the number of viable colonies after irradiation with the photosensitizer to the number of viable colonies in the control study (without PS) under the same treatment conditions was calculated. Equation (5-1) was used to evaluate antibacterial activity, and the results are summarized in Table 5-1.

$$\text{Log reduction} = \log_{10}(\mathrm{A}) - \log_{10}(\mathrm{B}) \qquad (5-1)$$

where, A and B are the numbers of living microbes in dark and after irradiation with visible light, respectively. The antibacterial activity of the RC film increased dramatically when it was incubated in visible light compared with when it was incubated in the dark. Therefore, it was concluded that the $^1O_2$ generated in the RC film by the action of visible light killed the *E. coli*.

Table 5-1. Antibacterial activity of the RC film compared with that of the blank

Sample	Log reduction
Blank (CA film without RB)	-0.13
RC film	3.55

These results proved that the RC film used in the present study produced sufficient $^1O_2$ to kill the *E. coli* following irradiation with visible light.

5.3.2 Invasion of $^1O_2$ following contact with a film that has an oxygen permeability coefficient close to that of skin

The oxygen permeability coefficient is expressed as the volume of oxygen (cm^3) per unit area (cm^2) in a unit time (s) when there is a unit pressure difference (cmHg) with a given unit thickness (cm) of polymer film [181]. The oxygen permeability coefficients of skin, an EC film, and a CA film are 3.07×10^{-9} [182], 2.0×10^{-9} [183], and 8×10^{-11} [183, 184] cm^3·cm/cm^2·s·cmHg, respectively. Furthermore, when irradiated with light, the PS in a polyurethane layer (30 μm thick) with an oxygen permeability coefficient smaller than that of EC but slightly larger than that of CA produced $^1O_2$, which killed the microorganisms accumulated on its surface [185]. In the present study, $^1O_2$ generated by the RB in the cellulose acetate layer migrated into the air, and its bactericidal effect on the surface was confirmed. The invasion of $^1O_2$ following contact was investigated using DE and DC films, and the results are shown in Figure 5-4. Figure 5-4a and 5-4b show the spectral changes of the DE and DC films when irradiated in the presence or absence of the RC film. The DE and DC films produced a sharp absorbance peak at 416 nm compared with the absorbance of DPBF molecules accumulated on a glass sheet. This indicated that the dye aggregation was dramatically reduced when the DPBF molecules were dispersed in the polymer. The reduction in absorbance by the DE and DC films after 600 s was lower than that by the DPBF molecules. Therefore, we concluded DPBF dispersed in the resin was mildly self-oxidized, probably because the supply of oxygen into the film was rate-determining. The degradation rate of DPBF, k, can be determined as follows:

$$kt = \ln\frac{[\mathrm{DPBF}]0}{[\mathrm{DPBF}]\mathrm{t}} \qquad (5-2)$$

where $[\mathrm{DPBF}]_0$ and $[\mathrm{DPBF}]_t$ are the concentration of DPBF determined by absorbance at reaction times zero and t, respectively. Figure 5-4c and 5-4d show that the reaction kinetics of self-oxidation of DPBF followed a pseudo-first-order rate law, which means that apparently the concentrations of oxygen and photosensitizer did not change during the experiment [186]. Regardless of the presence of the RC film, the DPBF degradation rates in the DE and DC films were 0.0004 s^{-1} and 0.0002 s^{-1}, respectively. The result that EC, which is relatively permeable to oxygen, had a faster DPBF degradation rate was thought to be because the oxygen in the ground state increased the rate of DPBF photolysis, as previously reported [187]. To confirm that ground state oxygen affects the photodegradation of DPBF in the film, a DE film was irradiated with light in an argon atmosphere. As indicated by the red line in Figure 4c, the photobleaching rate of DPBF was reduced by blocking oxygen. It is highly possible that DPBF itself acted as a weak photosensitizer in the DE film. Importantly, the reduction in absorbance by the DE and DC films hardly changed regardless of contact with the RC film. Both its reaction with the naked DPBF molecular layer and its antibacterial effect on *E. coli* confirmed that the RC film produced $^1O_2$. The results were the same when the RC film and DE or DC film were overlaid in reverse (the data are indicated by the blue lines in Figure 5-4d). The DPBF in the polymer was unable to react with external $^1O_2$, unlike the naked DPBF molecules. Possibly the reason for this was that the $^1O_2$ generated by the RC film was incapable of invading the DE or DC films, or decomposed before reacting with the DPBF in the films. Given these results, it is unlikely that singlet oxygen would reach and attack any of the tissues in the vicinity of the epithelium.

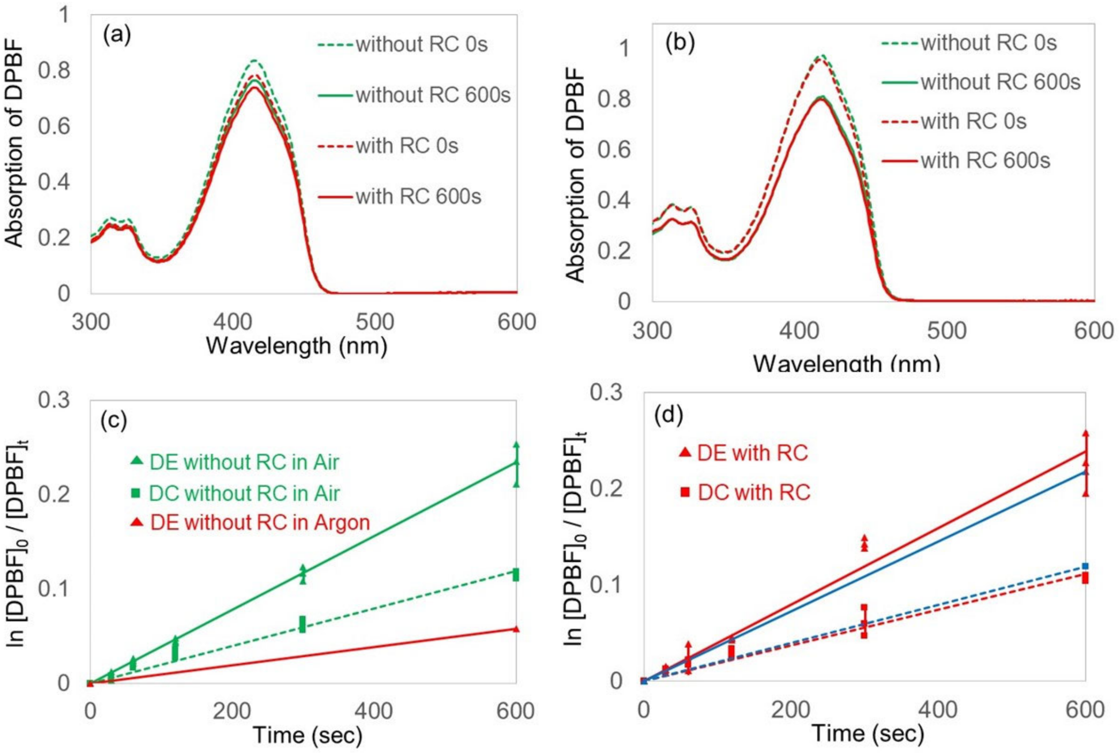

Figure 5-4. UV-Vis absorption spectra of DE and DC films before and after irradiation with and without the RC film: (a) the DE film, and (b) DC film. Changes in absorption intensity over time: (c) without the RC film in air (green lines) and in argon (red line), and (d) with the RC film (reverse irradiation is expressed by the blue line)

5.3.3 $^1O_2$ movement between the cast films

When an $^1O_2$-generating PS and an $^1O_2$ probe are present in the same polymer film, the $^1O_2$ generated inside the polymer following the consumption of external oxygen diffuses through the polymer matrix and reacts with the $^1O_2$ probe in the same polymer matrix [179, 187]. Using RCDE and RCDC films, we determined whether $^1O_2$ moves between different films when the films are integrated by casting. The change in absorbance of the films over time, and the reduction in absorbance by DPBF over time are shown in Figure 5-5. Comparing to the overlapped films, the absorption changes of the films revealed that the $^1O_2$ produced in the RC film reacted with the DPBF present in the film on the other side. The difference between the simply stacked films and the cast films resulted in a significant difference in absorption at 416 nm, which is attributable to absorption by DPBF, resulting from the reaction between DPBF and $^1O_2$. This was considered to be due to a decrease in the chance for contact between $^1O_2$ and external oxygen between the cast films, a decrease in the opportunity for the deactivation of $^1O_2$, or resistance to an invasion of the unbound polymer layers by $^1O_2$. The reaction kinetics of $^1O_2$ and DPBF in the RCDE film followed a pseudo-first-order rate law, whereas those in the RCDC film followed a pseudo-second-order rate law. In the DE film, which had relatively high oxygen permeability, the generation and diffusion of $^1O_2$, and the reaction between $^1O_2$ and DPBF proceeded in a well-balanced manner. However, in the DC film, which had relatively low oxygen permeability, the diffusion of $^1O_2$ into the DC film might have affected the reaction rate between $^1O_2$ and DPBF. Interestingly, the RCDC film made from the same CA material could not be separated, whereas despite integrated casting, the RCDE film was easily separated into two films—i.e., RC and DE—by hand.

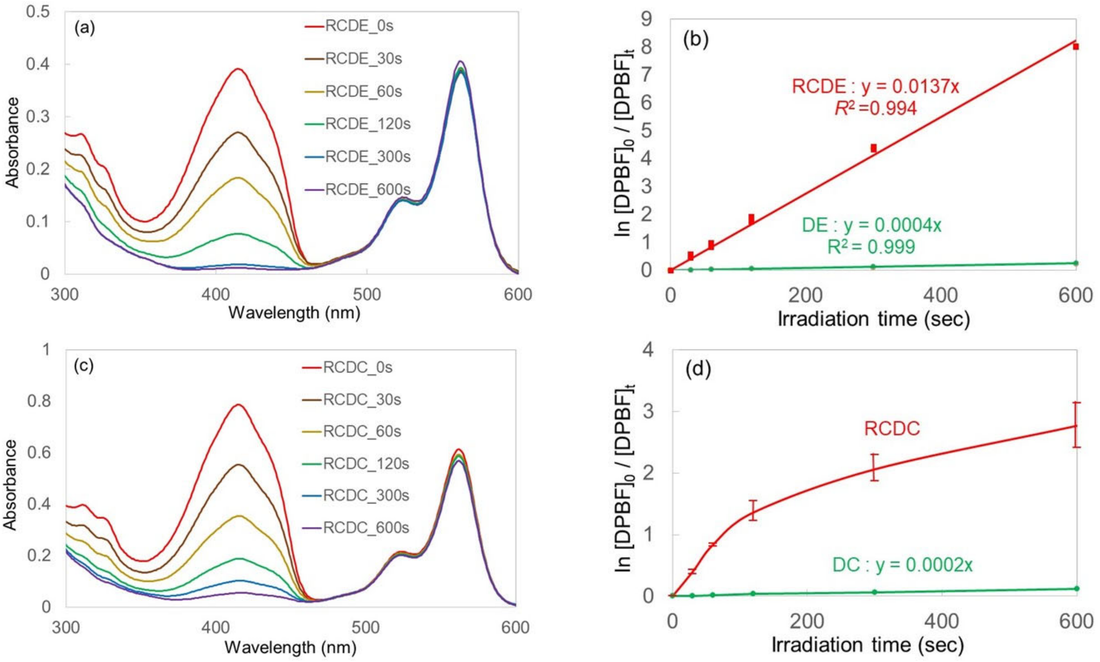

Figure 5-5. UV-Vis absorption spectra and changes in absorption intensity over time during irradiation: (a, b) the RCDE film, and (c, d) the RCDC film

5.3.4 FTIR analysis of the separated film

The RCDE film obtained by casting was peeled off by hand after the light irradiation reaction as illustrated in Figure 6. The RC and DE films were both 32 μm thick. The CA and EC films seemed to be incompatible. The bonded and non-bonded surfaces of each film were analyzed by FTIR (Figure 5-6). The absorption spectra of the PS in the films could not be confirmed. Thus, absorption by CA and EC was subtracted from the spectrum, and the range 1300–1800 cm^{-1}, where the characteristic absorption of the PS appears, was expanded and compared. There is a noticeable band at 1716 cm^{-1}, which may be attributed to the carbonyl functional group of RB [188]. This absorption was observed from both sides of the RC film but not from the DE film. In the presence of $^1O_2$, DPBF readily undergoes a 1,4-cycloaddition reaction, forming endoperoxide, which in turn decomposes to produce 1,2-dibenzoylbenzene (DBB) as shown in Figure 5-7 [176]. The band attributable to the carbonyl group of DBB obtained by the oxidation of DPBF should be visible at 1660 and 1675 cm^{-1}, but it was not clearly distinguishable in the FTIR spectra. The absorption band at 1300–1600 cm^{-1} attributable to an aromatic ring was difficult to assign because both RB and DBB contain aromatic rings. The migration of RB from the RC film to the DE film during casting was not recognized by the FTIR analysis.

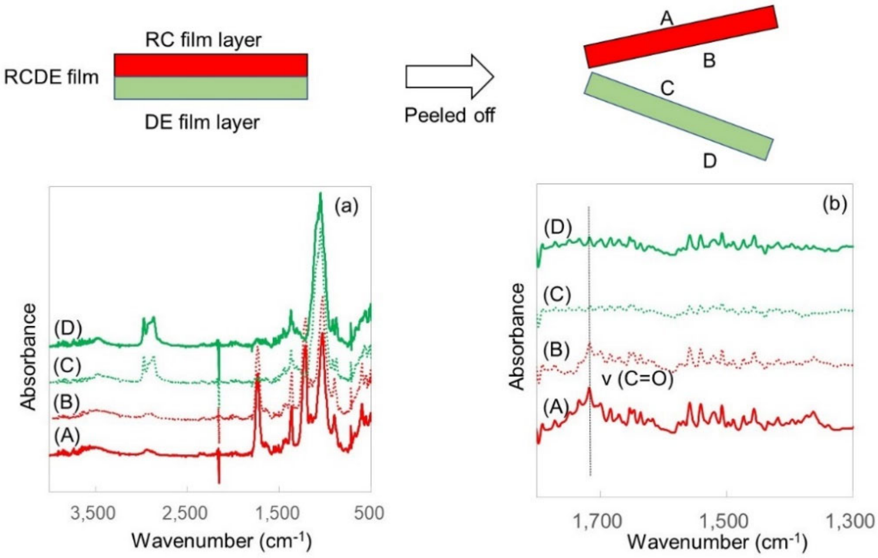

Figure 5-6. Fourier-transform infrared (FTIR) spectra of the separated RCDE films: (a) the obtained spectra, and (b) an enlarged portion of the spectra after subtraction of the absorption by CA and EC

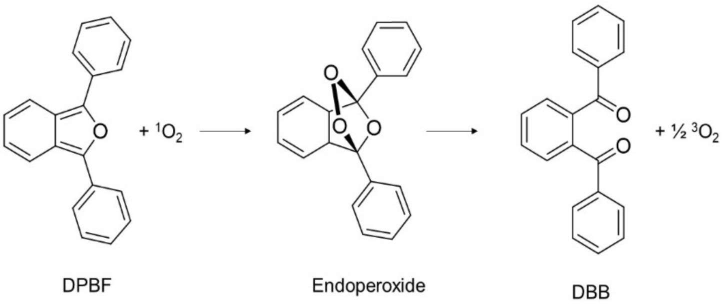

Figure 5-7. Reaction of 1,3-diphenylisobenzofuran (DPBF) with $^1O_2$

5.3.5 Confirmation of RB transfer from the RC film to the DE film by UV-Vis spectroscopy

Absorbance was measured using the same sample used for FTIR, and the results are shown in Figure 5-8. The UV spectral intensity at 561 nm, which is attributable to absorption by RB, suggests that approximately 10% of the RB inside the RC film was transferred to the DE film side when the DE solution was cast onto the RC film, and approximately 90% of the RB remained in the RC film. The distance traveled by the RB following casting was thought to be thinner than the thickness of the DE film because the thicknesses of the RC and DE films were almost the same, and the opposite side of the bonded surface of the DE film was not colored red. Regarding the RCDE film, it seems that some of the $^1O_2$ was generated by RB near the bonded surface side of the DE film, and reacted with the DPBF; the DPBF was subsequently completely oxidized to DBB over time, as indicated by the disappearance of the absorbance band at 416 nm, which is attributable to DPBF. The same thing was thought to occur in the case of the RCDC film, which could not be separated.

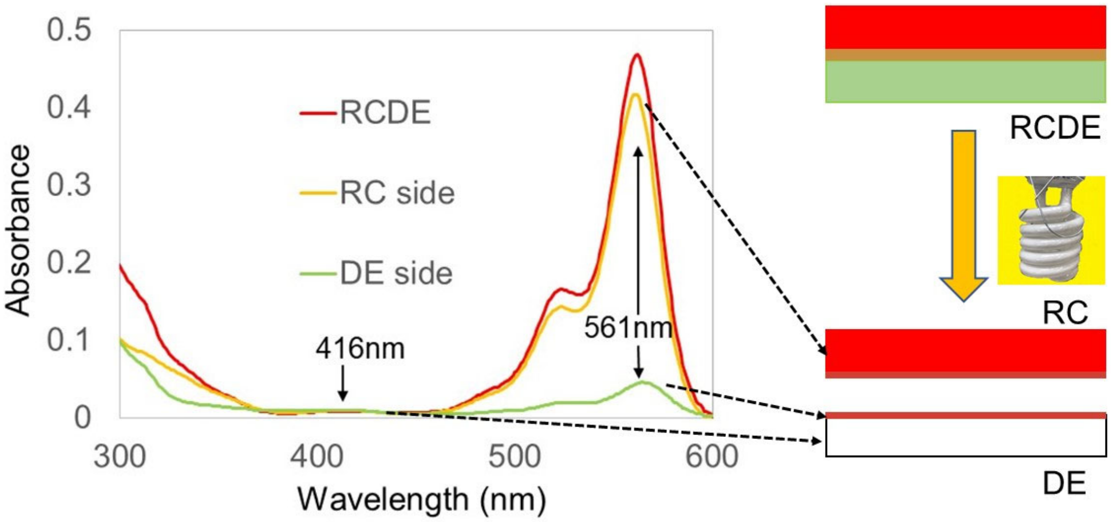

Figure 5-8. UV-Vis absorption spectra before and after peeling: (a) RCDE, (b) RC, and (c) DE

5.3.6 Diffusion of $^1O_2$ in the polymer films

The CA and EC films apparently existed independently, even after casting. Therefore, a triple-layered RCDEDC film was prepared by laminating the RC solution, the DE solution, and the DC solution in that order, as shown in Figure 1. The RCDEDC film was irradiated with visible light for 600 s, and the diffusion of $^1O_2$ was investigated by UV-Vis spectroscopy. Figure 5-9 shows the UV-Vis spectrum before and after irradiation.

There was a significant decrease in absorption peculiar to DPBF at 416 nm. In contrast, the absorbance at 416 nm by a DEDC film (formed by casting a DC solution onto a DE film without an RC layer) was hardly reduced by irradiation (Figure 5-10). Therefore, in the case of the three-layered film, the $^1O_2$ generated in the RC film by light irradiation probably reacted with the DPBF. Following irradiation, the three-layered film was separated into three films, and the UV-Vis spectrum of each film was obtained, as shown separately in Figure 5-9b. The separated RC, DE, and DC films were 34, 37, and 35 μm thick, respectively. Interestingly, the DE film adjacent to the RC film absorbed light at

561 nm, which may be attributed to RB, but the DC film positioned at the third layer did not. This indicates that the transfer of the RB following casting did not extend beyond DE film.

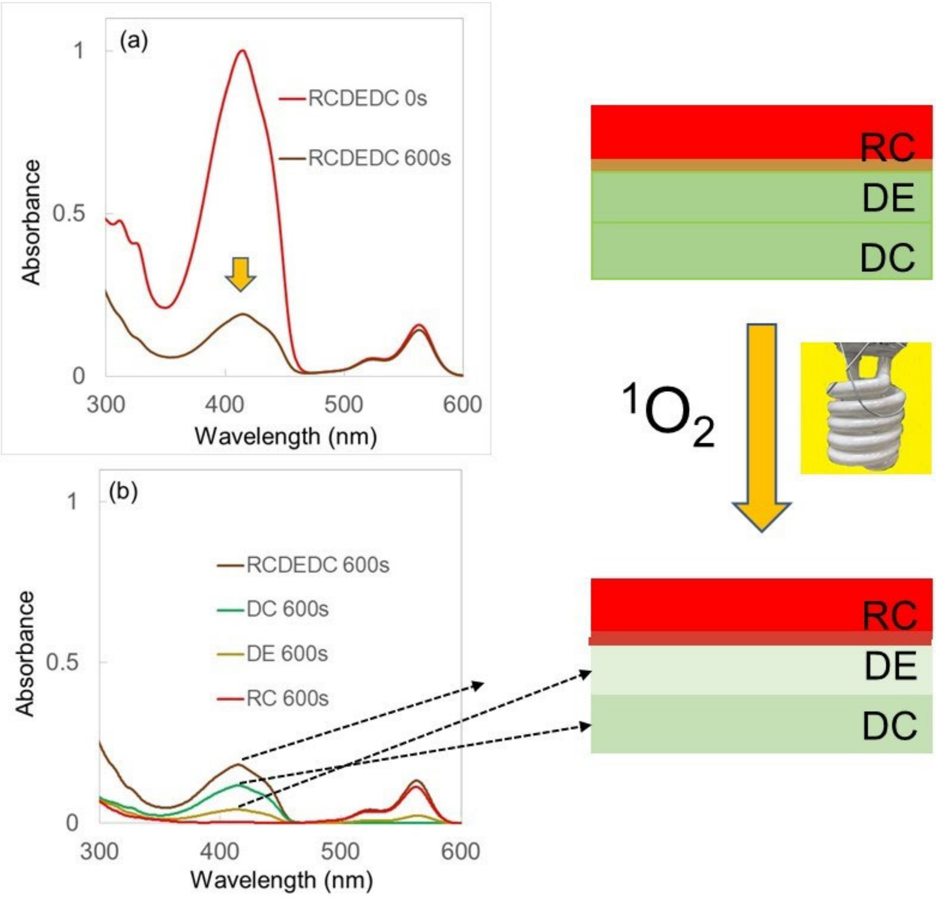

Figure 5-9. UV-Vis absorption spectra of the RCDEDC film before and after irradiation: (a) before and after, (b) the irradiated RCDEDC film and the peeled films

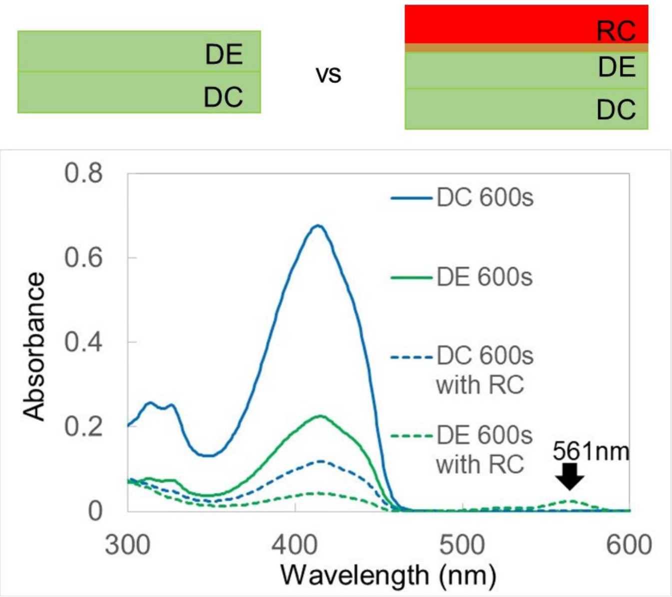

Figure 5-10. UV-Vis absorption spectra of irradiated DC and DE film after peeling: DC of DEDC (blue line), DC of RCDEDC (blue dotted line), DE of DEDC (green line), and DE of RCDEDC (green dotted line)

A comparison of the UV spectral intensities at 561 nm attributable to absorption by RB reveals that, approximately 10% of the RB in the RC film transferred to the DE film when the DE solution was cast onto the RC film as in the case of the two-layer RCDE film, whereas there was no absorption at 561 nm in the third DC film next to the DE film. However, absorption at 416 nm, which may be attributed to DPBF, decreased significantly in both the DE and DC films, which did not contain RB at all. The DEDC film was irradiated to provide a control for the RCDEDC irradiation experiment, and the absorbance of each separated film is shown in Figure 5-10 for comparison. In the case of three layers, as with two layers, it was confirmed that absorbance attributable to DPBF was significantly reduced when the RC film was cast compared with when it was not. Apart from the general decrease in absorbance, the absorbance of the DC film at 416 nm was larger than that of the DE film in both the DEDC and RCDEDC films. The difference in DPBF concentration in the original film, the difference in oxygen permeability, and the transfer of DPBF from the DE film to the DC film as a result of casting may explain this observation but further investigation is required on this point. The data verified that some of the $^1O_2$ reached the DC film through the DE film without deactivation. It has been reported that active oxygen species diffuse at least 100 μm into a hydroxypropyl methylcellulose (HPMC) film [189]. Our data proved that $^1O_2$ was able to move between the different polymer layers. This finding suggests the possibility of a new method for detecting $^1O_2$, which has mostly been detected in solution in the past [175-178, 190, 191]. When DPBF is incorporated into a solid film it is less susceptible to fading than DPBF in solution when exposed to light. Therefore, such an arrangement might be expected to improve the detection of $^1O_2$.

5.3.7 Consideration on the $^1O_2$ permeation of the bilayer films obtained by casting and overlapping

A bilayer film with an oxygen permeability coefficient close to that of a CA film deposited onto a film containing a singlet oxygen sensitizer, which was in turn deposited on a glass plate allowed oxygen to pass through the polymer layers while consuming oxygen by generating $^1O_2$ [187]. The diffusion of oxygen across interfacial boundaries indicates that $^1O_2$ can move between polymer layers. A double-layer film that allows the passage of oxygen might also allow the transmission of singlet oxygen. In the experiments reported herein, the film was simply sandwiched between glass plates, so there may have been sufficient oxygen around the film. This suggestion is supported by the fact that the reaction between $^1O_2$ and DPBF in the DE film followed a pseudo-first-order equation. The number of singlet oxygen molecules depends mainly on the photostability of the PS and the accumulation of singlet oxygen in the film depends on the PS quantum yield and on the lifetime of singlet oxygen in the polymer matrix. Owing to its high quantum yield, RB ensures relatively high $^1O_2$ production [192]. With regard to the photostability of RB, almost no photobleaching occurred during irradiation with visible light for up to 600 s. It has been reported that $^1O_2$ has quite a long "existence time" in solid polymers despite having a relatively short intrinsic lifetime [193]. The lifetimes of $^1O_2$ in CA and EC used for the polymer matrix in these experiments are reported as 30.4 μs and 24.3 μs, respectively [194]. In the literature [176], it has been reported that the probability of a reaction between DPBF and $^1O_2$ is dependent on the solvent, which affects the intrinsic lifetime of $^1O_2$, and that the DPBF in an EtOH/D_2O solution traps more than 70% of the generated $^1O_2$. In the present study, we think that a considerable amount (but not all) of the generated $^1O_2$ was captured by DPBF, this is because the intrinsic lifetime of $^1O_2$ in films has reportedly equivalent to—or longer than—in an EtOH/D_2O solution. With regard to RCDE and RCDC, it may be assumed that the large amount of $^1O_2$ produced by the RB molecules through the consumption of ambient oxygen could have diffused into the neighboring cast polymer layer owing to its relatively long lifetime in the polymer matrix. It is thought that the reaction between $^1O_2$ and DPBF decreases the oxygen concentration inside the polymer because half of the $^1O_2$ molecules are captured by the DPBF as it is oxidized to DBB [175]. It is reasonable to suppose that the continuously generated $^1O_2$ diffuses into the polymer to compensate for the reduced concentration of oxygen in the polymer films.

However, when the films were simply stacked together, they were surrounded by abundant oxygen. Possibly the $^1O_2$ emitted by the RC was unable to invade the DPBF film because the film was already replete with oxygen, and there was no means by which it could be removed. Therefore, it is probable that the $^1O_2$ was incapable of reacting with the DPBF inside film. In the case of the skin, oxygen is absorbed by cutaneous respiration [195], so $^1O_2$ may be absorbed at the same time. However, we believe that the deactivation of $^1O_2$ by ambient oxygen prevails over the invasion of $^1O_2$ by physical contact with a self-disinfecting surface. Given these results, it is unlikely that $^1O_2$ would reach and attack any of the tissues in the vicinity of the epithelium following physical contact with a self-disinfecting surface.

When induced in CA films, RB is photobleached by visible light [196]. Therefore, it is necessary to solve the problem of photobleaching if RC films are to have potential as practical antibacterial films in industrial applications. With regard to this point, it is discussed in the next chapter.

5.4 Conclusion

This chapter proved that the $^1O_2$ produced by a self-disinfecting surface—which comprised RB and CA—was incapable of penetrating a film with an oxygen permeability close to that of skin through mere contact. However, the $^1O_2$ produced by the self-disinfecting surface was able to kill microorganisms, and was capable of moving between polymer layers when the films were joined together. We found that the detection of $^1O_2$, which has mostly been done in solution to date, is also possible using a solid film containing a probe. These findings suggest that self-disinfecting surfaces that produce singlet oxygen may be used safely to improve hygiene in daily life, and solid films can be used as a new means of detecting $^1O_2$.

Chapter 6

Fabrication and evaluation of durable, optically clear, and self-disinfecting films

6.1 Introduction

Infectious diseases caused by microorganisms, such as bacteria and viruses, are a major public health problem [197]. Antibiotics significantly reduce mortality caused by infectious diseases and are one of the most important discoveries in the history of medicine [198]. However, the frequent use of antibiotics has caused the emergence of antibiotic-resistant strains that cannot be easily treated, even in the hospital environment [197]. Antibiotic resistance has created a need to develop viable alternatives to antibiotics for the prevention of infectious diseases [199, 200].

Singlet oxygen ($^1O_2$) is highly reactive and able to attack virion membranes, cell membranes, essential enzymes, and nucleic acids, which leads to inactivation or death by oxidative stress [29, 152, 156, 158]. The use of $^1O_2$ is nonspecific to the target microorganism, has few side effects, prevents the regrowth of microbes and presents limited opportunities for resistance mechanisms to develop because of the mode of action and type of biochemical targets (lethal multitarget process) [201-203]. Moreover, mutants resistant to this approach have never been detected [204]. Therefore, the development of materials that generate $^1O_2$ by photoactivation is a promising approach to infectious disease prevention that may replace or reduce the burden on antibiotics and the unintended consequences of their use [197, 200].

The spread of microbes and viruses, and resulting infections, is a serious global health concern with increasingly severe consequences as the world becomes more interconnected. The effects of outbreaks can be suppressed to some extent by reducing direct contact with infected individuals or indirect contact with contaminated objects and surfaces [155, 159]. Self-disinfecting surfaces such as fabrics, paper, films, and coatings may play a vital role in preventing the transmission of pathogens. Accordingly, films and structures containing a photosensitizer (PS) that generates $^1O_2$ upon irradiation with visible light have been researched because they may be able to continuously self-disinfect hospitals or other indoor environments [155, 159, 203, 205, 206].

Numerous studies have examined organic PS molecules to induce the lethal photosensitization of bacteria, including phenothiazines such as toluidine blue O [207] and halogenated xanthenes such as rose Bengal [152], acridines [208], porphyrins [209], and phthalocyanine (Pc) derivatives [210-212]. Rose bengal (RB) is a well-known $^1O_2$ sensitizer [161]. It is excited to its excited species upon irradiation with visible light, and the excited state species activate molecular oxygen to $^1O_2$. Decraene et al. reported cellulose acetate (CA) films containing 25 μM toluidine blue O and the same amount of RB killed microbes when illuminated with white light [162] and reduced the microbial load in a clinical environment [163]. Ideally, self-disinfecting surfaces should be activated by room light, easy to prepare, nonspecific to pathogens, scalable, and durable. However, most PSs, such as phenothiazines [212-214], RB [215, 216], and porphyrins [217], undergo photobleaching under room light irradiation, which restricts their long-term utilization.

Pcs have been shown to be more stable than RB with respect to photooxidation [215] when homogenously distributed throughout the polymer matrix. However, Pc molecules tend to aggregate when dispersed in CA films [218], which affects their optical properties. Preventing aggregation relies on inducing steric isolation of the Pc core, and substitution with bulky groups in solution has led to reduced aggregation of Pc or prevented it entirely [219-222]. Furthermore, the packing structure of Pc might be inhibited by introducing a substituent with large steric hindrance, such as a phenoxy group, to improve solubility in and compatibility with the resin. The phenoxy group can also shift the absorption wavelength to improve the transmittance (transparency) of visible light.

Considering the balance between the transmission of visible light and the light sterilization effect of its absorption, we addressed these issues by synthesizing and using phenoxy-substituted zinc Pc with the name [2,3,9,10,16,17,23,24-octakis(2-chloro-4-methoxyethoxycarbonylphenoxy)-1,4,8,11,15,18,22,25-octafluoro-29H,31H-phthalocyaninato(2-)-N29, N30, N31, N32] zinc (PPcZn). The structure of PPcZn is expected to confer chemical robustness against the generated $^1O_2$ [223]. The bulky phenoxy groups in PPcZn should effectively protect this molecule from aggregation and facilitate its homogeneous distribution in the polymer matrix. Site isolation without aggregation in the polymer matrix is an important feature, since aggregation diminishes the $^1O_2$ yield, shortens the lifetime of the excited states, and produces inefficient intersystem crossing. PPcZn is also chemically and thermally stable while being photoreactive, features that make it an attractive choice for research.

The photometric monitoring of 1,3-diphenylisobenzofuran (DPBF) degradation is a widely used method for indirect $^1O_2$ detection. The mechanism of $^1O_2$ detection by DPBF is its reaction with $^1O_2$ to form endoperoxide, which then irreversibly decomposes to 1,2-dibenzoylbenzene (DBB) [176]. As demonstrated in chapter 5, $^1O_2$ generated by irradiating an RB-containing film was detected using a solid film containing DPBF [224].

In this chapter, we synthesized PPcZn in which bulky phenoxy groups were arranged and dispersed it in a CA film to create a transparent film. We confirmed the aggregation state of the PS molecule in the films by changing the concentration of PPcZn [225] and comparing the rate of $^1O_2$ formation under visible light irradiation using a film containing DPBF. The antiviral property of the film was evaluated, and the continuity of $^1O_2$ generation was tested after six months. Film durability was also measured to evaluate its practicality.

6.2 Experiment

6.2.1 Materials

CA, RB, EC, DPBF, acetone, and THF were the same ones used in chapter 5. Zinc iodide (II) were purchased from Sigma-Aldrich Japan (Tokyo, Japan). Methyl cellosolve was purchased from Tokyo Chemical Industry Co., Ltd. (Tokyo, Japan). Benzonitrile was obtained from Nippon Shokubai Co., Ltd. (Osaka, Japan). Methanol and dimethyl acetoamide (DMAc) were purchased from FUJIFILM Wako Pure Chemical Corporation (Osaka, Japan). All the chemicals and reagents used in the study were of analytical grade and used as received.

6.2.2 Measurement

NMR spectra were measured with an ECZ600R spectrometer (JEOL Ltd., Tokyo, Japan) at 20 °C. Proton spectra were referenced to $Si(CH_3)_4$ as the internal standard. ^{19}F NMR spectra were referenced to monofluorobenzene as an external standard at $\delta = -113.15$ ppm. Mass measurements were performed with liquid chromatography-mass spectrometry (Synapt G2, Waters Corporation, Milford, MA, USA) in LC-QTOF/MS ESI mode (negative) and with MALDI-TOFMS (Autoflex III Bruker, Billerica, MA, USA). The thickness of the films, the illuminance of the light, $^1O_2$ production from the films, and the absorption spectra of the films were measured by the same manner described in the subsection 5.2.2. A white fluorescent lamp (FL20SSW/18, Mitsubishi Electronic Corporation, Tokyo, Japan) with a sharp cut filter (Type B) was used as the light source for the antiviral experiment. The tensile tests were performed using a tensile testing machine (Autograph AGS-1kNX; Shimadzu Corp., Kyoto Japan) at room temperature (controlled at 25 °C).

6.2.3 Synthesis of PPcZn

PPcZn was synthesized in the two steps illustrated in Figure 6-1 based on a reported procedure [226].

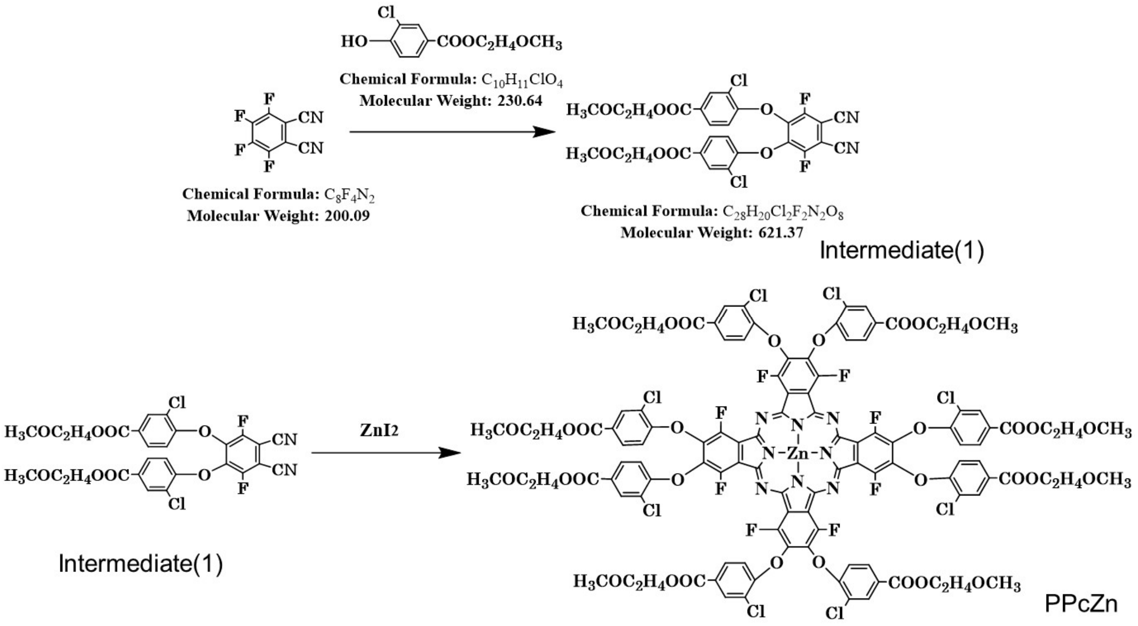

Figure 6-1. Synthesis of PPcZn

The yield of the first step to obtain intermediate (1) was 64.8%. ^{1}H NMR (600 MHz, $CDCl_3$, 20 °C, Figure S1 [227]): δ 8.07 (s, 2H), 7.90 (d, 2H), 6.85 (d, 2H), 4.47 t, 4H), 3.72 (t, 4H), 3.42 (s, 6H); ^{19}F{^{1}H} NMR ($CDCl_3$, 20 °C, Figure S2 [227]): δ 118.13 (s, 2F); Exact Mass: 620.06, Calc. for $C_{28}H_{20}Cl_2F_2N_2O_8$ (621.37): C 54.12; H 3.24; Cl 11.41; F 6.11, N 4.51%; Found: C 54.11; H 3.21; Cl 11.39; F 6.13; N 4.52%. Exact mass refers the measured mass value and calc. indicates the calculated average molecular weight. In the second step, 20.0 g (0.032 mol) of intermediate (1) was added to a 200 mL four-necked flask; 2.57 g (0.0081 mol) of zinc iodide (II) and 30.0 g of benzonitrile were charged into the flask and reacted at 160 °C for 24 h with stirring. After the reaction was complete, 52.7 g of methyl cellosolve were added to the reaction solution. The mixture was added dropwise to a solution of methanol and water to induce crystallization, and the crystals were separated by vacuum filtration. The obtained cake was then washed with a solution of methanol and water, followed by another vacuum filtration step. The washed cake was dried at 90 °C for 24 h using a vacuum dryer to obtain 17.35 g (yield 86.7%) of the target phthalocyanine (PPcZn). ^{1}H NMR (600 MHz, $CDCl_3$, 20 °C, Figure S3 [227]): δ 7.79 (m, 8H), 7.76 (m, 8H), 7.18 (m,8H), 7.17 (m,8H), 4.22 (m, 16H), 3.57 (m, 16H), 3.27 (m, 24H); ^{19}F{^{1}H} NMR ($CDCl_3$, 20 °C, Figure S4 [227]): δ 131.23 (m, 8F); Exact Mass: 2544.16, UV-Vis (DMAc): λ_{max} 695 nm ($\varepsilon = 3.1 \times 10^5$), Calc. for $C_{112}H_{80}Cl_8F_8N_8O_{32}Zn$ (2550.86): C 52.74; H 3.16; Cl 11.12; F 5.96, N 4.39%; Found: C 52.51; H 3.22; Cl 11.05; F 5.91; N 4.35%.

6.2.4 Fabrication of PS-containing films

Films containing PSs (PPcZn and RB) and evaluated as self-disinfecting surfaces were prepared using the procedures described in the upper part of Figure 6-2.

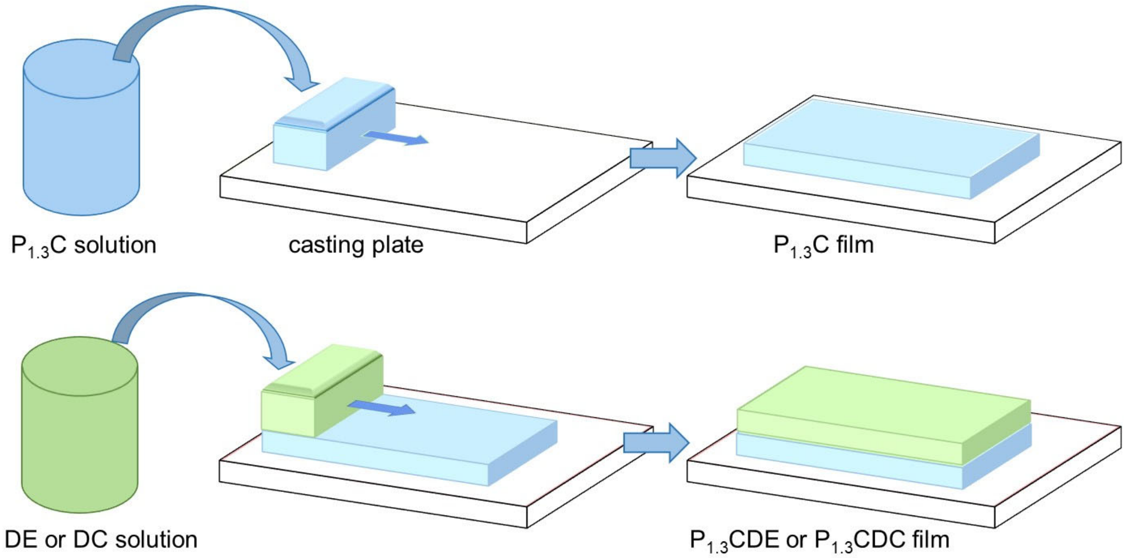

Figure 6-2. Illustration showing the fabrication process for PS-containing films

In a typical preparation, 3 mg of PPcZn and 1.2 g of CA were dissolved in 12 mL of acetone. THF was available to use as a solvent, but acetone was used in this study based on a result in subsection 5.2.3. The resulting solution was cast to form a film on a glass plate, which was dried at 25 °C and is referred to as a $P_{1.3}C$ film (based on the PS, its concentration, and the polymer matrix). The PS molar concentrations were calculated using the molar mass of PPcZn (2550.86 g mol^{-1}), the molar mass of RB (973.67 g mol^{-1}), and the density of CA (1.34 g cm^{-3}) according to subsection 5.2.3. The films were defined as X_iY, where X represents the PS (P for PPcZn and R for RB), the subscript i represents the concentration of the PS (mM), and Y represents the polymer matrix (C for CA and E for EC). For example, a film composed of 1.3 mM PPcZn in CA would be a $P_{1.3}C$ film. We fabricated 4 different films: $P_{0.5}C$, $P_{1.3}C$, $P_{2.1}C$, and $R_{1.3}C$. All fabrication procedures were carried out in the dark. The thickness of each film ranged from 30 ± 5 μm. In all cases, optically clear films were obtained.

For the detection of $^1O_2$, CA and EC films containing DPBF were prepared using the same method described above. The solution of DPBF was then cast on the preformed self-disinfecting film to obtain an integrated film, as shown in the lower part of Figure 6-2. Using the molar mass of DPBF (270.33 g mol^{-1}) and the densities of CA and EC, the concentration of DPBF in the films was calculated to be 19.8 mM (DC, where D represents DPBF) and 16.9 mM (DE, where E represents EC). The integrated films were named according to the rule that the first layer was indicated before the second layer, the individual layers were defined with the letter representing the PS placed before the letter(s) for the polymer, and the subscript represents the concentration of the PS in the film. For example, films prepared by casting a DE solution on a $P_{1.3}C$ film were referred to as $P_{1.3}CDE$. Notably, a subscript is not used for the DPBF concentration in CA or EC because it does not vary as the PS concentration does. The DE film was prepared using THF as the solvent instead of acetone. The thickness of the double-layer films ranged from 60 ± 5 μm. The dried films were stored in foil laminate bags until required. The films tested in this study are listed in Table 6-1.

Table 6-1. Films fabricated for evaluation

Film name	1st layer		2nd layer	
	PS (mM)	Polymer	PS (mM)	Polymer
$P_{0.5}C$	PPcZn (0.5)	CA	none	
$P_{1.3}C$	PPcZn (1.3)	CA	none	
$P_{2.1}C$	PPcZn (2.1)	CA	none	
$R_{1.3}C$	RB (1.3)	CA	none	
$P_{1.3}CDE$	PPcZn (1.3)	CA	DPBF (16.9)	EC
$P_{1.3}CDC$	PPcZn (1.3)	CA	DPBF (19.8)	CA
$P_{2.1}CDE$	PPcZn (2.1)	CA	DPBF (16.9)	EC
$P_{0.5}CDE$	PPcZn (0.5)	CA	DPBF (16.9)	EC
$R_{1.3}CDE$	RB (1.3)	CA	DPBF (16.9)	EC

6.2.5 Detection of $^1O_2$ using DPBF

The generation of $^1O_2$ from the self-disinfecting surfaces was determined using integrated films, such as the $P_{1.3}CDE$ film. The test films were 20 mm × 40 mm in size. Figure 6-3 illustrates the integrated film sandwiched between plates of glass with no gap. The layered laminate was then irradiated from the upper side at 2000 lx using the F32W-T fluorescent light source. The absorbance level of the films was measured after 30, 60, 120, 300, and 600 s. Similarly, an experiment without a self-disinfecting surface film was conducted for comparison. All experiments were repeated more than three times.

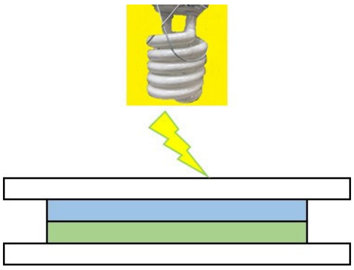

Figure 6-3. Cross-sectional illustration of $^1O_2$ detection during irradiation with visible light

6.2.6 Durability tests of self-disinfecting surfaces

The durability of the films as self-disinfecting surfaces was evaluated by performing a water-resistance test and an indoor exposure test. The water-resistance test involved the immersion of the film sample (20 mm × 40 mm in size) in 50 mL of pure water in a 100 mL beaker. The absorbance was measured before and after stirring for 2 h in the dark, and the ratio was compared. The indoor exposure test involved the illumination of the film sample (50 mm × 50 mm in size) for six months in a laboratory with room lights at 610 lx (the lights were turned off at night). The absorptance of the film was measured before and after illumination, and the ratio was used to determine the photostability of PS in the film.

6.2.7 Antiviral activity of $P_{1.3}C$

Using *Bacteriophage Qβ* (NBRC 20012) as the test microorganism, antiviral activities of the $P_{1.3}C$ film and a CA film (the control) were assessed according to the Japanese Industrial Standard JIS R 1756 2020. A sterilized humidity control filter paper was placed on the bottom of a sterilized storage petri dish, an appropriate amount of sterilized water was added to the humidity control paper, and a U-shaped glass tube was placed on it. An ultraviolet-sterilized test piece (length: 50 ± 2 mm, width: 50 ± 2 mm, thickness: 30 ± 5 μm) was placed on a U-shaped glass tube, and 0.15 mL of the test bacteriophage solution was dropped onto the test piece. The bacteriophage solution was covered with a polyethylene film, and the moisturizing glass was placed on the petri dish. Light irradiation tests were performed immediately after inoculation with the test bacteriophage solution using the white fluorescent lamp (FL20SSW/18) as the light source, except for the control pieces. The experiment was performed for 4 h both in the dark and in visible light (1000 lx). After experiments, the test pieces were immediately washed with 10 mL of Soybean-Casein Digest Broth with Lecithin & Polysorbate 20 Medium (SCDLP), and the solution was diluted 10^0, 10^1, 10^2, and 10^3-fold. The diluted solution was added to a separately prepared plate on which *E. coli* was grown, incubated at 35 °C for 16 h, and the number of plaques formed was visually counted. All tests were carried out three times to obtain an average value.

6.3 Results and discussion

6.3.1 Aggregation behavior of PPcZn in the CA film

PS should be present in a nonaggregated state for self-disinfecting applications because aggregation induces fast, radiationless deactivation and inhibits $^1O_2$ generation [220, 225]. Generally, Pc exhibits a strong tendency to aggregate that derives oligomers in solution due to its extended π-conjugation [220, 225, 228, 229]. Additionally, tetra-*tert*-phthalocyanine has been reported to be present in an aggregated state in CA films [218]. The aggregation behavior was assessed using UV-Vis spectroscopy. As expected, the absorption spectra of P_iC films ($P_{0.5}C$, $P_{1.3}C$, and $P_{2.1}C$) showed a single sharp Q-band at λ_{max} 664 nm, which is typical of nonaggregated species (Figure 6-4a).

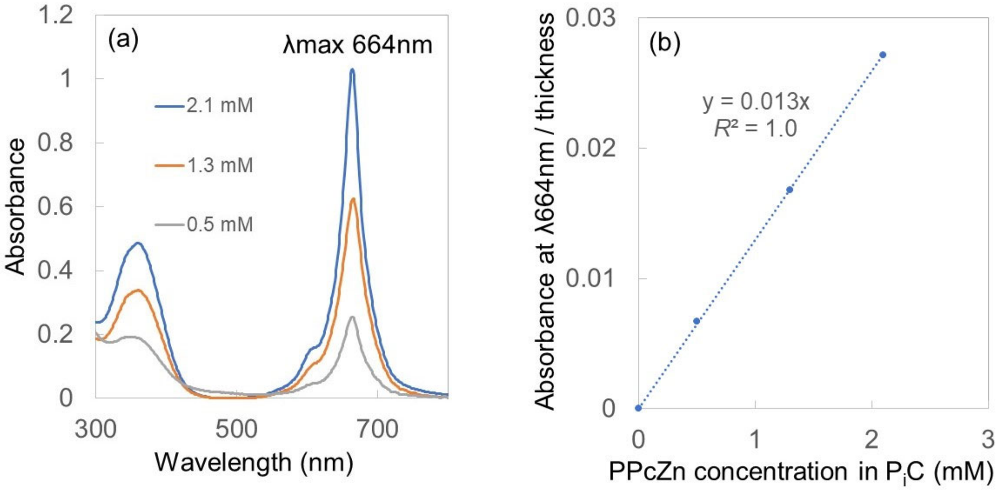

Figure 6-4. (a) UV-Vis absorption spectra of $P_{2.1}C$, $P_{1.3}C$, and $P_{0.5}C$; and (b) plot of the PPcZn concentration in the CA film versus absorbance at 664 nm

The aggregation behavior of PPcZn in the CA matrix was examined at different concentrations. Figure 6-4(b) shows that the appearance of the Q-band absorption maxima remained unchanged as the concentration increased. Furthermore, its apparent molar extinction coefficient remained almost constant, suggesting a purely monomeric form, which obeys the Beer–Lambert Law in the studied concentration range. PPcZn was confirmed to be uniformly dispersed in the CA film without aggregation, and the CA film containing PPcZn should be expected to generate $^1O_2$ upon visible light irradiation.

6.3.2 $^1O_2$ generation from CA films containing PSs upon visible light irradiation

The rate of $^1O_2$ formation is associated with a decrease in the absorbance of DPBF as a function of the irradiation time [178], and the reaction of DPBF with $^1O_2$ in solution has been reported to follow a pseudo-first-order kinetic model [221]. The change in the absorption spectrum of the $P_{1.3}CDE$ film irradiated with visible light is shown in Figure

6-5(a), and a dramatic reduction in absorption at 416 nm corresponding to DPBF absorption was observed.

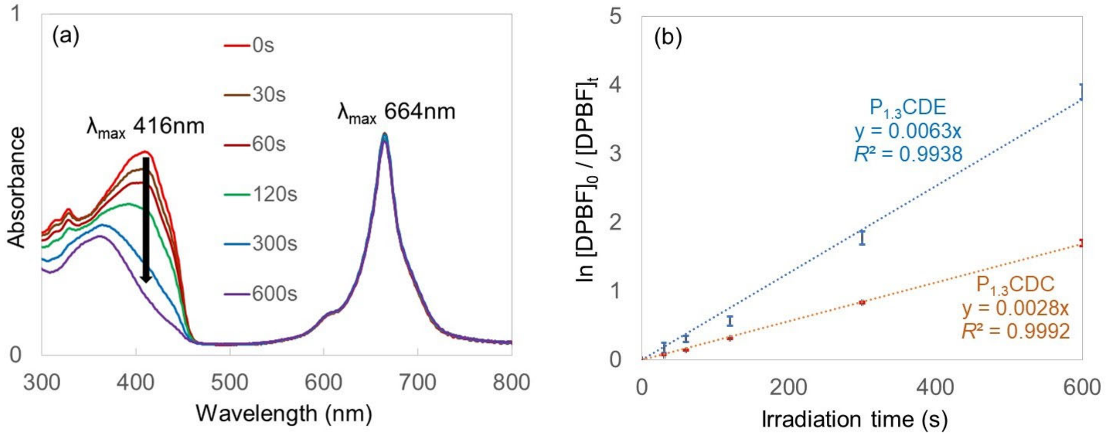

Figure 6-5. (a) Changes in the UV-Vis spectra of the $P_{1.3}$CDE film during irradiation and (b) time-dependent absorption intensity during irradiation reported as ln $[DPBF]_0/[DPBF]_t$

The degradation kinetics of DPBF by $^1O_2$ generated from $P_{1.3}$CDC and $P_{1.3}$CDE were determined by monitoring the photooxidation of DPBF. The degradation rate of DPBF, *k*, was determined by Equation 5-2 described in subsection 5.3.2. As shown in Figure 6-5(b), the reaction kinetics follow a pseudo-first-order rate law. This result suggests that the concentrations of oxygen and PS did not change during the experiment [186].

According to the results described in subsection 5.3.2, the DPBF photodegradation rates in DE and DC films that contained only DPBF as the PS were 0.0004 s^{-1} and 0.0002 s^{-1}, respectively. The degradation rates of DPBF in the $P_{1.3}$CDE and $P_{1.3}$CDC films were 0.0063 s^{-1} and 0.0028 s^{-1}, respectively. Thus, the $P_{1.3}$C film produced $^1O_2$ upon visible light irradiation, and the $^1O_2$ reacted with DPBF. Additionally, the rate of the reaction between $^1O_2$ and DPBF in the DC film was slower than that in the DE film because of the difference in oxygen permeability coefficients between the CA and EC films. The reaction rate of $^1O_2$ with DPBF has been reported to depend on the solvent [221], and a similar outcome is expected when a polymer film is used.

$P_{2.1}CDE$, $P_{0.5}CDE$, and $R_{1.3}CDE$ films were evaluated, and the results are shown in Figure 6-6. Interestingly, the rate of $^1O_2$ generation from the film depended on the concentration of PS. When the PS concentration in the film was increased 2.6 times (1.3 mM against 0.5 mM) and 4.2 times (2.1 mM against 0.5 mM), the rate of $^1O_2$ production increased 2.9 times (0.0067 s^{-1} against 0.0023 s^{-1}) and 4.5 times (0.0104 s^{-1} against 0.0023 s^{-1}), respectively.

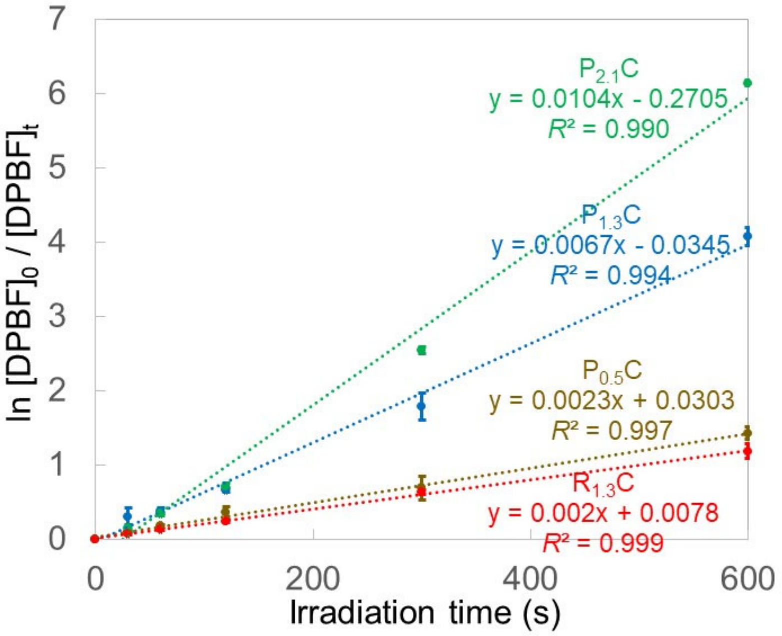

Figure 6-6. Comparison of the rate of $^1O_2$ generation upon the visible light irradiation of CA films containing RB and PPcZn at different concentrations

In this concentration range, the higher the concentration of PPcZn, the higher the amount of $^1O_2$ produced per unit time. The $P_{2.1}C$, $P_{1.3}C$, and $P_{0.5}C$ films reduced the initial concentration of DPBF almost completely (0.2% or less), to a large extent (2% or less), and by 24% at 600 s, respectively. $^1O_2$ was likely first generated at the interface with the

PS-containing film and diffused into the deeper region of the DE or DC film to reach the unreacted DPBE molecule. Additionally, at the same concentration, PPcZn produced more $^1O_2$ per unit time than RB. PPcZn is therefore expected to possess antiviral properties upon visible light irradiation.

6.3.3 Antiviral activity of the $P_{1.3}C$ film

The antiviral activity of the $P_{1.3}C$ film, a representative CA film containing PPcZn, was analyzed, and the test satisfied the requirements for validity as specified in JIS R 1756. As in subsection 5.3.1, log reduction was used to evaluate antiviral activity using the number of virus particles capable of forming plaques per unit volume in the dark and after irradiation with visible light. The number of visible plaques after irradiation and the number of visible plaques in the dark were counted, and the infection value (pfu/sample) was calculated based on the number of visible plaques.

After incubation under visible light, the antiviral activity of the $P_{1.3}C$ film increased compared with incubation in the dark (Table 6-2). This result indicates that the photodynamic effect on *Bacteriophage Qβ* was achieved with ordinary, daily light conditions (1000 lx). In an actual indoor environment, sunlight containing infrared light of 700 nm or more will be present, and a greater photoantiviral effect is expected based on the high durability of the $P_{1.3}C$ film, as described below.

Table 6-2 Antiviral activity of the $P_{1.3}C$ film compared to that of the blank film

Sample film	Log reduction
blank	0.0
$P_{1.3}C$	1.3

6.3.4 Durability of PC films compared to the RC film

The absorbance of the $R_{1.3}C$ film decreased to 84.3% compared to the film before immersion in water in the water-resistance test, which is likely due to the leaching of RB. Conversely, no leaching of PS was observed for any of the PPcZn-containing films in the UV-Vis spectra. This observation is likely because of the difference in the water solubility of PS.

The results of the indoor exposure test using the absorbance intensity ratio at 561 nm for the $R_{1.3}C$ film were 71.3% after only one day of exposure and 42.4% after seven days of exposure. The $P_{0.5}C$, $P_{1.3}C$, and $P_{2.1}C$ films had absorbance intensity ratios of 96.4%, 95.5%, and 98.5%, respectively, after six months of exposure at 664 nm. CA films containing PPcZn displayed a photobleaching degree of less than 5% even when incubated indoors under white light for six months. Additionally, the results of tensile tests on $P_{2.1}C$ films before and after six months of indoor exposure were performed 5 times for each sample and are summarized in Table 6-3.

Table 6-3 Tensile strength of $P_{2.1}C$ films before and after six months of indoor exposure.

Sample film	Tensile strength (MPa)
before exposure	72.0 ± 5.5
after six months exposure	73.0 ± 6.2

The data are presented as means ± standard deviations. These results suggest that the CA matrix containing PPcZn is a highly durable film both optically and physically.

The $^1O_2$ generation rates of the $P_{1.3}C$ films before and after exposure were compared by measuring the oxidation rate of DPBF by casting a DE solution onto each $P_{1.3}C$ film to confirm the lack of change in the $^1O_2$ production capacity of the PC film after six months of indoor exposure. As shown in Figure 6-7, the $P_{1.3}C$ film displayed a similar $^1O_2$ production rate before exposure and after six months of indoor exposure. The $P_{1.3}C$ film maintained the $^1O_2$ photogeneration efficiency over six months and was expected to maintain its antiviral effect. Furthermore, when comparing the transmittance of the $P_{1.3}C$ film with air in the visible light region (470 - 530 nm) in which PPcZn and CA have no absorption, the effect of exposure of the film for six months was investigated. The transmittance values both before and after exposure were >91%, confirming that the $P_{1.3}C$ film maintained its transparency for more than six months. These results prove that the CA film containing PPcZn exhibits excellent durability under indoor exposure conditions in terms of its function ($^1O_2$ generation ability with light irradiation), appearance (transparency and nonfading properties), and mechanical strength.

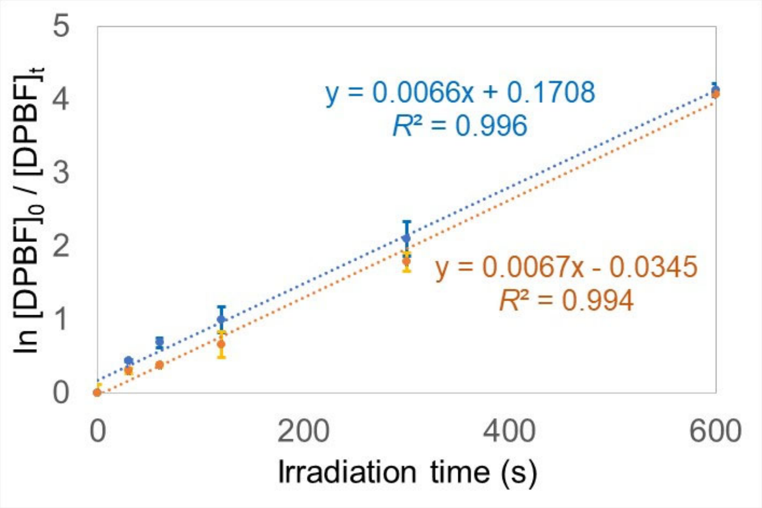

Figure 6-7. Comparison of $^1O_2$ production rates from the DE film before (orange) and after (blue) indoor exposure for six months

6.3.5 A representative applications of CA film containing PPcZn

The CA film containing PPcZn was used in origami to determine whether it has the appropriate strength and stiffness for practical applications. Figure 6-8 shows an example of a windmill that had the same appearance after one month and after six months of indoor exposure and was expected to exhibit antiviral function when placed in air flow. The self-sterilizing film obtained in this study has the potential to be used in indoor interior design or consumer-goods because it maintained its $^1O_2$ photogeneration ability for a long period while maintaining its transparency without fading and it could be manipulated without losing strength or stiffness.

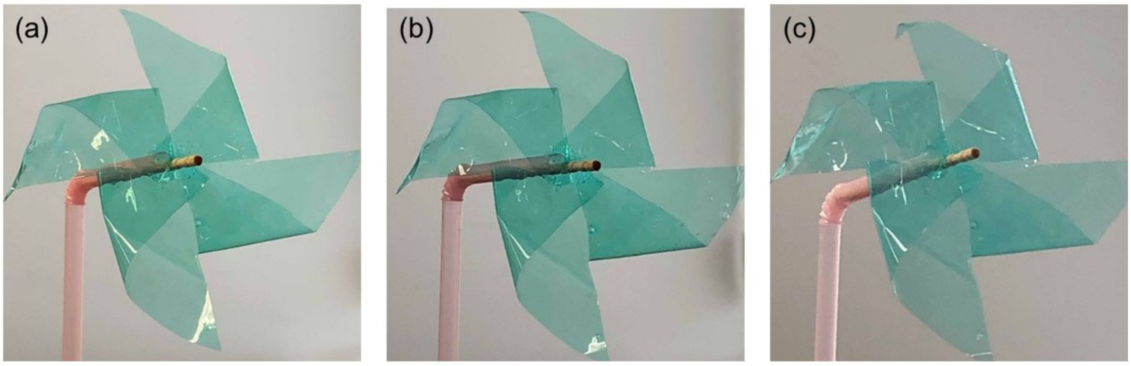

Figure 6-8. A picture of an "origami (windmill)" created with the $P_{1.3}C$ film. (a) Initial film (before exposure), (b) after one month of exposure, and (c) after six months of exposure

6.4 Conclusion

This chapter fabricated CA films containing PPcZn using a simple casting procedure. This phthalocyanine was successfully dispersed into CA films without aggregation, as confirmed by the fit to the Beer–Lambert law. Visible light illumination resulted in the photogeneration of $^1O_2$ from CA films containing PPcZn by CA and EC films containing DPBF. PPcZn in CA showed good photostability with no significant degradation over six months of continuous exposure to room light while maintaining its ability to generate $^1O_2$ with minimal degradation over time. We have shown that room light can serve as an economical and efficient light source for the photodynamic inactivation of viruses, and these data suggested that the photodynamic disinfection of the CA film containing PPcZn persists for over six months. These findings are promising for the implementation of this film as a self-disinfecting surface in real-world applications.

Concluding remarks

This thesis provides value-added sustainable polymers obtained from cellulose acetate and starch as representatives of polysaccharides. This research is based on the surveyed facts that the cost is important for the practical use of sustainable polymers. The strategies to realize sustainable practical materials are the usage inexpensive raw materials in waste-free process and the valorization of harmful waste materials.

This thesis composes of 6 chapters.

In chapter 1, water-swellable modified starch particles were obtained by simply mixing starch, urea, and phosphate followed by heating them in a particle state. Without washing process, they showed better plant-growing ability than commercially available petroleum-derived superabsorbent polymers (SAP).

In chapter 2, macroporous cellulose beads (MCBs), which have the same water absorption as the fluff-pulp used for disposable diapers, were fabricated in a single step from a cellulose acetate (CA) and from used cigarette filter (CF), respectively. The utilization of used CFs leads to the valorization of harmful waste materials.

In chapter 3, activated carbon (AC)-containing cellulosic porous beads (ACPBs) were prepared by extending the preparation method of MCBs. ACPB was evaluated using toluidine blue (TB) dye as a model adsorbate and could retain original shape and adsorption capacity after three times recycle of adsorption/desorption of TB. This method was applied to the fabrication of white activated carbon particles.

In chapter 4, cellulose-based SAP was obtained by applying the method described in chapter 1 to the cellulosic beads in chapter 2. The obtained cellulose-based SAP maintained the interconnected porous structure before processing. The cellulose-based SAP showed water absorption of approximately 50 g/g.

Coronavirus pandemic still poses a threat to humanity and the way to preventing the diffusion of the pandemic has been awaited.

In chapter 5, a film having antivirus function was prepared from a CA solution containing a photosensitizer (PS). Since CA has oxygen permeability, it was useful as a substrate for producing s singlet oxygen (${}^1O_2$) from oxygen. By using a film containing a detection probe of ${}^1O_2$, it was confirmed that ${}^1O_2$, which is effective in inactivating the virus, had effective to kill microbiol but no adverse effect on the human body.

In chapter 6, optically clear and durable film having inactivating function against virus was fabricated by incorporating phenoxy-substituted phthalocyanine zinc (PPcZn) into CA film and the antivirus effect was demonstrated.

In summary, this thesis demonstrated the method fabricating sustainable and practical materials under two efficient strategies. Hopefully, both the no-waste process and the valorization of harmful waste materials may become a standard for the development of the biomass-based sustainable products.

List of publications

Chapter 1

Energy-Efficient Preparation Method of Water-Swellable Starch Phosphate Carbamate Particles.

Nobuyuki Harada*, Yoshiro Mitsukami, and Hiroshi Uyama*

Starch **2021**, 73, 2000119.

DOI: 10.1002/star.202000119.

Chapter 2

Preparation of Macroporous Cellulose Beads through a Single-Step Non-Solvent Induced Phase Separation Method from a Cellulose Acetate Solution.

Nobuyuki Harada*, Jun-ichi Nakamura, and Hiroshi Uyama*

Bulletin of the Chemical Society of Japan **2019**, 92(9), 1444-1446.

DOI: 10.1246/bcsj.20190078.

Chapter 3

Single-step fabrication and environmental applications of activated carbon-containing porous cellulose beads.

Nobuyuki Harada*, Jun-ichi Nakamura, and Hiroshi Uyama*

Reactive and Functional Polymers **2021**, 160, 104830.

DOI: 10.1016/j.reactfunctpolym.2021.104830.

Chapter 4

Preparation and characterization of water-swellable hydrogel-forming porous cellulose beads.

Nobuyuki Harada*, Yoshiro Mitsukami, and Hiroshi Uyama*

Polymer **2021**, 215, 123381.

DOI: 10.1016/j.polymer.2021.123381.

Chapter 5

Penetration of Singlet Oxygen into Films with Oxygen Permeability Coefficient Close to that of Skin.

Nobuyuki Harada*, Mika Kataoka, Masahiro Nakanosho, and Hiroshi Uyama*

Photochem. Photobiol. **2021**, 97, 971.

DOI: 10.1111/php.13446.

Chapter 6

Fabrication and evaluation of durable, optically clear, and self-disinfecting films.

Nobuyuki Harada*, Kiyoshi Masuda, Jun-ichi Nakamura, and Hiroshi Uyama*

Polymer Journal **2021**, 53, 1383.

DOI: 10.1038/s41428-021-00532-9.

Acknowledgements

In compiling this doctoral thesis, first of all, I would like to express my sincere gratitude to Prof. Hiroshi Uyama for his continuous invaluable guidance and support.

I also would like to express my sincere appreciation to Prof. Akinori Saeki, Prof. Norimitsu Tohnai, Prof. Susumu Kuwabata, Prof. Takashi Hayashi, Prof. Nobuhito Imanaka, Prof. Ken-ichi Nakayama, Prof. Hidehiro Sakurai, Prof. Satoshi Minakata, Prof. Masaya Nogi, and Prof. Takahiro Kozawa for taking the time to review this thesis and for giving me valuable opinions in spite of their busy schedule.

I would like to express my heartful appreciation to Dr. Jun-ichi Nakamura for his suggestions and help in conducting research on cellulose acetate-based products related to chapter 2, 3, and 6. I would like to show my highest respect to Dr. Yoshiro Mitsukami for his cooperation and advice in advancing the research on bio-superabsorbent polymers related to Chapters 1 and 4. I would like to express my heartful thanks to Mr. Masahiro Nakanosho and Ms. Mika Kataoka for the corporation with rich knowledge and experience on the research of chapter 5. I would like to express my heartful appreciations to Mr. Kiyoshi Masuda for giving me valuable guidance and supplying dyes-related samples on Chapter 6.

I would like to express my deep thanks to president, Yujiro Goto and managing executive officer, Yasutaka Sumida for giving me this opportunity to compile this research treatise.

Finally, I would like to express my sincere thanks to all the members of Nippon Shokubai Research Alliance Laboratories and Nippon Shokubai Co., Ltd. for their cooperation in carrying out this research and compiling this thesis.

References

[1] R. Mülhaupt, Bioinspired Macromolecular Chemistry-Paying Tribute to the Pioneering Advances of Hermann Staudinger and Helmut Ringsdorf, *Macromolecular Chemistry and Physics* **2010**, 211(2), 121-126.

[2] R. Mülhaupt, Green Polymer Chemistry and Bio-based Plastics: Dreams and Reality, *Macromolecular Chemistry and Physics* **2013**, 214(2), 159-174.

[3] R.C. Thompson, C.J. Moore, F.S. vom Saal, S.H. Swan, Plastics, the environment and human health: current consensus and future trends, *Philos Trans R Soc Lond B Biol Sci* **2009**, 364(1526), 2153-66.

[4] Available on line: https://www.european-bioplastics.org/

[5] S. Venkatarajan, A. Athijayamani, An overview on natural cellulose fiber reinforced polymer composites, *Materials Today: Proceedings* **2021**, 37, 3620-3624.

[6] W. A. Laftah, Starch Based Biodegradable Blends: A Review, *International J. Engineering & technology* **2017**, 6, 1151.

[7] T. Niranjana Prabhu, K. Prashantha, A review on present status and future challenges of starch based polymer films and their composites in food packaging applications, *Polymer Composites* **2018**, 39(7), 2499-2522.

[8] M. Lemoigne, Products of dehydration and of polymerization of β-hydroxybutyric acid, *Bull. Soc. Chim. Biol.* **1926**, 8, 770-782.

[9] G.Q. Chen, A microbial polyhydroxyalkanoates (PHA) based bio- and materials industry, *Chem Soc Rev* **2009**, 38(8), 2434-46.

[10] M. Iguchi, S. Yamanaka, A. Budhiono, Bacterial cellulose - a masterpiece of Nature's arts, *J. Mater. Sci.* **2000**, 35(2), 261-270.

[11] G.-Q. Chen, X.-Y. Chen, F.-Q. Wu, J.-C. Chen, Polyhydroxyalkanoates (PHA) toward cost competitiveness and functionality, *Advanced Industrial and Engineering Polymer Research* **2020**, 3(1), 1-7.

[12] V. Siracusa, I. Blanco, Bio-Polyethylene (Bio-PE), Bio-Polypropylene (Bio-PP) and Bio-Poly(ethylene terephthalate) (Bio-PET): Recent Developments in Bio-Based Polymers Analogous to Petroleum-Derived Ones for Packaging and Engineering Applications, *Polymers (Basel)* **2020**, 12(8), 1641.

[13] J.-B. Zeng, K.-A. Li, A.-K. Du, Compatibilization strategies in poly(lactic acid)-based blends, *RSC Advances* **2015**, 5(41), 32546-32565.

[14] K. Okano, T. Tanaka, C. Ogino, H. Fukuda, A. Kondo, Biotechnological production of enantiomeric pure lactic acid from renewable resources: recent achievements, perspectives, and limits, *Appl Microbiol Biotechnol* **2010**, 85(3), 413-23.

[15] W. Deng, L. Yan, B. Wang, Q. Zhang, H. Song, S. Wang, Q. Zhang, Y. Wang, Efficient Catalysts for the Green Synthesis of Adipic Acid from Biomass, *Angew Chem Int Ed Engl* **2021**, 60(9), 4712-4719.

[16] Y. Tachibana, S. Kimura, K. Kasuya, Synthesis and verification of biobased terephthalic acid from furfural, *Sci Rep* **2015**, 5, 8249.

[17] Available online: https://www.shokubai.co.jp/ja/news/news0484.html.

[18] T. Vaisanen, A. Haapala, R. Lappalainen, L. Tomppo, Utilization of agricultural and forest industry waste and residues in natural fiber-polymer composites: A review, *Waste Manag* **2016**, 54, 62-73.

[19] R. L. Shogren, G. F. Fanta, W. M. Doane, Development of starch-based plastics - a reexamination of selected polymer systems in historical perspective, *Starch/Staerke* **1993**, 45(8), 276-80.

[20] S. Khoramnejadian, J.J. Zavareh, S. Khoramnejadian, Bio-based plastic a way for reduce municipal solid waste, *Procedia Engineering* **2011**, 21, 489-495.

[21] R. Soni, T.A. Asoh, H. Uyama, Cellulose nanofiber reinforced starch membrane with high mechanical strength and durability in water, *Carbohydr Polym* **2020**, 238, 116203.

[22] M.S. Rahman, M.S. Hasan, A.S. Nitai, S. Nam, A.K. Karmakar, M.S. Ahsan, M.J.A. Shiddiky, M.B. Ahmed, Recent Developments of Carboxymethyl Cellulose, *Polymers (Basel)* **2021**, 13(8), 1345.

[23] R.G. Candido, A.R. Goncalves, Synthesis of cellulose acetate and carboxymethylcellulose from sugarcane straw, *Carbohydr Polym* **2016**, 152, 679-686.

[24] S.W. Pattinson, A.J. Hart, Additive Manufacturing of Cellulosic Materials with Robust Mechanics and Antimicrobial Functionality, *Advanced Materials Technologies* **2017**, 2(4), 1600084.

[25] R. Battisti, E. Hafemann, C.A. Claumann, R.A.F. Machado, C. Marangoni, Synthesis and characterization of cellulose acetate from royal palm tree agroindustrial waste, *Polymer Engineering & Science* **2018**, 59(5), 891-898.

[26] M. Volanti, D. Cespi, F. Passarini, E. Neri, F. Cavani, P. Mizsey, D. Fozer, Terephthalic acid from renewable sources: early-stage sustainability analysis of a bio-PET precursor, *Green Chemistry* **2019**, 21(4), 885-896.

[27] A.L. Roder Green, A. Putschew, T. Nehls, Littered cigarette butts as a source of nicotine in urban waters, *Journal of Hydrology* **2014**, 519, 3466-3474.

[28] J. Assres, B. Abate, Reprocessing Waste Cigarette Butts into Usable Materials, *Int. J. Textile Eng. Process.* **2018**, 4(3), 6-11.

[29] D. Korneev, O. Kurskaya, K. Sharshov, J. Eastwood, M. Strakhovskaya, Ultrastructural Aspects of Photodynamic Inactivation of Highly Pathogenic Avian H5N8 Influenza Virus, *Viruses* **2019**, 11(10), 955.

[30] J. Lee, S. Park, H.G. Roh, S. Oh, S. Kim, M. Kim, D. Kim, J. Park, Preparation and Characterization of Superabsorbent Polymers Based on Starch Aldehydes and Carboxymethyl Cellulose, *Polymers (Basel)* **2018**, 10(6), 605.

[31] T. Sato, T. Tanaka, H. Nishiofuku, Y. Fukuoka, T. Masada, S. Tatsumoto, N. Marugami, K. Morita, C. Obayashi, S. Hori, M. Kaneko, A. Kijima, K. Kichikawa,

Superabsorbent Polymer Microspheres Prepared with Hypertonic Saline to Reduce Microsphere Expansion, *Cardiovasc Intervent Radiol* **2018**, 41(9), 1412-1418.

[32] M.N. Alam, M.S. Islam, L.P. Christopher, Sustainable Production of Cellulose-Based Hydrogels with Superb Absorbing Potential in Physiological Saline, *ACS Omega* **2019**, 4(5), 9419-9426.

[33] M. O. Weaver, R. R. Montgomery, L. D. Miller, V. E. Sohns, G. F. Franta, W. M. Doane, A Practical Process for the Preparation of Super Slurper, a Starch-Based Polymer with a Large Capacity to Absorb Water, *Starch/Stärke* **1977**, 29, 413.

[34] M. Sadeghi, M. Yarahmadi, Swelling Kinetics Study of Hydrolyzed Starch-poly Acrylonitrile Superabsorbent Hydrogel with Salt-sensitivity Properties, *Asian J.Chem.* **2011**, 23, 5225-5228.

[35] M. D. Lechner, W. Lazik, Super slurpers from renewable resources: synyhesis, properties, applications, *Hem. Ind*. **2001**, 55, 477-481.

[36] K. Sangseethong, P. Chatakanonda, K. Sriroth, Superabsorbent Hydrogels From Rice Starches With Different Amylose Contents, *Starch/Stärke* **2018**, 70(11-12), 1700244.

[37] W. M. Kulicke, Y. A. Aggour, H. Nottelmann, M. Z. Elsabee, Swelling and Rheological Studies of Some Starch Hydrogels, *Starch/Stärke* **1989**, 41, 140.

[38] L. Passauer, F. Liebner, K. Fischer, Starch Phosphate Hydrogels. Part I: Synthesis by Mono-phosphorylation and Cross-linking of Starch, *Starch/Staerke* **2009**, 61(11), 621-627.

[39] W. Xie, L. Shao, Phosphorylation of Corn Starch in an Ionic Liquid, *Starch/Stärke* **2009**, 61(12), 702-708.

[40] M. I. Khalil, S. Farag, K. M. Mostafa, Some Studies on Starch Carbamate, *Starch/Stärke* **1994**, 46, 312.

[41] V. H. Kessel, Bestimmung der funktionellen Carbamoyl-gruppe in Carbamatstärken und Carbamatphosphatstärken, *Starch/Stärke* **1987**, 39, 57.

[42] M. I. Khalil, S. Farag, A. A. Aly, A. Hebeish, Some studies on starch-urea-acid reaction mechanism, *Carbohydrate Polymers* **2002**, 48, 255.

[43] U. Heinze, D. Klemm, E. Unger, F. Pieschel, New Starch Phosphate Carbamides of High Swelling Ability: Synthesis and Characterization, *Starch/Stärke* **2003**, 55, 55–60.

[44] F. Pieschel, E. Lange, J. Camacho, German Patent DE 19859123 C1, **2000**.

[45] F. Pieschel, E. Lange, J. Camacho, U. S. Patent 6,703,296 B1, **2004**.

[46] L. Guo, S. Zhang, B. Ju, J. Yang, Study on adsorption of Cu (II) by water-insoluble starch phosphate carbamate, *Carbohydr. Polym.* **2006**, 63, 487.

[47] L. Passauer, Thermal characterization of ammonium starch phosphate carbamates for potential applications as bio-based flame-retardants, *Carbohydr Polym* **2019**, 211, 69-74.

[48] G. Lewandowicz, J. Fornal, A. Walkowski, M. Maczynski, G. Urbaniak, G. Szymariska, Starch esters obtained by microwave radiation — structure and functionality, *Ind. Crops Prod.* **2000**, 11, 249.

[49] H.-P. Rensch, B. Riedl, An Infrared Spectroscopic Study of Chemically Modified Chemithermomechanical Pulp, *Journal of Wood Chemistry and Technology* **2006**, 13(2), 167-186.

[50] D.L. Frasco, Infrared Spectra of Ammonium Carbamate and Deuteroammonium Carbamate, *The Journal of Chemical Physics* **1964**, 41(7), 2134-2140.

[51] W.-R. Wang, A. Li, W. Mei, R.-R. Zhu, K. Li, X.-Y. Sun, Y.-C. Qian, S.-L. Wang, Dexamethasone sodium phosphate intercalated layered double hydroxides and their therapeutic efficacy in a murine asthma model, *RSC Advances* **2015**, 5(30), 23826-23834.

[52] D.M. Suflet, G.C. Chitanu, V.I. Popa, Phosphorylation of polysaccharides: New results on synthesis and characterisation of phosphorylated cellulose, *Reactive and Functional Polymers* **2006**, 66(11), 1240-1249.

[53] E. Kochkina, N. D. Lukin, Mono-starch phosphate/montmorillonite nanocomposites prepared by vibration milling: structure and adsorption capacity towards methylene blue dye, *Cellul. Chem. Technol.* **2019**, 53, 133.

[54] G. F. Touzinsky, S. H. Gordon, Degree of substitution of cellulose derivatives containing n different substituent groups*, Carbohydr. Res. **1979**, 69, 327.

[55] L. Passauer, H. Bender, Functional group analysis of starches reacted with urea-phosphoric acid-Correlation of wet chemical measures with FT Raman spectroscopy, Carbohydr Polym **2017**, 168, 356-364.

[56] D. C. Roe, U. S. Patent 5,422,169, **1995**.

[57] N. Herfert, M. M. Azad, G. T. Woodrum, U. S. Patent 2008/0045916 A1, **2008**.

[58] H.S. Elshafie, I. Camele, Applications of Absorbent Polymers for Sustainable Plant Protection and Crop Yield, *Sustainability* **2021**, 13(6), 3253.

[59] N. R. Cameron, D. C. Sherrington, Synthesis and Characterization of Poly(aryl ether sulfone) PolyHIPE Materials, *Macromolecules* **1997**, 30, 5860.

[60] H. Inoue, K. Yamanaka, A. Yoshida, A. Nakamura, T. Aoki, M. Teraguchi, T. Kaneko, Specific Ion Exchange Properties of a New Porous Ion Exchange Resin Having an Open-celled Monolith Structure, *Kobunshi Ronbunshu* **2005**, 62, 7.

[61] K. Haibach, A. Menner, R. Powell, A. Bismarck, Tailoring mechanical properties of highly porous polymer foams: Silica particle reinforced polymer foams via emulsion templating, *Polymer* **2006**, 47(13), 4513-4519.

[62] Y. Xin, T. Fujimoto, H. Uyama, Facile fabrication of polycarbonate monolith by non-solvent induced phase separation method, *Polymer* **2012**, 53(14), 2847-2853.

[63] X. Sun, H. Uyama, In situ mineralization of hydroxyapatite on poly(vinyl alcohol) monolithic scaffolds for tissue engineering, *Colloid and Polymer Science* **2014**, 292(5), 1073-1078.

[64] X. Sun, G. Sun, X. Wang, Morphology modeling for polymer monolith obtained by non-solvent-induced phase separation, *Polymer* **2017**, 108, 432-441.

[65] Y. Xin, J. Sakamoto, A.J. van der Vlies, U. Hasegawa, H. Uyama, Phase separation approach to a reactive polycarbonate monolith for "click" modifications, *Polymer* **2015**, 66, 52-57.

[66] Y. Xin, Q. Xiong, Q. Bai, M. Miyamoto, C. Li, Y. Shen, H. Uyama, A hierarchically porous cellulose monolith: A template-free fabricated, morphology-tunable, and easily functionalizable platform, *Carbohydr Polym* **2017**, 157, 429-437.

[67] Q. Xiong, Q. Bai, C. Li, Y. He, Y. Shen, H. Uyama, A cellulose acetate/Amygdalus pedunculata shell-derived activated carbon composite monolith for phenol adsorption, *RSC Advances* **2018**, 8(14), 7599-7605.

[68] Z. Yang, T.-A. Asoh, H. Uyama, Cationic functionalization of cellulose monoliths using a urea-choline based deep eutectic solvent and their applications, *Polymer Degradation and Stability* **2019**, 160, 126-135.

[69] L. F. Chen, G. T. Tsao, Physical Characteristics of Porous Cellulose Beads as Supporting Material for Immobilized Enzymes, *Biotechnol. Bioeng.* **1976**, 18, 1507.

[70] A. Sachse, N. Linares, P. Barbaro, F. Fajula, A. Galarneau, Selective hydrogenation over Pd nanoparticles supported on a pore-flow-through silica monolith microreactor with hierarchical porosity, *Dalton Trans* **2013**, 42(5), 1378-84.

[71] S.R. Dods, O. Hardick, B. Stevens, D.G. Bracewell, Fabricating electrospun cellulose nanofibre adsorbents for ion-exchange chromatography, *J Chromatogr A* **2015**, 1376, 74-83.

[72] V. Smrekar, F. Smrekar, A. Strancar, A. Podgornik, Single step plasmid DNA purification using methacrylate monolith bearing combination of ion-exchange and hydrophobic groups, *J Chromatogr A* **2013**, 1276, 58-64.

[73] X. Fu, T. Maruyama, T. Sotani, H. Matsuyama, Effect of surface morphology on membrane fouling by humic acid with the use of cellulose acetate butyrate hollow fiber membranes, *Journal of Membrane Science* **2008**, 320(1-2), 483-491.

[74] H. Matsuyama, M. Teramoto, T. Uesaka, M. Goto, F. Nakashio, Kinetics of droplet growth in the metastable region in cellulose acetate/acetone/nonsolvent system, *J. Membr. Sci.* **1999**, 152, 227.

[75] K.F. Du, M. Yan, Q.Y. Wang, H. Song, Preparation and characterization of novel macroporous cellulose beads regenerated from ionic liquid for fast chromatography, *J Chromatogr A* **2010**, 1217(8), 1298-304.

[76] E. Yildir, R. Kolakovic, N. Genina, J. Trygg, M. Gericke, L. Hanski, H. Ehlers, J. Rantanen, M. Tenho, P. Vuorela, P. Fardim, N. Sandler, Tailored beads made of dissolved cellulose--investigation of their drug release properties, *Int J Pharm* **2013**, 456(2), 417-23.

[77] W. Xie, T. Li, C. Chen, H. Wu, S. Liang, H. Chang, B. Liu, E. Drioli, Q. Wang, J.C. Crittenden, Using the Green Solvent Dimethyl Sulfoxide To Replace Traditional Solvents Partly and Fabricating PVC/PVC-g-PEGMA Blended Ultrafiltration Membranes with High Permeability and Rejection, *Industrial & Engineering Chemistry Research* **2019**, 58(16), 6413-6423.

[78] H. Matsuyama, Structure Control of Porous Membrane Prepared by Thermally Induced Phase Separation, *Membrane* **2001**, 26, 116.

[79] Y. Yamashita, T. Endo, Deterioration Behavior of Cellulose Acetate Films in Acidic or Basic Aqueous Solutions, *J. Appl. Polym. Sci.* **2004**, 91, 3354-3361.

[80] A. J. Reuvers, F. W. Altena, C. A. Smolders, Demixing and Gelation Behavior of Ternary Cellulose Acetate Solutions, *J. Polym. Sci., Part B: Polym. Phys.* **1986**, 24, 793-804.

[81] D. Ciolacu, F. Ciolacu, V. Popa, Amorphous cellulose - structure and characterization, *Cellul. Chem. Technol.* **2011**, 45, 13-21.

[82] Available online: http://www.env. go.jp/recycle/recycling/diapers.

[83] N.F. Cardoso, E.C. Lima, I.S. Pinto, C.V. Amavisca, B. Royer, R.B. Pinto, W.S. Alencar, S.F. Pereira, Application of cupuassu shell as biosorbent for the removal of textile dyes from aqueous solution, *J Environ Manage* **2011**, 92(4), 1237-47.

[84] H. Ali, C.V. Silva, B. Royer, G. Rodrigues Filho, D.A. Cerqueira, R.M.N. Assuncao, Chemically Modified Polyvinyl Chloride for Removal of Thionine Dye (Lauth's Violet), *Materials (Basel)* **2017**, 10(11), 1297.

[85] D. Ozer, G. Dursun, A. Ozer, Methylene blue adsorption from aqueous solution by dehydrated peanut hull, *J Hazard Mater* **2007**, 144(1-2), 171-179.

[86] M. Rafatullah, O. Sulaiman, R. Hashim, A. Ahmad, Adsorption of methylene blue on low-cost adsorbents: a review, *J Hazard Mater* **2010**, 177(1-3), 70-80.

[87] L. Zápotocký, M. Šváb, Removal of ammonia emissions from waste air in a biotrickling filter: pilot-scale demonstration in real conditions, *Open Chemistry* **2012**, 10(4), 1049-1058.

[88] C.-H. Tsai, W.-J. Lee, C.-Y. Chen, W.-T. Liao, Decomposition of CH3SH in a RF Plasma Reactor: Reaction Products and Mechanisms, *Industrial & Engineering Chemistry Research* **2001**, 40(11), 2384-2395.

[89] M. Sadiq, M. Khan, R. Aman, S. Sadiq, M. Sohail Ahmad, M. Ali, R. Ali, Thermodynamic and kinetic studies of adsorptive removal of toluidine blue by activated carbon from olive pit, *Desalination and Water Treatment* **2017**, 78, 292-299.

[90] M. Danish, T. Ahmad, W.N.A.W. Nadhari, M. Ahmad, W.A. Khanday, L. Ziyang, Z. Pin, Optimization of banana trunk-activated carbon production for methylene blue-contaminated water treatment, *Applied Water Science* **2018**, 8(1). DOI: 10.1007/s13201-018-0644-7.

[91] S. Khorvash, S. Behnam, Removal of methylene blue dye by immobilized mixture of brown alga Dictyota cervicornis and activated carbon, *Desalination and Water Treatment* **2019**, 162, 383-390.

[92] Ü. Geçgel, B. Kocabıyık, O. Üner, Adsorptive Removal of Methylene Blue from Aqueous Solution by the Activated Carbon Obtained from the Fruit of Catalpa bignonioides, *Water, Air, & Soil Pollution* **2015**, 226(8). DOI: 10.1007/s11270-015-2513-4.

[93] X. Zhao, C. Huang, S. Zhang, C. Wang, Cellulose acetate/activated carbon composite membrane with effective dye adsorption performance, *J. Macromol. Sci. Phys.* **2019**, 58, 909–920.

[94] S. Moosavi, S. Gan, S. Zakaria, Functionalized cellulose beads with activated carbon, *Cellulose Chem. Technol.* **2019**, 53, 815–825.

[95] N. Somsesta, V. Sricharoenchaikul, D. Aht-Ong, Adsorption removal of methylene blue onto activated carbon/cellulose biocomposite films: Equilibrium and kinetic studies, *Materials Chemistry and Physics* **2020**, 240, 122221.

[96] Q. Bai, Q. Xiong, C. Li, Y. Shen, H. Uyama, Hierarchical porous cellulose/activated carbon composite monolith for efficient adsorption of dyes, *Cellulose* **2017**, 24(10), 4275-4289.

[97] N. Saeidi, M.N. Lotfollahi, A procedure to form powder activated carbon into activated carbon monolith, *Int. J. Adv. Manuf. Technol.* **2015**, 81(5-8), 1281-1288.

[98] S. Firstov, Yu. Pudrezov, Optimization of mechanical properties of porous materials, *Powder Metallurgy Progress* **2001**, 1 (1), 5–18.

[99] N. Harada, J.-i. Nakamura, H. Uyama, Preparation of Macroporous Cellulose Beads through a Single-Step Non-Solvent Induced Phase Separation Method from a Cellulose Acetate Solution, *Bull. Chem. Soc. Jpn.* **2019**, 92(9), 1444-1446.

[100] N.E. Chadi, S. Merouani, O. Hamdaoui, Characterization and application of a 1700-kHz acoustic cavitation field for water decontamination: a case study with toluidine blue, *Applied Water Science* **2018**, 8(6). DOI: 10.1007/s13201-018-0809-4.

[101] Y. Shimizu, J. Hayashi, A new method for cellulose acetylation with acetic acid, *Seni-Gakkaishi* **1988**, 44(9), 451–456.

[102] T.G.M. van de Ven, K. Saint-Cyr, M. Allix, Adsorption of toluidine blue on pulp fibers, *Colloids Surf. A Physicochem. Eng. Asp.* **2007**, 294(1-3), 1-7.

[103] R. Thimmaraju, N. Bhagyalakshmi, M.S. Narayan, G.A. Ravishankar, Kinetics of pigment release from hairy root cultures of Beta vulgaris under the influence of pH, sonication, temperature and oxygen stress, *Process Biochem.* **2003**, 38(7), 1047-1061.

[104] L. D'Ilario, A. Martinelli, Toluidine blue: aggregation properties and structural aspects, *Model. Simul. Mater. Sci. Eng.* **2006**, 14(4), 581-595.

[105] M.A. Rauf, S.B. Bukallah, F.A. Hamour, A.S. Nasir, Adsorption of dyes from aqueous solutions onto sand and their kinetic behavior, *Chem. Eng. J.* **2008**, 137(2), 238-243.

[106] L. Guo, G. Li, J. Liu, S. Ma, J. Zhang, Kinetic and Equilibrium Studies on Adsorptive Removal of Toluidine Blue by Water-Insoluble Starch Sulfate, *J. Chem. Eng. Data* **2011**, 56(5), 1875-1881.

[107] M.A. Rauf, S.M. Qadri, S. Ashraf, K.M. Al-Mansoori, Adsorption studies of Toluidine Blue from aqueous solutions onto gypsum, *Chem. Eng. J.* **2009**, 150(1), 90-95.

[108] W. Chen, Q. Li, Y. Wang, X. Yi, J. Zeng, H. Yu, Y. Liu, J. Li, Comparative study of aerogels obtained from differently prepared nanocellulose fibers, *ChemSusChem* **2014**, 7(1), 154-61.

[109] F. Ali, Adsorption of toluidine blue dye from industrial waste water on the remnants of tea leaf, *Int. J. ChemTech Res.* **2017**, 10, 497–506.

[110] B.H. Hameed, A.T. Din, A.L. Ahmad, Adsorption of methylene blue onto bamboo-based activated carbon: kinetics and equilibrium studies, *J Hazard Mater* **2007**, 141(3), 819-25.

[111] S. Wonorahardjo, M.S. Ibnu, E. Budiasih, Sulfur dioxide and ammonia gas reduction using coconut cellulose and acetylated cellulose, *Chem. Chem. Eng. Biotech. Food Ind.* **2016**, 17, 179.

[112] S. Sornkamnerd, M.K. Okajima, T. Kaneko, Tough and Porous Hydrogels Prepared by Simple Lyophilization of LC Gels, *ACS Omega* **2017**, 2(8), 5304-5314.

[113] S. Woerly, Porous Hydrogels for Neural Tissue Engineering, *Materials Science Forum* **1997**, 250, 53-68.

[114] A. Suyantohadi, T. Kyoren, M. Hariadi, M.H. Purnomo, T. Morimoto, Effect of high consentrated dissolved oxygen on the plant growth in a deep hydroponic culture under a low temperature, *IFAC Proceedings* **2010**, 43(26), 251-255.

[115] M. Beaumont, S. Rosenfeldt, B.L. Tardy, C. Gusenbauer, A. Khakalo, Nonappa, M. Opietnik, A. Potthast, O.J. Rojas, T. Rosenau, Soft cellulose II nanospheres: sol-gel behaviour, swelling and material synthesis, *Nanoscale* **2019**, 11(38), 17773-17781.

[116] R. Ajdary, B.L. Tardy, B.D. Mattos, L. Bai, O.J. Rojas, Plant Nanomaterials and Inspiration from Nature: Water Interactions and Hierarchically Structured Hydrogels, *Adv. Mater.* **2020**, 33(28), e2001085.

[117] O. Petrauskaite, S. Gomes Pde, M.H. Fernandes, G. Juodzbalys, A. Stumbras, J. Maminskas, J. Liesiene, M. Cicciu, Biomimetic mineralization on a macroporous cellulose-based matrix for bone regeneration, *Biomed Res. Int.* **2013,** 452750.

[118] H. Gu, Z. Yue, S. Leong, B. Nugraha, L.P. Tan, Control of in vitro neural differentiation of mesenchymal stem cells in 3D macroporous, cellulosic hydrogels, *Regen. Med.* **2010**, 5, 245–253.

[119] S. Liu, M. Jin, Y. Chen, H. Gao, X. Shi, W. Cheng, L. Ren, Y. Wang, High internal phase emulsions stabilised by supramolecular cellulose nanocrystals and their application as cell-adhesive macroporous hydrogel monoliths, *J Mater Chem B* **2017**, 5(14), 2671-2678.

[120] X.-F. Sun, Z. Gan, Z. Jing, H. Wang, D. Wang, Y. Jin, Adsorption of methylene blue on hemicellulose-based stimuli-responsive porous hydrogel, *J. Appl. Polym. Sci.* **2015**, 132 (10), 41606.

[121] B.J. Kong, A. Kim, S.N. Park, Properties and in vitro drug release of hyaluronic acid-hydroxyethyl cellulose hydrogels for transdermal delivery of isoliquiritigenin, *Carbohydr Polym* **2016**,147, 473-481.

[122] S.F. Plappert, F.W. Liebner, J. Konnerth, J.M. Nedelec, Anisotropic nanocellulose gel-membranes for drug delivery: Tailoring structure and interface by sequential periodate-chlorite oxidation, *Carbohydr Polym* **2019**, 226, 115306.

[123] L. Zolghadr, B.V. Farahani, H. Ghasemzadeh, N. Javadi, Physicochemical studies of closed loop insulin delivery system based on intelligent carboxymethyl cellulose hydrogel, *Indian J. Biochem. Biophys.* **2019**, 56, 125-131.

[124] A. Sannio, G. Mensitieri, L. Nicolais, Water and synthetic urine sorption capacity of cellulose-based hydrogels under a compressive stress field, *J. Appl. Polym. Sci.* **2004**, 91, 3791–3796.

[125] D. Rusu, D. Ciolacu, B. Simionescu, Cellulose-based hydrogels in tissue engineering applications, *Cellul. Chem. Technol.* **2019**, 53, 907–923.

[126] Z.T. Xie, T.A. Asoh, Y. Uetake, H. Sakurai, H. Uyama, Dual roles of cellulose monolith in the continuous-flow generation and support of gold nanoparticles for green catalyst, *Carbohydr Polym* **2020**, 247, 116723.

[127] R. Castel, A. Richard, R. Audebert, Swelling of anionic and cationic starch-based superabsorbents in water and saline solution, *J. Appl. Polym. Sci.* **1990**, 39, 11–29.

[128] A.C. Nuessle, F.M. Ford, W.P. Hall, A.L. Lippert, Some aspects of the cellulose phosphate-urea reaction, *Textil. Res. J.* **1956**, 26, 32–39.

[129] B.G. Fiss, L. Hatherly, R.S. Stein, T. Friščić, A. Moores, Mechanochemical Phosphorylation of Polymers and Synthesis of Flame-Retardant Cellulose Nanocrystals, *ACS Sustain. Chem. Eng.* **2019**, 7(8), 7951-7959.

[130] S. Gebke, K. Thummler, R. Sonnier, S. Tech, A. Wagenfuhr, S. Fischer, Flame Retardancy of Wood Fiber Materials Using Phosphorus-Modified Wheat Starch, *Molecules* **2020**, 25(2), 335.

[131] I. Nehls, F. Loth, 13C-NMR-spektroskopische Untersuchungen zur Phosphatierung von Celluloseprodukten im System H3PO4/Harnstoff, *Acta Polym.* **1991**, 42, 233–235.

[132] N.K. Yurkshtovich, T.L. Yurkshtovich, F.N. Kaputskii, N.V. Golub, R.I. Kosterova, Esterification of viscose fibers with orthophosphoric acid and study of their physicochemical and mechanical properties, *Fibre Chem.* **2007**, 39, 31–36.

[133] F. Fu, M. Xu, H. Wang, Y. Wang, H. Ge, J. Zhou, Improved Synthesis of Cellulose Carbamates with Minimum Urea Based on an Easy Scale-up Method, *ACS Sustain. Chem. Eng.* **2015**, 3(7), 1510–1517.

[134] Y. Guo, J. Zhou, Y. Song, L. Zhang, An efficient and environmentally friendly method for the synthesis of cellulose carbamate by microwave heating, *Macromol. Rapid Commun.* **2009**, 30(17), 1504–1508.

[135] W.G. Glassor, B.K. McCartney, G. Samaranayake, Cellulose derivatives with a low degree of substitution. 3. The biodegradability of cellulose esters using a simple enzyme assay, *Biotechnol. Prog.* **1994**, 10, 214–219.

[136] T.N. Blanton, J.A. Kaduk, Q. Johnson, X-ray diffraction characterization of a distorted Debye–Scherrer film strip – the effect of deacetylation on cellulose triacetate and an improved structural model for cellulose II, *Powder Diffraction* **2014**, 29(2), 108-112.

[137] Q. Li, Z. Zhou, D. Zhang, W. Cong, Deacidification of Microalgal Oil with Alkaline Microcrystalline Cellulose, *Appl. Biochem. Biotechnol.* **2021**, 193(4), 952-964.

[138] T. Hatakeyama, H. Kanetsuna, Thermal analysis of cellulose, *Kobunshi Kagaku* **1969**, 26, 76–82.

[139] D. Ruhr, M. John, A. Reiche, Determination of the effective degree of cross-linking of porous cellulose membranes cross-linked with bifunctional epoxides, *Carbohydr Polym* **2021**, 251, 117043.

[140] T. Hirata, T. Nishimoto, DSC, DTA, and TG of cellulose untreated and treated with flame-retardants, *Thermochim. Acta* **1991**, 193, 99–106.

[141] S.R. Labafzadeh, J.S. Kavakka, K. Vyavaharkar, K. Sievänen, I. Kilpeläinen, Preparation of cellulose and pulp carbamates through a reactive dissolution approach, *RSC Advances* **2014**, 4(43), 22434.

[142] A. Sdrobis, G.E. Ioanid, C.D. Varganici, C. Vasile, Dual responsive modified cellulose/chitin mixed fibers, *Cellul. Chem. Technol.* **2015**, 49, 281–289.

[143] H. Schott, Swelling kinetics of polymers, *J. Macromol. Sci.* **1992**, B31(1), 1–9.

[144] C. Jin, W. Song, T. Liu, J. Xin, W.C. Hiscox, J. Zhang, G. Liu, Z. Kong, Temperature and pH Responsive Hydrogels Using Methacrylated Lignosulfonate Cross-Linker: Synthesis, Characterization, and Properties, *ACS Sustain. Chem. Eng.* **2018**, 6(2), 1763-1771.

[145] H. El-Hamshary, Synthesis and water sorption studies of pH sensitive poly(acrylamide-co-itaconic acid) hydrogels, *Eur. Polym. J.* **2007**, 43(11), 4830–4838.

[146] K. Syverud, S.R. Pettersen, K. Draget, G. Chinga-Carrasco, Controlling the elastic modulus of cellulose nanofibril hydrogels—scaffolds with potential in tissue engineering, *Cellulose* **2014**, 22(1), 473-481.

[147] S.K. Raj, A.B. Raj, Seed priming: An approach towards agricultural sustainability, *Journal of Applied and Natural Science* **2019**, 11(1), 227-234.

[148] K. Njira, A review of effects of nutrient elements on crop quality, *Afr. J. Food Agric. Nutrit. Develop.* **2015**, 15, 9777–9793.

[149] E. Bontempi, The europe second wave of COVID-19 infection and the Italy "strange" situation, *Environ. Res.* **2021**, 193, 110476.

[150] S. Noimark, E. Salvadori, R. Gomez-Bombarelli, A.J. MacRobert, I.P. Parkin, C.W. Kay, Comparative study of singlet oxygen production by photosensitiser dyes encapsulated in silicone: towards rational design of anti-microbial surfaces, *Phys. Chem. Chem. Phys.* **2016**,18(40), 28101-28109.

[151] J.M. Boyce, Modern technologies for improving cleaning and disinfection of environmental surfaces in hospitals, *Antimicrob Resist. Infect. Control* **2016**, 5, 10.

[152] M. Schafer, C. Schmitz, R. Facius, G. Homeck, B. Milow, K. H. Funken, J. Ortner, Systematic study of parameters influencing the action of rose Bengal with visible light on bacterial cells: Comparison between the biological effect and singlet-oxygen production, *Photochem. Photobiol.* **2000**, 71, 514.

[153] C.A. Morton, K.E. McKenna, L.E. Rhodes, G. British Association of Dermatologists Therapy, S. Audit, G. the British Photodermatology, Guidelines for topical photodynamic therapy: update, *Br. J. Dermatol.* **2008**, 159(6), 1245-66.

[154] S. Noimark, M. Bovis, A.J. MacRobert, A. Correia, E. Allan, M. Wilson, I.P. Parkin, Photobactericidal polymers; the incorporation of crystal violet and nanogold into medical grade silicone, *RSC Advances* **2013**, 3(40), 18383.

[155] D.J. Weber, W.A. Rutala, Self-disinfecting surfaces: review of current methodologies and future prospects, *Am. J. Infect. Control* **2013**, 41, 531-535.

[156] T. Walker, M. Canales, S. Noimark, K. Page, I. Parkin, J. Faull, M. Bhatti, L. Ciric, A Light-Activated Antimicrobial Surface Is Active Against Bacterial, Viral and Fungal Organisms, *Sci. Rep.* **2017**, 7(1), 15298.

[157] D.J. Weber, W.A. Rutala, E.E. Sickbert-Bennett, H. Kanamori, D. Anderson, C.D.C.P.E. Program, Continuous room decontamination technologies, *Am. J. Infect. Control* **2019**, 47S, A72-A78.

[158] D. Weng, H. Qi, T.T. Wu, M. Yan, R. Sun, Y. Lu, Visible light powered self-disinfecting coatings for influenza viruses, *Nanoscale* **2012**, 4(9), 2870-2874.

[159] M.M. Querido, L. Aguiar, P. Neves, C.C. Pereira, J.P. Teixeira, Self-disinfecting surfaces and infection control, *Colloids Surf B Biointerfaces* **2019**, 178, 8-21.

[160] E. Akarsu, R. Uslu, Light-activated hybrid organic/inorganic antimicrobial coatings, *J. Sol-Gel Sci. Technol.* **2018**, 87(1), 183-194.

[161] J. J. M. Lamberts, D. R. Schumacher, D. C. Neckers, Novel rose bengal derivatives: synthesis and quantum yield studies, *J. Am. Chem. Soc.* **1984**, 106, 5879–5883.

[162] V. Decraene, J. Pratten, M. Wilson, Cellulose acetate containing toluidine blue and rose bengal is an effective antimicrobial coating when exposed to white light, *Appl. Environ. Microbiol.* **2006**, 72(6), 4436-9.

[163] V. Decraene, J. Pratten, M. Wilson, Assessment of the activity of a novel light-activated antimicrobial coating in a clinical environment, *Infect. Control Hosp. Epidemiol.* **2008**, 29, 1181–1184.

[164] J. Baier, T. Maisch, M. Maier, M. Landthaler, W. Baumler, Direct detection of singlet oxygen generated by UVA irradiation in human cells and skin, *J. Invest. Dermatol.* **2007**, 127(6), 1498-506.

[165] A.N. Onyango, Endogenous Generation of Singlet Oxygen and Ozone in Human and Animal Tissues: Mechanisms, Biological Significance, and Influence of Dietary Components, *Oxid. Med. Cell Longev.* **2016**, 1-22.

[166] M. Morsella, N. d'Alessandro, A.E. Lanterna, J.C. Scaiano, Improving the Sunscreen Properties of TiO2 through an Understanding of Its Catalytic Properties, *ACS Omega* **2016**, 1(3), 464-469.

[167] M. Battistin, V. Dissette, A. Bonetto, E. Durini, S. Manfredini, A. Marcomini, E. Casagrande, A. Brunetta, P. Ziosi, S. Molesini, R. Gavioli, F. Nicoli, S. Vertuani, A. Baldisserotto, A New Approach to UV Protection by Direct Surface Functionalization of TiO2 with the Antioxidant Polyphenol Dihydroxyphenyl Benzimidazole Carboxylic Acid, *Nanomaterials (Basel)* **2020**, 10(2), 231.

[168] A. Prasad, A. Balukova, P. Pospisil, Triplet Excited Carbonyls and Singlet Oxygen Formation During Oxidative Radical Reaction in Skin, *Front. Physiol.* **2018**, 9, 1109.

[169] N. Joly-Tonetti, J.I.D. Wibawa, M. Bell, D.J. Tobin, An explanation for the mysterious distribution of melanin in human skin: a rare example of asymmetric (melanin) organelle distribution during mitosis of basal layer progenitor keratinocytes, *Br. J. Dermatol.* **2018**, 179(5), 1115-1126.

[170] T. Aasen, J.C. Izpisua Belmonte, Isolation and cultivation of human keratinocytes from skin or plucked hair for the generation of induced pluripotent stem cells, *Nat. Protoc.* **2010**, 5(2), 371-382.

[171] B. Zeina, J. Greenman, D. Corry, W. M. Purcell, Cytotoxic effects of antimicrobial photodynamic therapy on keratinocytesin vitro, *Br. J. Dermatol.* **2002**, 46, 568–573.

[172] B. Poljsak, R. Dahmane, Free radicals and extrinsic skin aging, *Dermatol. Res. Pract.* **2012**, 2012, 1-4.

[173] J. Duan, L. Gan, L. Nie, F. Sun, X. Lu, G. He, On the penetration of reactive oxygen and nitrogen species generated by a plasma jet into and through mice skin with/without stratum corneum, *Phys. Plasmas* **2019**, 26(4), 043504.

[174] K.K. Wang, S. Song, S.J. Jung, J.W. Hwang, M.G. Kim, J.H. Kim, J. Sung, J.K. Lee, Y.R. Kim, Lifetime and diffusion distance of singlet oxygen in air under everyday atmospheric conditions, *Phys. Chem. Phys.* **2020**, 22(38), 21664-21671.

[175] Y. Litman, H.B. Rodriguez, E. San Roman, Tuning the concentration of dye loaded polymer films for maximum photosensitization efficiency: phloxine B in poly(2-hydroxyethyl methacrylate), *Photochem. Photobiol. Sci.* **2016**, 15(1), 80-85.

[176] T. Entradas, S. Waldron, M. Volk, The detection sensitivity of commonly used singlet oxygen probes in aqueous environments, *J. Photochem. Photobiol.* **2020**, B 204, 111787.

[177] C. Wang, P. Chen, Y. Qiao, Y. Kang, C. Yan, Z. Yu, J. Wang, X. He, H. Wu, pH responsive superporogen combined with PDT based on poly Ce6 ionic liquid grafted on SiO2 for combating MRSA biofilm infection, *Theranostics* **2020**, 10(11), 4795-4808.

[178] S. George, A. Kishen, Photophysical, photochemical, and photobiological characterization of methylene blue formulations for light-activated root canal disinfection, *J. Biomed. Opt.* **2007**, 12(3), 034029.

[179] M. L. Rooney, R. V. Holland, Singlet oxygen: an intermediate in the inhibition of oxygen permeation through polymer films, *Chem. Industry* **1979**, 24, 900–901.

[180] T. Wilson, Excited singlet molecular oxygen in photooxidation, *J. Am. Chem. Soc.* **1966**, 88, 2898–2902.

[181] Editorial Board, Gas permeability etc. (1), *Nippon Gomu Kyo kaishi* **1982**, 55, 682.

[182] G. R. Ultsch, In vivo permeability coefficient to oxygen of the skin of Siren intermedia, *Am. J. Physiol.* **1974**, 226, 1219–1220.

[183] B. Takeda, B. Yamaguchi, Permeability of polymer films to gases, *Kogyo kagaku Zasshi* **1959**, 62, 1897–1904.

[184] K. Nagai, Gas barrier properties of plastic products for pack aging applications, *J. Print. Sci. Technol.* **2015**, 52, 149–155.

[185] A. Felgentrager, T. Maisch, A. Spath, J.A. Schroder, W. Baumler, Singlet oxygen generation in porphyrin-doped polymeric surface coating enables antimicrobial effects on Staphylococcus aureus, *Phys. Chem. Chem. Phys.* **2014**, 16(38), 20598-607.

[186] P. Wang, F. Qin, Z. Zhang, W. Cao, Quantitative monitoring of the level of singlet oxygen using luminescence spectra of phosphorescent photosensitizer, *Opt. Express* **2015**, 23(18), 22991-3003.

[187] L. Poulsen, I. Zebger, P. Tofte, M. Klinger, O. Hassager, P. R. Ogilby, Oxygen diffusion in bilayer polymer films. *J. Phys. Chem.* **2003**, B 107, 13885–13891.

[188] H. Hettegger, M. Gorfer, S. Sortino, A. Fraix, D. Bandian, C. Rohrer, W. Harreither, A. Potthast, T. Rosenau, Synthesis, characterization and photo-bactericidal activity of silanized xanthene-modified bacterial cellulose membranes, *Cellulose* **2015**, 22(5), 3291-3304.

[189] K. Hosoya, S. Yenchit, Y. Tadokoro, K. Oya, S. Iwamori, Improved Singlet Oxygen Detection Sensitivity in Electron Spin Resonance Using a Spin-trap Agent Incorporated into a Water-soluble Polymer Film, *Chem. Lett.* **2018**, 47(9), 1191-1193.

[190] S. Tanaka, T. Enoki, H. Imoto, Y. Ooyama, J. Ohshita, T. Kato, K. Naka, Highly Efficient Singlet Oxygen Generation and High Oxidation Resistance Enhanced by Arsole-Polymer-Based Photosensitizer: Application as a Recyclable Photooxidation Catalyst, *Macromolecules* **2020**, 53(6), 2006-2013.

[191] M. Morone, L. Beverina, A. Abbotto, F. Silvestri, E. Collini, C. Ferrante, R. Bozio, G. A. Pagani, Enhancement of two photon absorption cross-section and singlet-oxygen generation in porphyrins upon β-functionalization with donor−acceptor substituents, *Org. Lett.* **2006**, 8, 2719–2722.

[192] M.O. Sunday, H. Sakugawa, A simple, inexpensive method for gas-phase singlet oxygen generation from sensitizer-impregnated filters: Potential application to bacteria/virus inactivation and pollutant degradation, *Sci. Total Environ.* **2020**, 746, 141186.

[193] R. L. Clough, M. P. Dillon, K.-K. Iu, P. R. Ogilby, Behavior of singlet molecular oxygen in a polymer matrix: Effects of temperature, matrix rigidity, and molecular composition, *Macromolecules* **1989**, 22, 3620–3628.

[194] K. Schiller, F. W. Muller, Singlet oxygen lifetime in polymer films. *Polym. Int.* **1991**, 25, 19–22.

[195] M. Stucker, A. Struk, P. Altmeyer, M. Herde, H. Baumgärtl, D. W. Lübbers, The cutaneous uptake of atmospheric oxygen contributes significantly to the oxygen supply of human dermis and epidermis, *J. Physiol.* **2002**, 538, 985-994.

[196] H. Oda, Effect of Nickel Arylsulfonates on the Photofading of dyes in Polymer Substrate, *Sen'i Gakkaishi* **1991**, 47, 606–611.

[197] Z. Biyiklioglu, I. Ozturk, T. Arslan, A. Tunçel, K. Ocakoglu, M. Hosgor-Limoncu, F. Yurt, Synthesis and antimicrobial photodynamic activities of axially {4-[(1E)-3-oxo-3-(2-thienyl)prop-1-en-1-yl]phenoxy} groups substituted silicon phthalocyanine, subphthalocyanine on Gram-positive and Gram-negative bacteria, *Dyes and Pigments* **2019**, 166, 149-158.

[198] Bibliometric analysis of recent research on multidrug and antibiotics resistance (2017–2018), *J. Appl. Pharm.* Sci. **2019**, 9(5), 112-116.

[199] F. Nakonechny, M. Barel, A. David, S. Koretz, B. Litvak, E. Ragozin, A. Etinger, O. Livne, Y. Pinhasi, G. Gellerman, M. Nisnevitch, Dark Antibacterial Activity of Rose Bengal, *Int J Mol Sci* **2019**, 20(13). DOI: 10.3390/ijms20133196.

[200] E. Baigorria, M.E. Milanesio, E.N. Durantini, Synthesis, spectroscopic properties and photodynamic activity of Zn(II) phthalocyanine-polymer conjugates as antimicrobial agents, *Eur. Polym. J.* **2020,** 134. DOI: 10.1016/j.eurpolymj.2020.109816.

[201] A. Tavares, C.M. Carvalho, M.A. Faustino, M.G. Neves, J.P. Tome, A.C. Tome, J.A. Cavaleiro, A. Cunha, N.C. Gomes, E. Alves, A. Almeida, Antimicrobial photodynamic

therapy: study of bacterial recovery viability and potential development of resistance after treatment, *Mar Drugs* **2010**, 8(1), 91-105.

[202] N. Kashef, M.R. Hamblin, Can microbial cells develop resistance to oxidative stress in antimicrobial photodynamic inactivation?, *Drug Resist Updat* **2017**, 31, 31-42.

[203] S. Noimark, C.W. Dunnill, I.P. Parkin, Shining light on materials--a self-sterilising revolution, *Adv Drug Deliv Rev* **2013**, 65(4), 570-80.

[204] A.F. Forte Giacobone, M.F. Ruiz Gale, E.N. Hogert, O.J. Oppezzo, A Possible Phenomenon of Persistence in Pseudomonas aeruginosa Treated with Methylene Blue and Red Light, *Photochem. Photobiol.* **2016**, 92(5), 702-7.

[205] K. Page, M. Wilson, I.P. Parkin, Antimicrobial surfaces and their potential in reducing the role of the inanimate environment in the incidence of hospital-acquired infections, *J. Mater. Chem.* **2009**, 19(23), 3819.

[206] M. Q. Mesquita, C. J. Dias, M. G. P. M. S. Neves, A. Almeida, M. A. F. Faustino, Revisiting Current Photoactive Materials for Antimicrobial Photodynamic Therapy, *Molecules* **2018**, 23(10), 2424.

[207] M. Bhatti, A. MacRobert, S. Meghji, B. Henderson, M. Wilson, A study of the uptake of toluidine blue 0 by *Porphyromonas gingivails* and the mechanism of lethal photosensitization, *Photochem. Photobiol.* **1998**, 68, 370–376.

[208] M. Wainwright, Acridine-a neglected antibacterial chromophore, *J. Antimicrob. Chemother.* **2001**, 47, 1-13.

[209] B.L. Carpenter, F. Scholle, H. Sadeghifar, A.J. Francis, J. Boltersdorf, W.W. Weare, D.S. Argyropoulos, P.A. Maggard, R.A. Ghiladi, Synthesis, Characterization, and Antimicrobial Efficacy of Photomicrobicidal Cellulose Paper, *Biomacromolecules* **2015**, 16(8), 2482-92.

[210] L. George, A. Müller, B. Röder, V. Santala, A. Efimov, Photodynamic self–disinfecting surface using pyridinium phthalocyanine, *Dyes and Pigments* **2017**, 147, 334-342.

[211] L. M. Moreira, F. V. Santos, J. P. Lyon, M. Maftoum-Costa, C. Pacheco-Soares, N. S. Silva, Photodynamic therapy: porphyrins and phthalocyanines as photosensitizers, *Aust. J. Chem.* **2008**, 61, 741-754.

[212] N.E. Grammatikova, L. George, Z. Ahmed, N.R. Candeias, N.A. Durandin, A. Efimov, Zinc phthalocyanine activated by conventional indoor light makes a highly efficient antimicrobial material from regular cellulose, *J. Mater. Chem.* B **2019**, 7(28), 4379-4384.

[213] S.J.M. Nassar, C. Wills, A. Harriman, Inhibition of the Photobleaching of Methylene Blue by Association with Urea, *ChemPhotoChem* **2019**, 3(10), 1042-1049.

[214] J. Robinson-Duggon, N. Marino-Ocampo, P. Barrias, D. Zuniga-Nunez, G. Gunther, A.M. Edwards, A. Greer, D. Fuentealba, Mechanism of Visible-Light Photooxidative Demethylation of Toluidine Blue O, *J. Phys. Chem. A* **2019**, 123(23), 4863-4872.

[215] R. Gerdes, O. Bartels, G. Schneider, D. Wöhrle, G. Schulz-Ekloff, Photooxidations of phenol, cyclopentadiene and citronellol with photosensitizers ionically bound at a polymeric ion exchanger, *Polym. Adv. Technol.* **2001**, 12, 152-16.

[216] R. A. Kenley, N. A. Kirshen, T. Mill, Photooxidation of Di-n-butyl sulfide using sensitizers immobilized in polymer films, *Macromolecules* **1980**, 13, 808-815.

[217] O. Lyutakov, O. Hejna, A. Solovyev, Y. Kalachyova, V. Svorcik, Polymethylmethacrylate doped with porphyrin and silver nanoparticles as light-activated antimicrobial material, *RSC Adv.* **2014**, 4(92), 50624-50630.

[218] R. Bonnett, D. G. Buckley, T. Burrow, A. B. B. Galia, B. Saville, S. P. Songca, Photobactericidal materials based on porphyrins and phthalocyanines, *J. Mater. Chem.* **1993**, 3, 323–324.

[219] S. Makhseed, M. Al-Sawah, J. Samuel, H. Manaa, Synthesis, characterization and nonlinear optical properties of nonaggregating hexadeca-substituted phthalocyanines, *Tetrahedron Letters* **2009**, 50(2), 165-168.

[220] X.-F. Zhang, Q. Xi, J. Zhao, Fluorescent and triplet state photoactive J-type phthalocyanine nano assemblies: controlled formation and photosensitizing properties, *J. Mater. Chem.* **2010**, 20(32), 6726-33.

[221] M. Kucinska, P. Skupin-Mrugalska, W. Szczolko, L. Sobotta, M. Sciepura, E. Tykarska, M. Wierzchowski, A. Teubert, A. Fedoruk-Wyszomirska, E. Wyszko, M. Gdaniec, M. Kaczmarek, T. Goslinski, J. Mielcarek, M. Murias, Phthalocyanine derivatives possessing 2-(morpholin-4-yl)ethoxy groups as potential agents for photodynamic therapy, *J. Med. Chem.* **2015**, 58(5), 2240-55.

[222] S. Trashin, V. Rahemi, K. Ramji, L. Neven, S.M. Gorun, K. De Wael, Singlet oxygen-based electrosensing by molecular photosensitizers, *Nature Communications* **2017**, 8(1). DOI: 10.1038/ncomms16108.

[223] V.V. Zhdankin, V.N. Nemykin, E.A. Lukyanets, Synthesis of substituted phthalocyanines, *Arkivoc* **2010**, 2010(1), 136-208.

[224] N. Harada, M. Kataoka, M. Nakanosho, H. Uyama, Penetration of Singlet Oxygen into Films with Oxygen Permeability Coefficient Close to that of Skin, *Photochem. Photobiol.* **2021** (in press), DOI: 10.1111/php.13446.

[225] M.A. Revuelta-Maza, S. Nonell, G. de la Torre, T. Torres, Boosting the singlet oxygen photosensitization abilities of Zn(ii) phthalocyanines through functionalization with bulky fluorinated substituents, *Org. Biomol. Chem.* **2019**, 17(32), 7448-7454.

[226] J. Nakamura, Y. Miyoshi, G. Masuda, M. Aoki, Curable resin composition for imaging element and application thereof, JP6251530B2 **2017**.

[227] Available online: https://www.nature.com/articles/s41428-021-00532-9#Sec17.

[228] X.-F. Zhang, H.-J. Xu, Influence of halogenation and aggregation on photosensitizing properties of zinc phthalocyanine (ZnPC), *J. Chem. Soc. Faraday Trans.* **1993**, 89, 3347–3351.

[229] W. Chidawanyika, A. Ogunsipe, T. Nyokong, Syntheses and photophysics of new phthalocyanine derivatives of zinc, cadmium and mercury, *New Journal of Chemistry* **2007**, 31(3), 377-384.